Alma Mater Studiorum · Università di Bologna

DOTTORATO DI RICERCA IN
FISICA

Ciclo 33

Settore Concorsuale: 02/B1 – Fisica sperimentale della materia

Settore Scientifico Disciplinare: FIS/03 – Fisica della materia

New Methods for Brillouin Optical Time Domain Analyis

Presentata da:

Leonardo Rossi

Supervisore:

Prof. Gabriele Bolognini

Coordinatore Dottorato:

Prof. Michele Cicoli

Co-supervisore:

Prof. Beatrice Fraboni

Esame finale anno 2021

The uncreative mind can spot wrong answers, but it takes a very creative mind to spot wrong questions.

Antony Jay

He who knows all the answers has not been asked all the questions.

Confucius

Dedicated to my mother, my father
and my cat who suffered with me

Abstract

Brillouin optical time domain analysis (BOTDA) is one of the most important distributed optical fiber sensor technologies thanks to its capability of monitoring both temperature and strain distribution over tens of kilometers of sensing fibers with a single interrogating device. Because of this, BOTDA sensors have found important applications in structural health monitoring, safety, oil & gas and environmental engineering. Despite this, their employment is still limited by two factors: on one hand, the high complexity (and cost) for a single interrogator unit reduces the applications where BOTDA is competitive compared to classical point-like sensor applications. On the other, the time required to obtain a single temperature/strain distribution is in the order of several minutes, mainly limiting BOTDA to static or quasi-static measurements. In this thesis solutions are proposed for both of these limitations. In the first part, two different pump-probe laser sources based on Brillouin Ring Lasers (BRL) are shown and evaluated as low-cost alternatives to traditional sources employed in BOTDA. The first source, which is based on a long cavity BRL, is shown to be successfully employable in BOTDA measurements up to at least 10 km of range. The second source, which is based on a doubly resonant short cavity BRL, shows further improvements in intensity noise, output light spectral linewidth and tunability of the pump-probe frequency shift, at the cost of a slightly more complex hardware requirement, which still remains less severe than traditional sources. The activities were carried out in the framework of the Horizon 2020 project Pervasive Ubiquitous Lightwave Sensors (PULSe) which, among other aspects, focused on the development of innovative and low complexity Brillouin sensing equipment. In the second part, which was the result of a 9-month long collaboration with the Group for fiber optics (GFO) at the École polytechnique fédérale de Lausanne (EPFL), a fast BOTDA design based on a closed-loop control was explored and improved, with a particular focus in its signal processing methods. Finally, a new adaptive signal filtering technique to improve noise suppression is proposed and demonstrated.

Sommario

Brillouin optical time domain analysis (BOTDA) è una delle tecnologie più importanti tra i sensori distribuiti a fibra ottica grazie alla sua capacità di monitorare distribuzioni di temperatura e strain lungo decine di chilometri di fibre di sensing con un singolo dispositivo interrogatore. Per questo motivo i sensori BOTDA hanno trovato importanti applicazioni nel controllo della salute strutturale degli edifici, nella sicurezza, nei settori fossili e nell'ingegneria ambientale. Tuttavia, la loro applicabilità è ancora limitata da due fattori: da una parte, la complessità (e il costo) elevati per una singola unità interrogatrice riducono le applicazioni in cui i sensori BOTDA sono competitivi rispetto ai sensori puntuali classici. Dall'altra, il tempo richiesto per ottenere una singola distribuzione di temperatura o strain è dell'ordine di diversi minuti, limitando i sensori BOTDA principalmente a misure statiche o quasi-statiche. In questa tesi sono proposte soluzioni per entrambe le limitazioni. Nella prima parte, due differenti sorgenti pump-probe basate su laser ad anello Brillouin (BRL) sono presentate e valutate come alternative a basso costo rispetto alle sorgenti tradizionali utilizzate in BOTDA. Per la prima sorgente, che è basata su un BRL a cavità lunga, si dimostra che permette misure efficaci di BOTDA fino a una distanza di almeno 10 km. La seconda sorgente, che è basata su una cavità corta BRL doppiamente risonante, mostra ulteriori miglioramenti in termini di rumore di intensità, larghezza spettrale di banda e controllabilità dello shift di frequenza pump-probe al costo di un'attrezzatura leggermente più complessa, mantenendo un costo minore rispetto alle sorgenti tradizionali. Queste attività sono state condotte nell'ambito del progetto Horizon 2020 Pervasive Ubiquitous Lightwave Sensors (PULSe) che, tra gli altri obiettivi, si focalizza sullo sviluppo di dispositivo per sensori Brillouin innovativo a bassa complessità. Nella seconda parte, che è stata il risultato di una collaborazione con il Group for fiber optics (GFO) all'École polytechnique fédérale de Lausanne (EPFL), è stato studiato e migliorato uno schema BOTDA veloce basato su un controllo a circuito chiuso, con particolare attenzione alle tecniche impiegate per l'analisi del segnale. Infine si propone e dimostra un nuovo metodo adattivo di filtraggio del segnale per migliorare la soppressione del rumore.

Contents

List of Figures

Acronyms

AOM	Acousto-optic modulator
ATT	Attenuator
AWG	Arbitrary waveform generator
B-EDFA	Bi-directional erbium doped fiber amplifier
BFL	Brillouin fiber laser
BFS	Brillouin frequency shift
BGS	Brillouin gain spectrum
BRL	Brillouin ring laser
BOTDA	Brillouin optical time domain analysis
CC-BOTDA	Closed circuit BOTDA
CW	Continuous Wave
F-BOTDA	Fast BOTDA
SA-BOTDA	Slope-assited BOTDA
DAQ	Data AcQuisition
DC	Directional Coupler
DFB	Distributed feedback
DRC	Doubly resonant cavity
DRC-BRL	Doubly resonant cavity BRL
DOFS	Distributed optical fiber sensor
EDFA	Erbium doped fiber amplifier
EOM	Electro Optic Modulator
ESA	Electrical spectrum analyzer
FBG	Fiber bragg grating
FFT	Fast Fourier transform
FSR	Free spectral range
FUT	Fiber Under Test
FWHM	Full-Width at Half Maximum
GPIB	General Purpose Interface Bus

LC-BRL	Long cavity BRL
MZM	Mach-Zender modulator
OC	Optical Circulator
OFDM	Orthogonal frequency-division multiplexing
OFS	Optical fiber sensors
OSA	Optical Spectrum Analyzer
OSB	Optical Sideband
P	Proportional Controller
PC	Polarization controller
PD	Photodetector
PI	Propotional Integral controller
PID	Proportional-integral-derivative controller
PLL	Phase-locked loop
PS	Polarization scrambler
PZT	Piezoactuator
RF	Resonant Frequency
RIN	Relative intensity noise
SBS	Stimulated Brillouin cattering
SC-BRL	Short cavity BRL
SNR	Signal to Noise Ratio
SOA	Semiconductor optical amplifier
VOA	Variable optical attenuator

Introduction

In the last decades, distributed optical fiber sensors have affirmed themselves as a viable alternative that competes with conventional sensing techniques. On one hand, this is due to the inherent desirable properties of optical fibers, such as reduced dimensionality, light weight and resistance to environmental damage and to electromagnetic interference. On the other, optical fiber sensors offer the unique possibility of monitoring spatial distributions of relevant physical properties (such as temperature, strain, pressure and similar) with the use of a single interrogating device. This characteristic, which to this day cannot be replicated by any other kind of technology, has made distributed optical fiber sensors a preminent candidate for applications requiring the continuous and simultaneous monitoring of extensive structures such as buildings, bridges, tunnels, planes, ships and pipelines, which are relevant for a variety of sectors, including energy, security, oil and gas industry and environmental monitoring.

Several kinds of distributed optical fiber sensors have been developed over the years, thanks to improved understanding of scattering phenomena in optical fibers and the advancement of time and frequency-domain techniques to analyze them, leading to the creation of a wide variety of optical fiber sensors. Among them, Brillouin optical time analysis (BOTDA), which is based on stimulated Brillouin scattering, has proven to be one of the most attractive distributed optical fiber sensing techniques, thanks to its ability to monitor temperature and strain variations across tens of kilometers of sensing fibers with good sensitivity.

Despite the exceptional qualities that characterize BOTDA and other types of distributed optical fiber sensors, several challenges limit their fields of applicability. First of all, while the cost of optical fibers has been drastically reduced thanks to the interest and developement in telecommunication, the

complexity (and cost) of the interrogating equipment still remains high, which limits its employment outside of very large scale applications where the number of point like sensors needed would simply be unfeasible. In addition, the time required to extract a single temperature and/or strain distribution is in the order of minutes, mainly limiting the employment of BOTDA to static or quasi-static measurement and preventing dynamic monitoring.

In this thesis, possible ways of reducing both of these issues are explored. First, two novel sources based on Brillouin ring lasers are presented as a low-complexity and low-cost alternative to traditional light source design in order to reduce the price of BOTDA interrogating systems. Their performance is evaluated in terms of tunability, intensity noise, conversion efficiency and spectral linewidth, and their viability for BOTDA measurements is demonstrated showing, in addition to lower hardware requirements, specific performance advantages which are unique to Brillouin ring lasers and can prove beneficial in other BRL applications, such as communications and LIDAR detection.

Second, a previously developed closed-circuit design for dynamic BOTDA is presented. Its control system for the closed loop, which is based on a PID controller, is evaluated in terms of control speed, dynamic step response and noise filtering and compared with other filters, such as the moving average. In addition, a new adaptive signal filtering method is proposed, which consists of a method to control whether the system under measurement is in a stationary or dynamic state and employs a filter that is appropriate to each case: one with faster impulse response and smaller noise reduction factor to capture dynamic changes and one with slower impulse response and high reduction factor to more accurately determine the equilibrium state reached by the system. It is shown that this method has a response speed that is very close to the moving average filter, which is known to be optimal in situations (such as the one described in this work) where data is gathered in real time and no previous assumption can be made on the evolution of the system, maintaining similar performance in noise suppression when the signal is in dynamic phases and outperforming it when the signal is in stationary phases. While other filters, namely nonlinear filters, are known to show better performance than the moving average filter, they require an accurate model of the system being monitored to predict its state based on the measurement. The proposed method, on the other hand, only requires information about the extent of the minimum changes the system must undergo to be considered dynamic or static. Finally, the closed-loop measuring method is implemented experimentally with

the previously demonstrated PI implementation and the new method, showing the possibility for measurements with similar response speed but higher noise suppression, especially for slowly changing readings.

The first chapter presents the main principles of optical fiber sensors and distributed optical fiber sensor technology, including their main advantages with respect to traditional sensors. Afterwards, it gives a theoretical description of the stimulated Brillouin scattering process and details the generalities of the BOTDA sensing process.

The second chapter describes the two most used light source schemes for Brillouin optical time domain analysis, presenting their main advantages and drawbacks. It then describes Brillouin ring lasers, showing the way they could be employed as a source for Brillouin optical time domain analysis. Finally, a developed low-cost hybrid Brillouin ring laser-erbium doped fiber amplifier source is presented, and its performance is evaluated in terms of noise intensity, output linewidth and tunability. Finally, its employment in BOTDA measurements is showcased, providing estimates for its measurement resolution for a range of 10 km.

The third chapter describes a developed short cavity Brillouin ring laser source which uses the double resonance effects and improves on the previous one in terms of conversion efficiency, intensity noise and cavity linewidth, paired with a wavelength locking system that allows high frequency stabilization and accurate tunability.

In the fourth chapter, the issue of the slow measurements for BOTDA systems is outlined and potential solutions are presented, with particular attention to the slope-assisted BOTDA method. Finally, a closed-circuit implementation of the slope-assisted BOTDA method is presented, which allows to surpass one of its major limitations, namely the reduced measurement range, and its application for measurement sensing is showcased.

In the fifth chapter the PID control system used in the closed-circuit BOTDA is evaluated in terms of tracking capabilities and noise filtering. To do so, a model is created to simulate the behavior of a PID controller which is then characterized in terms of noise suppression and step response and compared with the moving average. Afterwards, a new adaptive filtering method is proposed and shown to perform as well as the moving average and better in specific occasions.

In the sixth chapter, a BOTDA system like the one shown in the fourth chapter is implemented with shorter range and increased speed. The causes for technical limitations found in the original implementation (such as a

slowed measurement time compared to the original slope-assisted method) are identified and possible ways to overcome them are presented. Finally, experimental results are presented and implementations where the data is filtered by the PID controller, the moving average and an implementation of the proposed filtering method were tested, showing the better performance of the latter in terms of noise suppression to determine the temperature when stationary while having similar speed.

1

Brillouin Optical Time Domain Analysis

In the most general terms, all optical fiber sensors (OFS) involve an optical beam being modulated or altered in an interaction region after being guided there by an optical fiber, and the nature or the extent of the alteration is linked with changes in the local environment [18].

The change to the beam could be in terms of intensity, phase (delay), polarization, frequency or more generally spectral composition, and this changed optical signal is fed through an optical fiber into a receiver, from which the measurand, that is the environmental conditions that caused the change in the first place, can be extracted. A schematic representation of this is shown in figure 1.1 on the following page.

1.1 Distributed optical fiber sensors

A variety of OFS technologies have been developed in the last decades, which use different interactions or monitored different aspects of the local environment [38, 47, 109]. The most generic way to divide them into classification is to distinguish between extrinsinc and intrinsic sensors [109].

- In extrinsic sensors, also known as hybrid fiber sensors, optical fiber only serves the role of carrying the light from the source where it interacts with the external environment and is influenced by the measurand, and then directing the altered light into the receiver.
- In intrinsic sensors, also known as all-fiber sensors, the optical fiber also acts as the interaction medium. In this case, the environment directly alters the light as it passes through the fiber, which for this reason is also known as sensing fiber.

Of these two types, intrinsic sensors are of particular interest due to the inherent advantages optical fibers present: they are light, flexible and thus can be applied to a wide variety of structures while occupying very small volumes [13]. In addition, due to their capability of transmitting information through light and not through electrons, they are immune to electromagnetic interferences, and the light signals needed for the sensing to occur can be generated at considerable distances from the point where the measurement will take place. Because of these reasons OFS-based technology is known to be successfully employable in a variety of applications [47].

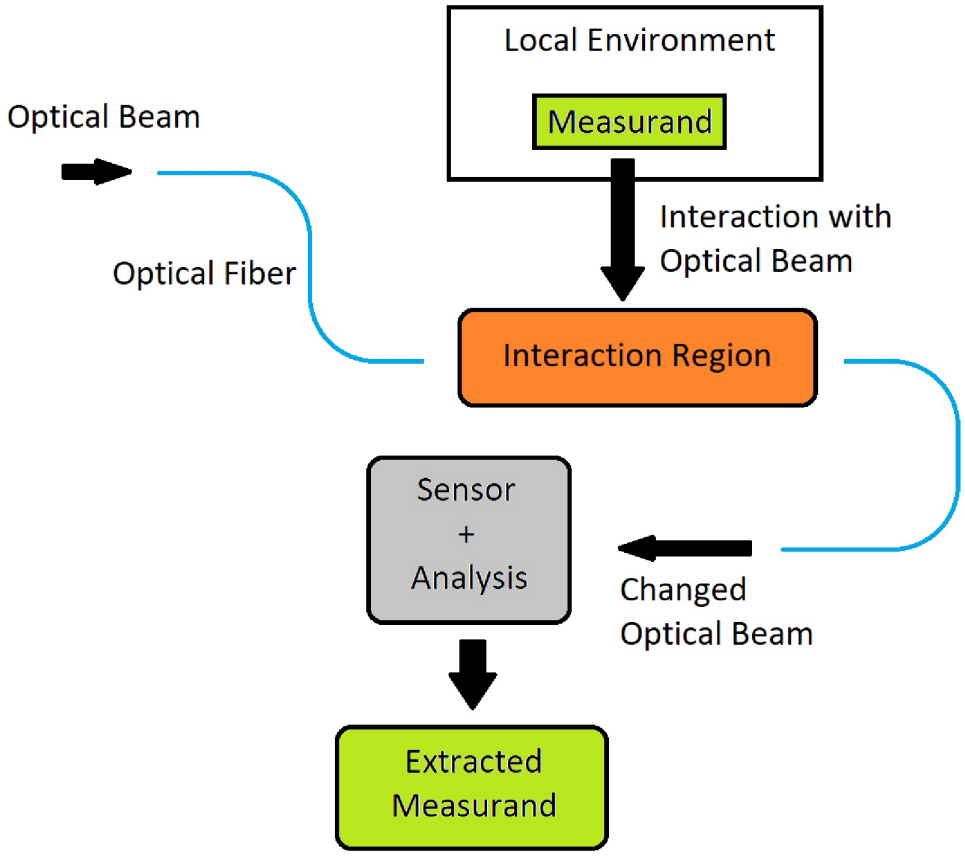

Figure 1.1: Schematic representation of a generic OFS.

Nevertheless, their diffusion has been so far limited by the fact that they are competing with well-established conventional sensor technologies (such as electronic sensors) which, in general, provide effective sensors which are reliable and low cost [47].

Despite this, OFS technologies, thanks to their fiber-based nature, offer unique advantages that make them desirable in specific applications compared

with conventional sensing methods. Among these advantages, one of the most relevant and which is exclusive to OFS is the possibility of providing distributed sensing [38, 47, 49, 73], while conventional sensors can only provide discrete sensors.

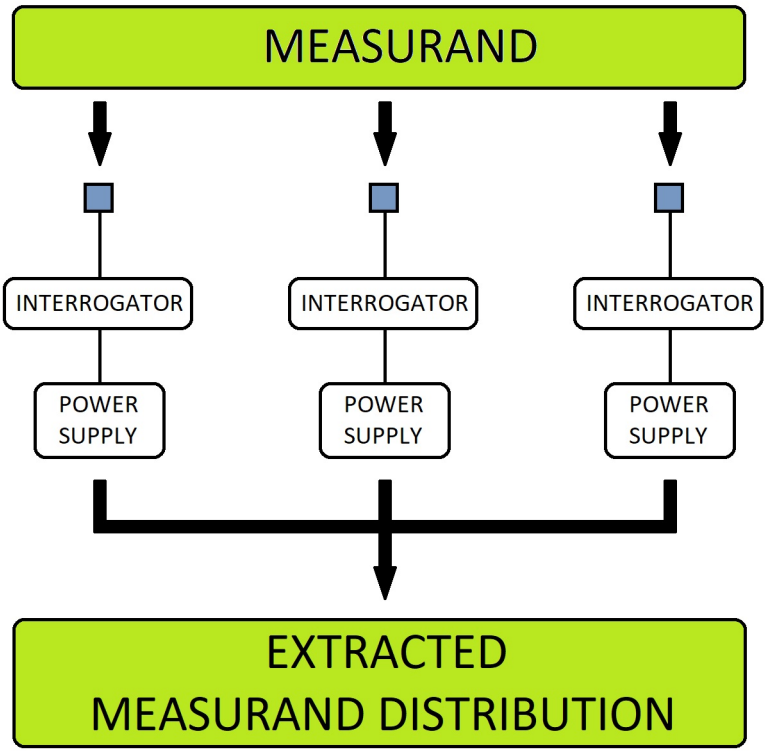

Figure 1.2: Schematic representation of an array of discrete sensors.

The difference between the two types of sensor can be described as follows:

- **Discrete sensors**: In this type of sensors (shown schematically in figure 1.2), only the measurand of a single point can be detected at a single time. In the case when multiple measurands have to be acquired, for example to obtain the temperature distribution along a power plant, multiple copies of the sensors have to be applied and their output has to be organized in a network, with each sensor measuring a single point of the distribution. Because of this, they are also called point sensors. In general, this type of sensors (be it optical or electronic) is limited by the fact that it is not always possible to reliably determine the points where the sensors must be located in order to gather the desired information. In addition, if the number of points to be monitored simultanously is high

enough, the complexity of the sensor network can become unmanageable, also due to the fact that every single point requires a distinct sensor, which includes the set of hardware that is required for its functioning and gathering its output (known as an interrogator) and the relative power supply.

- **Distributed sensors**: In distributed sensors (shown schematically in figure 1.3), which are usually intrinsic OFS, the interaction region is located in every point of the sensing fiber. Mixed with the possibility to spatially discriminate the change in the light signal taking place at different points, it is possible to acquire the desired measurand of every point of the monitored environment, which can thus be monitored in its entirety with a single measurement. As further advantage, this can be accomplished with a single power source powering a single beam source, which provides the light signal and then uses a single interrogator to extract the measurand by evaluating how it has changed when it reaches the end of the sensing fiber.

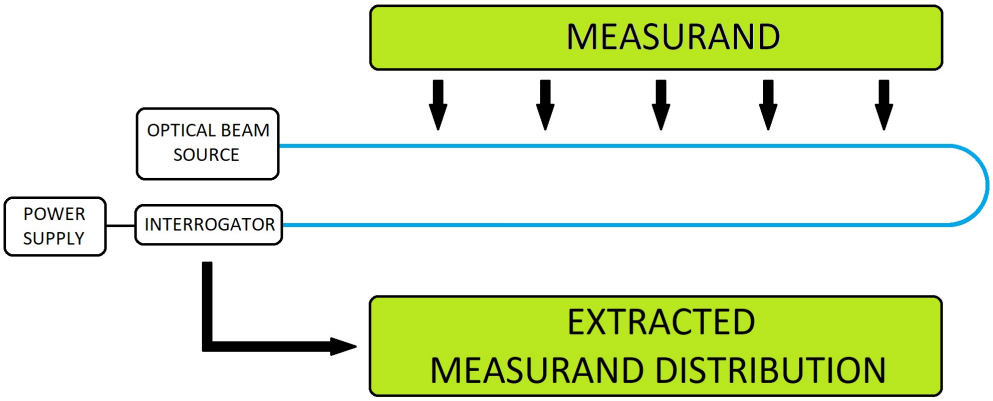

Figure 1.3: Schematic representation of a DOFS

DOFS, with their capability of performing distributed measurements using a non-intrusive and flexible medium such as optical fibers, offer a new kind of monitoring, diagnosis and control of large and extended structures [79]. In particular, in the most extreme large-scale cases a single optical fiber and a single interrogator can potentially replace thousands of conventional discrete sensors, providing not only a reduction in complexity of the system and required power supplies, but also a significant reduction in the cost and work associated with installation, calibration and maintenance.

From these characteristics, it is easy to see that distributed optical fiber sensors (DOFS) provide benefits which are invaluable for applications where the distribution of a measurand over very large structures needs to be monitored [88]. This situation is encountered in applications such as monitoring the temperature distribution across a oil and gas pipelines in order to detect leaks, or monitoring the strain of very large structure, such as buildings, bridges, submarines and ships, provide a fire alarm system or even early slide detection systems [15, 86].

In order to work, these sensors exploit linear and nonlinear optical scattering effects which can be easily recreated in optical fibers, such as Rayleigh scattering, spontaneous Raman scattering and spontaneous or stimulated Brillouin scattering [71, 74]. Depending on the effect used, DOFS will be able to detect different measurand (such as temperature or strain) and will have different measurement ranges and spatial resolutions. In addition, the measurands that can be explored with a specific effect can be expanded with the use of apposite fibers [87].

Among the different types of DOFS, Brillouin Optical Time Domain Analysis (BOTDA), which is based on a phenomenon known as stimulated Brillouin scattering (SBS) has gathered significant attention due to its capability of allowing simultaneous distributed measurements of temperature and strain over lengths of tens of km.

1.2 Stimulated Brillouin Scattering

Stimulated Brillouin Scattering (SBS) is one of the main scattering effects that occur in telecommunication fibers, and results in the generation of a downshifted, backward-propagating light wave (known as the Stokes light) that carries a significant part of the input power. Since this phenomenon occurs only once a certain level of input power (known as the Brillouin threshold) is reached, in optical communication systems SBS is one of the main limiting factors for the maximum channel power that can be employed. At the same time, it can be useful for making fiber-based Brillouin lasers and amplifiers [2].

In physical terms, it can be classically described as the interaction of two lightwaves, a “pump” and a counterpropagating, downshifted “probe”, mediated by an acoustic wave propagating through the medium. Through the process of electrostriction [67], by which the electric field of the light contracts or dilates a dielectric medium (such as the core of an optical fiber),

the beating of the two lightwaves generates an acoustic wave, which in turn creates a modulation of the medium's refractive index, as shown in figure 1.4 below. Since the electric field of the interference patterns created by the two lights is periodical, the refractive index modulation is also periodical, and turns the medium into a Bragg diffraction grating which scatters the pump lightwave. The induced grating moves at the same speed of the acoustic wave, which is the acoustic velocity V_A of the medium, in the same direction of the pump, resulting in the scattered light being downshifted due to the Doppler effect. This scattered light adds to the probe, amplifying it, which in turn further increases the acoustic wave.

Two situations can lead to SBS taking place in an optical fiber. The first (known as Brillouin amplifier), and most obvious, takes place when two counterpropagating waves are present in the same medium. If the frequency shift between the two waves is compatible with the acoustic speed, the upshifted light will transfer power to the downshifted one, resulting in a "controlled" amplification which can be employed in light amplifiers or, as will be seen below, for DOFS. The second (known as Brillouin generator) takes place with only one light. In this situation, a downshifted, counterpropagating light (called Stokes light) is generated through a process known as spontaneous Brillouin scattering, which involves the light being inelastically scattered by the medium phonon field. If the power of the original light is high enough, SBS will be triggered, with the first light acting as the pump and the Stokes light acting as the probe.

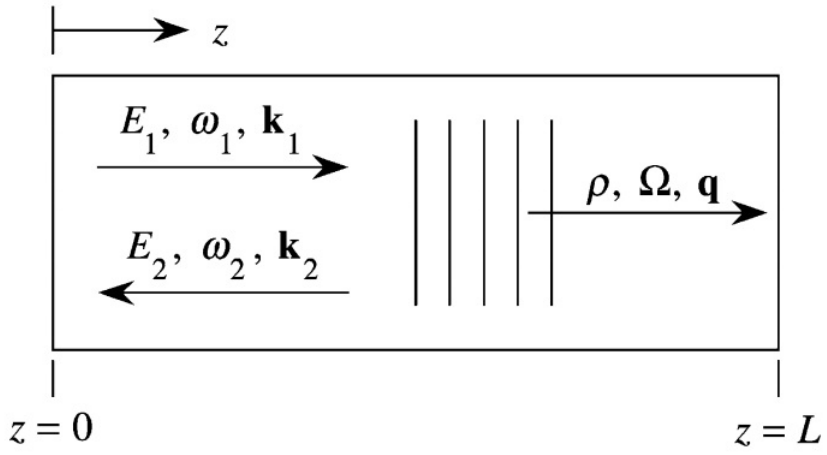

Figure 1.4: Wave representation of the pump, probe and acoustic waves in stimulated Brillouin scattering. From [8].

1.2.1 Physical process

Figure 1.4 on the preceding page schematically represents the Brillouin scattering process. In the generator situation, the "probe" will have a frequency that will only depend on the pump and acoustic characteristics of the fiber. If ω_P and ω_S are the pump and probe frequency respectively, the frequency of the acoustic wave Ω_B, due to energy conservation, must be defined as:

$$\Omega_B = \omega_P - \omega_S \tag{1.1}$$

And, for momentum conservation, the same must apply for the wave vectors $\mathbf{k}$:

$$\mathbf{K_B} = \mathbf{k_P} - \mathbf{k_S} \tag{1.2}$$

Acoustic waves propagate through a medium with a speed that is always equal to the acoustic velocity V_A. Because of this, $\mathbf{K_B}$ and Ω_B are linked by the relation:

$$\frac{\Omega_B}{|\mathbf{K_B}|} = V_A \quad \Longrightarrow \quad \Omega_B = V_A|\mathbf{K_B}| \tag{1.3}$$

Since the pump and probe are lightwaves, they follow similar relations with the speed of light in the medium $c\,/\,n$, where n is the refraction index:

$$|\mathbf{k_P}| = n\frac{\omega_P}{c} \quad \text{and} \quad |\mathbf{k_S}| = n\frac{\omega_S}{c} \tag{1.4}$$

By putting the relations shown in (1.4) in (1.2), and remembering that the pump and probe waves are counterpropagating, thus $|\mathbf{K_P} - \mathbf{K_S}| = |\mathbf{K_P}| + |\mathbf{K_S}|$, the following relation is obtained:

$$\Omega_B = \frac{V_A}{\frac{c}{n}}\left(\omega_P + \omega_S\right) \tag{1.5}$$

Adding the relation in (1.1) the ω_S can be removed from (1.5), resulting in the following relation between Ω_B and ω_P:

$$\Omega_B = \frac{\frac{2V_A}{\frac{c}{n}}\omega_P}{1 + \frac{V_A}{\frac{c}{n}}} \tag{1.6}$$

Since the speed of sound in the medium is many orders of magnitude smaller than the speed of light for all known materials, (1.6) can be approximated to:

$$\Omega_B = \frac{2V_A}{\frac{c}{n}}\omega_P \tag{1.7}$$

And similarly the acoustic wavevector is found to be:

$$\mathbf{K_B} = \mathbf{2k_P} \tag{1.8}$$

This evaluation is valid for the Brillouin generator case. For the Brillouin amplifier, the probe wave frequency is determined externally and a priori and, because of this, the frequency of the acoustic wave $\Omega = \omega_P - \omega_S$ will not necessarily be equal to the Brillouin shift shown in (1.7). As will be seen below, the acoustic wave will be excited effectively only if $|\Omega - \Omega_B|$ is within the order of a certain value.

Wave coupling

The optical field within the Brillouin medium can be represented as

$$\tilde{E}(z,t) = \tilde{E}_P(z,t) + \tilde{E}_S(z,t)$$

where:

$$\begin{aligned} \tilde{E}_P(z,t) &= A_P(z,t)\, e^{i(k_P z - \omega_P t)} \\ \text{and} \quad \tilde{E}_S(z,t) &= A_S(z,t)\, e^{i(k_S z - \omega_S t)} \end{aligned} \tag{1.9}$$

The acoustic field can be similarly described in terms of the material density distribution as

$$\tilde{\rho}(z,t) = \rho_0 + \left[\rho(z,t)\, e^{i(k_z - \Omega_t)}\right] \tag{1.10}$$

where $k = 2k_P$ and ρ_0 is the medium mean density. It can be assumed that the material density behaves like an acoustic wave, and thus follows the acoustic wave equation ([26, section 34.9]):

$$\frac{\partial^2 \tilde{\rho}}{\partial t^2} - \Gamma' \nabla^2 \frac{\partial \tilde{\rho}}{\partial t} - V_A^2 \nabla^2 \tilde{\rho} = \nabla \mathbf{f} \tag{1.11}$$

where Γ' is a damping constant dependant on the medium's viscous properties. The $\mathbf{f}$ term on the right hand side of (1.11) consists of the force per unit volume, which is defined as the gradient of the electrostrictive force, defined as

$$\mathbf{f} = \nabla p_{st}$$

where p_{st} is the pressure due to electrostrition, which, as said above, is the tendency of materials to become compressed in the presence of an electric field [8].

The contribution of the pressure due to an electric field p_{st} can be determined by:

$$p_{st} = \frac{1}{2}\,\epsilon\rho\left(\frac{\partial\epsilon}{\partial\rho}\right)\langle\mathbf{E}\cdot\mathbf{E}\rangle = -\frac{1}{2}\,\epsilon_0\gamma_0\,\langle\mathbf{E}\cdot\mathbf{E}\rangle$$

where ρ is the density of the medium, $\mathbf{E}$ is the electric field vector, ϵ_0 is the dielectric constant of the void and the term $\rho\left(\frac{\partial\epsilon}{\partial\rho}\right) = \gamma_0$ is known as the electrostrictive constant, while the angled brackets represent the temporal average over an optical period.

In this situation, p_{st} can be also directly defined as

$$p_{st} = -\frac{1}{2}\,\epsilon_0\gamma_0\,\langle\tilde{\mathbf{E}}^2\rangle$$

Using the fields defined in (1.9), the right-side term in (1.11) becomes:

$$\nabla\mathbf{f} = \epsilon_0\gamma_e k^2 A_P A_S^* e^{i\,(kz\,-\,\Omega t)} \tag{1.12}$$

Now, if the definition of $\tilde{\rho}$ in (1.9) and (1.10) are inserted into (1.11), and it is assumed that the amplitude of the acoustic wave varies slowly, it can be seen that (1.11) becomes:

$$-2i\,\Omega\,\frac{\partial\rho}{\partial t} + \left(\Omega_B^2 - \Omega^2 - i\Omega\Gamma_B\right)\rho - 2ikV_A^2\,\frac{\partial\rho}{\partial z} = \epsilon\gamma_e k^2 A_1 A_2^* \tag{1.13}$$

Where Γ_B is the Brillouin linewidth, defined as $\Gamma_B = k^2\Gamma'$, and it can be seen that $\tau_P = \Gamma_B^{-1}$ is the lifetime of the phonons involved in the process.

In (1.13), the last term on the left side describes the propagation of phonons in the medium, but hypersonic phonons like the ones involved here are known to be strongly damped and thus propagate only over short distances compared to the distances over the term of the right (which is linked to electrostriction) varies significantly. In addition, if steady state conditions are assumed, $\partial\rho\,/\,\partial t$ can also be dropped, and the acoustic amplitude can be expressed as:

$$\rho\,(z,t) = \epsilon_0\gamma_e k^2\,\frac{A_P - A_S^*}{\Omega_B^2 - \Omega^2 - i\Omega\Gamma_B} \tag{1.14}$$

Optical fields formulation

From the form of the density in (1.14), the spatial evolution of the optical field can be described with the wave equations:

$$\frac{\partial^2 \tilde{E}_i}{\partial z^2} - \frac{1}{\left(\frac{c}{n}\right)^2}\frac{\partial^2 \tilde{E}_i}{\partial t^2} = \frac{1}{\epsilon_0\, c^2}\frac{\partial^2 \tilde{P}_i}{\partial t^2}\,, \tag{1.15}$$

where i can stand for P (pump) or S (probe).$\tilde{P}$ is the nonlinear polarization, which is given by

$$\tilde{P} = \epsilon_0 \Delta\epsilon \tilde{E} = \epsilon_0 \rho_0^{-1} \gamma_e \tilde{\rho} \tilde{E} \tag{1.16}$$

The components of $\tilde{P}$ that can act as source for the the pump and probe fields, which are the components resonant with the respective fields and are given by:

$$\tilde{P}_P = p_P e^{i\,(k_P z - \omega_P t)} \qquad \text{and} \qquad \tilde{P}_S = p_S e^{i\,(k_S z - \omega_S t)} \tag{1.17}$$

where

$$p_P = \epsilon_0 \gamma_e \rho_0^{-1} \rho A_S \qquad \text{and} \qquad p_S = \epsilon_0 \gamma_e \rho_0^{-1} \rho A_P \tag{1.18}$$

If the definition of the fields in (1.9) is introduced into (1.15), alongside the definitions of the polarization in (1.17) and (1.18), and assuming that amplitudes vary slowly, the following equations are obtained:

$$\frac{\partial A_P}{\partial z} + \frac{1}{\frac{c}{n}}\frac{\partial A_P}{\partial t} = \frac{i\omega\gamma_e}{2nc\rho_0}\,\rho A_S \quad \text{and} \quad \frac{\partial A_S}{\partial z} + \frac{1}{d\frac{c}{n}}\frac{\partial A_S}{\partial t} = \frac{i\omega\gamma_e}{2nc\rho_0}\,\rho^* A_P \tag{1.19}$$

where ρ is the solution to (1.13). In addition, by using $\omega = \omega_P \simeq \omega_S$ the distinction between ω_P and ω_S has been dropped. Under steady state conditions, the time derivatives in (1.19) can be dropped and for r the solution (1.14) can be used. As a result, the amplitude equations become:

$$\begin{aligned} \frac{\partial A_P}{\partial z} &= \frac{i\epsilon_0\omega k^2\gamma_e^2}{2nc\rho_0}\,\frac{|A_S|^2 A_P}{\Omega_B^2 - \Omega^2 - i\Omega\Gamma_B} \\ \text{and} \quad \frac{\partial A_S}{\partial z} &= \frac{i\epsilon_0\omega k^2\gamma_e^2}{2nc\rho_0}\,\frac{|A_P|^2 A_S}{\Omega_B^2 - \Omega^2 - i\Omega\Gamma_B} \end{aligned} \tag{1.20}$$

From these equations it can be seen that stimulated Brillouin Scattering is a pure gain process, where each wave is either amplified or depleted by the other, and the waves are always automatically phase-matched. As a result,

the interacting optical waves can be described as coupled equations. Defining their intensities as $I_i = 2n\epsilon_0 c A_i A_i^*$, the equations at (1.20) become:

$$\frac{dI_P}{dz} = -gI_P I_S \qquad \text{and} \qquad \frac{dI_S}{dz} = -gI_P I_S \tag{1.21}$$

g is the gain factor, which is given by

$$g = g_0 \frac{\left(\frac{\Gamma_b}{2}\right)^2}{(\Omega_B - \Omega)^2 + \left(\frac{\gamma_B}{2}\right)^2} \tag{1.22}$$

where g_0 , which is the gain when $\Omega = \Omega_B$, is given by

$$g_0 = \frac{\gamma_e^2 \omega^2}{n V_A c^3 \rho_0 \Gamma_B} \tag{1.23}$$

1.2.2 Constant pump approximation

Assuming that the pump is constant (which is true for low pump and probe intensity), which is equivalent to putting $I_P =$ constant in (1.21), the solution for I_S is:

$$I_S(z) = I_S(L)\, e^{g I_S (L - z)}$$

Which describes a probe that is injected at $z = L$ and grows exponentially as it propagates through the medium and is amplified by the pump. The extent of this gain is dependant on the gain factor g, and is maximum when $\Omega = \Omega_B$.

The function $g(\Omega)$, which is shown in (1.22), determines the efficiency of this process and depends on the pump-probe frequency shift. This function is also known as the Brillouin Gain Spectrum (BGS) and the frequency shift value $\Omega = \Omega_B$ where this function reaches the maximum is known as the Brillouin Frequency Shift (BFS). In more detail, the function (1.22) is a Lorentzian distribution whose peak is centered at Ω_B and has a full-width half maximum linewidth equal to Γ_B

1.2.3 Environment effects on SBS

As shown in (1.18), the BFS is dependant on the pump wavelength and the acoustic velocity of the medium. In terms of frequency and wavelength, it can also be defined as:

$$\nu_B = \frac{2nV_A}{\lambda_P}$$

where ν_B is the BFS (expressed in frequency) and λ_P is the pump wavelength. For silica (SiO2) telecommunication fiber, the BFS value is arnound 10.8 GHz for a pump wavelength of 1550 nm. In other words, the BFS depends on the refractive index n and the acoustic velocity V_A, which are known to be temperature and longitudinal strain dependant. More in particular, most of the changes in the BFS are known to be linked to changes in the acoustic velocity [39, 40].

As a result, different local environmental conditions in temperature and strain causes changes in the SBS process which manifest in a shift in the BFS.

Several sources have shown that the shifts in BFS are directly proportional to the changes in strain $\Delta\epsilon$ and temperature ΔT, showing the relationship [76, 77]:

$$\Delta BFS = C_{\nu_B\epsilon}\Delta\epsilon + C_{\nu_B T}\Delta T$$

where $C_{\nu B\epsilon}$ and $C_{\nu BT}$ are constant coefficients, which for most optical fibers are equal respectively to 0.046 MHz / $\mu\epsilon$ and 1.07 Mhz

The Brillouin linewidth was also shown to display a weak dependence (with a ratio roughly equal to one tenth of $C_{\nu BT}$) to the temperature in a nonlinear way with a sensitivity that decreases with increasing temperature [70].

1.3 Brillouin Optical Time Domain Analysis

The dependency of the SBS process on temperature and strain means that it can be used as a basis for a DOFS. In addition, the SBS effect is known to have higher gain and sensitivity than other scattering effects, which both are favorable traits for creating DOFS with good resolution.

As mentioned above, the DOFS sensors that employ SBS are the one based on the Brillouin Optical Time Domain Analysis (BOTDA) technique, whose operating principle is shown in figure 1.5 on the facing page. The SBS is triggered inside a sensing fiber by two lights obtained from two single-frequency lasers emitting at both ends of a sensing fiber of length L. In order to allow for spatially resolved measurements, the light source at the fiber input ($z = 0$, propagating in the +z direction) is pulsed, while the light at the fiber end ($z = L$, propagating in the $-z$ direction) is continuous, and thus is also defined as continuous wave (CW) [41].

Depending on which of the two sources acts as the pump and as the probe, two different configurations are possible:

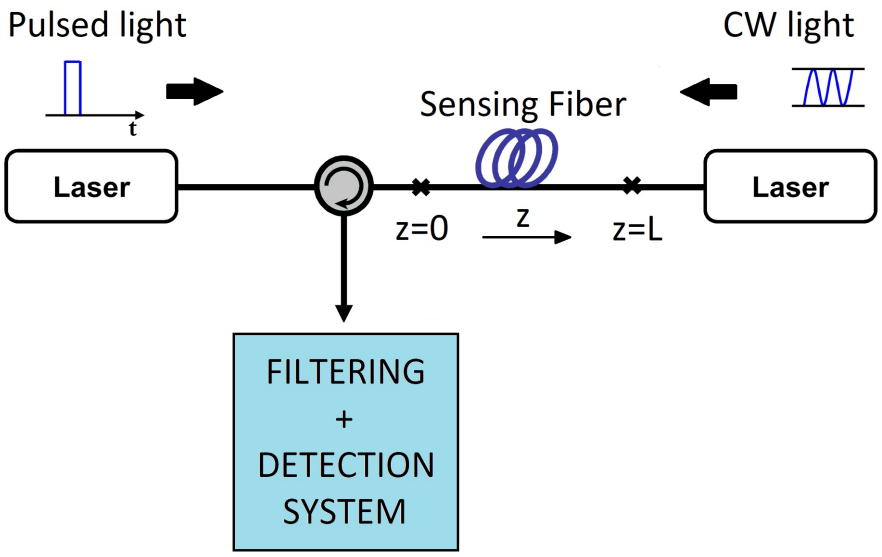

Figure 1.5: General representation of a BOTDA system.

- In the configuration known as Brillouin gain, the pulsed light (whose frequency will be called ν_0) acts as the pump for Brillouin amplification, while the CW light acts as a probe and will be downshifted from the pump by a fequency amount equal to $\Delta\nu$ [23]. When the CW probe frequency lies within the BGS for the pump, its signal is amplified through SBS as it travels through the sensing fiber. In particular, every point of the CW probe will be amplified only at a precise time when it meets the pulsed pump, which happens at a specific point of the fiber. As a result, by detecting the CW probe trace as it travels through the fiber it is possible to monitor the SBS at every point of the fiber through simple time-of-flight calculations. Since the SBS is dependant on local temperature and strain conditions, a variation in SBS due to different temperature/strain condition will be visible in the measured trace as a different gain, as shown in figure 1.6 on the next page. In order to obtain the temperature and strain distribution along the sensing fiber, the CW traces at different $\Delta\nu$ are measured to reconstruct the BGS for every point of the fiber. From there, it is possible (for instance through Lorentzian curve fitting) to extract the BFS at every point of the sensing fiber, and finally the temperature and strain distributions. Since the BFS changes is determined by a mix of temperature and strain changes, in case both are expected they can be discriminated by performing the same measurement in parallel with two sensing fiber, one that is subject

to both strain and temperature variation (by being bound to the source of both) and one that is let loose and thus is only subject to temperature variation.

- In the configuration known as Brillouin loss, the CW light acts as the pump in the SBS process and is upshifted by a frequency amount $\Delta\nu$ from the pulsed light, which in this case acts as a probe, at frequency ν_0 [4, 24]. The configuration then works exactly as the Brillouin gain one, except that in this case the pulsed probe is amplified through SBS by the CW pump, which is depleted as it travels along the fiber. The BGS distribution in the fiber is obtained by determining the loss from the pump trace at different $\Delta\nu$ values. From the BGS distribution the temperature and strain values are extracted like the Brillouin gain configuration. It is to note that in this case, in order to obtain a strong depletion, the CW pump must have an intensity that is much lower compared to the pulsed probe [24]. Aside from that, the two configurations provide equivalent results.

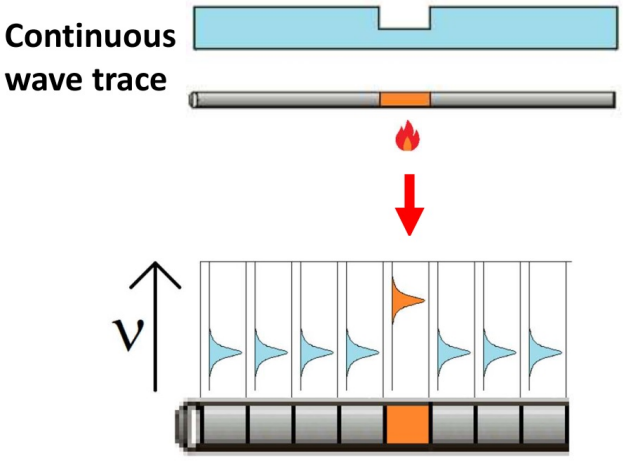

Figure 1.6: Schematic representation of the correspondence between the continuous wave trace and the sensing fiber.

A schematic representation of the pump and probe wavelengths and Brillouin gain/loss spectra is shown in figure 1.7 on the facing page.

1.3.1 Theoretical modeling

In order to reconstruct the BGS, it is assumed that when one of the two waves is pulsed, the gain is proportional to the BGS itself. In this example

the BOTDA system will be assumed to work in Brillouin gain configuration (pulsed pump, CW probe), but similar results apply for Brillouin loss.

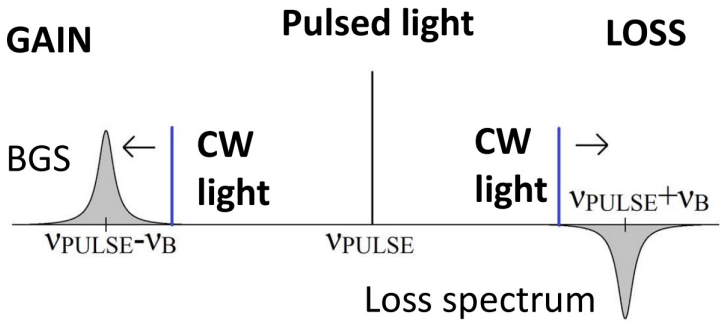

Figure 1.7: Brillouin gain and loss configurations for BOTDA.

To see that this is the case, the process can be modeled in the following way: assuming steady-state conditions and that the pulse is longer than the phonon lifetime ($\sim 10\,\text{ns}$), the equations (1.21) can be used [3, 65],which are reported again here.

$$\frac{dI_P}{dz} = -g\left(z, \Delta\nu\right) I_P\left(z\right) I_S\left(z\right) - \alpha I_P\left(z\right) \tag{1.24}$$

$$\frac{dI_S}{dz} = -g\left(z, \Delta\nu\right) I_P\left(z\right) I_S\left(z\right) - \alpha I_S\left(z\right) \tag{1.25}$$

Compared to (1.21), the term $\alpha I_{P,S}(z)$ has been added, which represents fiber attenuations with coefficient α. The term is positive for the probe equation since this propagates in the $-z$ direction (from $z = L$ to $z = 0$).

This system of equations can be solved through a perturbative method: first, if it's assumed that no pulse is interacting with the probe, it is only affected by fiber attenuation, and the solution to (1.25) simply becomes:

$$I_S\left(z\right) = I_S\left(L\right) \exp\left[-\alpha\left(L - z\right)\right] \tag{1.26}$$

where $I_S(L)$ is the initial probe power entering the sensing fiber at $z = L$. Using (1.26), a solution for (1.24) can be found:

$$I_P\left(z\right) = I_P\left(0\right) \exp\left(-\alpha z\right) G\left(z, \Delta\nu\right) \tag{1.27}$$

where $I_P(0)$ is the initial probe power entering the sensing fiber at $z = 0$ and $G(z, \Delta\nu)$ is a factor that describes the depletion of the pump due to SBS interaction with the probe, and is given by:

$$G\left(z, \Delta\nu\right) = \exp\left[-\int_0^z g_B\left(\xi, \Delta\nu\right) I_S\left(L\right) \exp\Big[-\alpha\left(L - \xi\right)\Big] d\xi\right] \tag{1.28}$$

where the Brillouin gain coefficient $g_B(z, \Delta\nu)$ depends on the pump-probe frequency shift $\Delta\nu$ and the fiber location z through the BFS $\nu_B(z)$ which is generally different at every point of the fiber. Its form is analogous to the one derived in (1.22):

$$G\left(z, \Delta\nu\right) = g_{B0} \frac{\left(\Delta\nu_B\right)}{\left[\Delta\nu - \nu_B\left(z\right)\right]^2 + \left(\frac{\Delta\nu_B}{2}\right)^2} \tag{1.29}$$

where $\Delta\nu_B$ is the FWHM of the BGS (or BGS linewidth) and g_{B0} is the peak gain.

The equations in (1.27) and (1.28) can be inserted into equation (1.25) to find the unperturbed solution, by integrating over Δz, which is the length of fiber over which the pump and probe interact, corresponding to the length of fiber occupied by the pump at the same time and determines the ultimate spatial resolution of the BOTDA sensor. The following integral is obtained [5, 63]

$$\int_{I_s(z)}^{I_s(z+\Delta z)} \frac{dI_S\left(\xi, \Delta\nu\right)}{I_S\left(\xi, \Delta\nu\right)} = \int_z^{z+\Delta z} \Big[-g_B\left(\xi, \Delta\nu\right) I_P\left(\xi, \Delta\nu\right) + \alpha\Big] d\xi \tag{1.30}$$

which results in

$$\frac{I_S\left(z+\Delta z, \Delta\nu\right)}{I_S\left(z, \Delta\nu\right)} = \exp\left\{\int_z^{z+\Delta z} \Big[-g_B\left(\xi, \Delta\nu\right) I_P\left(\xi, \Delta\nu\right)\Big] d\xi\right\} \exp\left(\alpha\Delta z\right) \tag{1.31}$$

Through (1.31) and (1.27), it is possible to estimate the ampified probe light increase that will reach the detector at $z = 0$ at a certiain time t, defined as $\Delta I_S\left(z = 0, t, \Delta\nu\right)$, which is compared to the the pump light intensity in the absence of Brillouin interaction, according to:

$$\Delta I_S\left(t, \Delta\nu\right) = \left|I_S\left(z = 0, t, \Delta\nu\right) - I_S\left(L\right) \exp\left(-\alpha L\right)\right| \tag{1.32}$$

Adding (1.31) in (1.32), the following result is obtained:

$$\Delta I_S\left(t, \Delta\nu\right) = I_S\left(L\right) \exp\left(-\alpha L\right) \left\{\exp\Big[-\int_{tv_g\,/\,2 + \Delta z}^{tv_g\,/\,2} \Big(g_B\left(\xi, \Delta\nu\right) I_P\left(\xi, \Delta\nu\right)\Big) d\xi\Big] - 1\right\} \tag{1.33}$$

where t is equal to $2z\,/\,v_g$ and can take a value between 0 and $2(L-\Delta z)\,/\,v_g$ [65], while v_g is the group velocity of the light in the fiber. It can be easily seen that the integral indices in (1.33) are simply the ones in (1.31) converted into time.

When the gain factor $G\,(z,\Delta\nu)$ from (1.28) is close to 1 for any value of $\Delta\nu$ and z, the depletion on the pulsed pump caused by the power transfer to the probe is small, so that the pulse intensity can be approximated to change almost exclusively due to the fiber attenuation. In this case ΔI_S values are small and thus the exponential term in (1.28) can be linearized, leading to:

$$\Delta I_S\,(t,\Delta\nu) \propto \int_{tv_g\,/\,2+\,\delta z}^{tv_g\,/\,2} g_B\,(\xi,\Delta\nu)\,I_P\,(\xi,\Delta\nu)\,d\xi \tag{1.34}$$

By (1.34), the BGS at position z can be reconstructed directly from the difference $\Delta I_S\ (z=0,t,\Delta\nu)$ between the probe amplified at $t=2z\,/\,v_g$ (where $t=0$ is the moment when the pump pulse enters the fiber at $z=0$) and the unamplified probe. This difference has the same spectral shape of the BGS defined by $g_B(z,\Delta\nu)$ at the respective fiber location z, allowing for the reconstruction of the BGS distribution along the sensing fiber by measuring the trace for different values of $\Delta\nu$. Similar results can be obtained for the Brillouin configuration by putting a – sign in front of $g_B(z,\Delta n)$ to represent the depletion of the continuous wave and renaming I_S with I_P and viceversa to represent the continuous wave pump and the pulsed probe.

2

BOTDA employing a Long Cavity Brillouin Ring Laser Source (LC-BRL)

2.1 Sources employed for classical BOTDA

In order to reliably determine the BGS along every point of the sensing fiber, the choice of the sources that will provide the pump and probe lights is crucial. In particular, any source couple must satisfy these key requirements:

- Low intensity noise: since the intensity of the amplified probe trace will be dependent to the intensities of both the pump and probe signals, the accuracy of BOTDA measurements will be directly dependent on the intensity noise of the source. As a result, low noise laser sources, such as Distributed Feedback (DFB) lasers are required. In addition, since a single measurement event, including the averaging process, might have a duration in the order of milliseconds, the outputs must be stable for a similar timeframe.
- High tunability: since the BFS is expected to shift due to temperature or strain changes, to ensure that the BGS can always be reconstructed the pump-probe frequency shift must be swept over a range of around 100–200 MHz. As a result, the sources must allow for one of the signals (usually the probe) to be tunable over the same range.
- High pump-probe shift stability and accuracy: since the pump-probe frequency shift is the parameter that determines the extent of the Brillouin amplification, the frequency difference of the two sources must be prevented from drifting during the measurement event. This generally means that the two sources must be connected together in some way,

either by a control system or by having other elements in common. In addition, the frequency shift must be as close as possible to to the one set by the user.

The most prominent ways to provide pump and probe lights that satisfy these requirements and have seen the most employment are two: the optical sideband generation (OSB) method [71] and the phase-locked loop (PLL) systems [9].

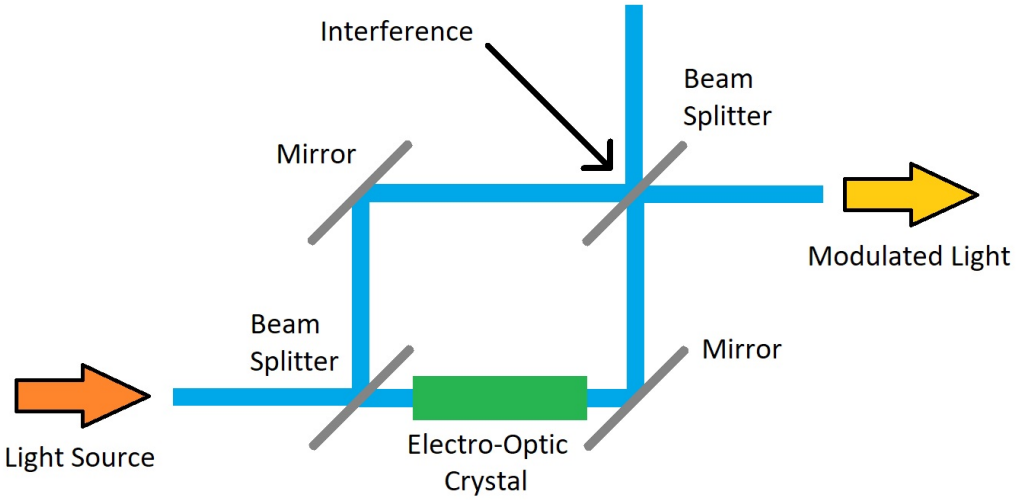

Figure 2.1: Scheme of the Mach-Zender electro-optic modulator (MZM).

2.2 Optical sideband (OSB) method

In the OSB method, which is now the most commonly employed, both the pump and probe light are originated by a single laser source, which is split in two branches, the pump and probe, by an optical coupler. The frequency difference between the two branches is then obtained by passing the probe through a Electro Optic Modulator (EOM). This device consists of a Mach-Zender interferometer (schematically shown in figure 2.1) where one of the branches consists of an electro-optic crystal (for instance $LiNbO_3$) whose refractive index changes with applied voltage. As a result, by changing the voltage it is possible to change the type of interference at the end of the interferometer, and it is thus possible to modulate the intensity of the incoming light.

If the frequency spectrum of the incoming light is composed of a single band at frequency ν_0, when the voltage applied to the Electro-optic crystal is a RF signal oscillating at a fixed frequency ν_m, the spectrum of the exiting light is split into two sidebands, simmetrically distant from ν_0 by an amount equal to ν_m, as shown in figure 2.2a on the following page. By adding a constant voltage bias at a suitable value, it is possible to maximize both constructive and destructive interferences when the oscillating RF signal reaches its maximums and minimums, thus suppressing the band at ν_0 (fig. 2.2b on the next page).

This way, the pump branch has now two sidebands which are respectively downshifted and upshifted from ν_0 (which will be the pump frequency) by exactly ν_m.

Thanks to the characteristics of this scheme, only a single high-quality laser source is required to provide both lightwaves, satisfying the low intensity noise requirement. The probe light is obtained through MZM with a bandwidth of 10–12 GHz and a suitable oscillating signal provided by a microwave signal generator, which allows for an easy tunability of the shift over the needed 100–200 MHz range, since it can be directly controlled by the frequency driving the modulator. Finally, the pump-probe frequency shift is automatically stabilized, since the probe will always be shifted from the pump by the same frequency amount.

2.3 Phase Locked Loop (PLL) method

In the PLL method (shown in figure 2.3 on page 27), which was one of the first developed for BOTDA, the pump and probe sources are obtained by a fixed laser and a tunable laser respectively emitting at the pump and probe frequencies ν_p and ν_s. Through the use of two optical couplers part of the two lights is coupled into the same fiber, where their interference creates a beating signal with two different spectral components oscillating at frequencies $\nu_p + \nu_s$ and $\nu_p - \nu_s$ respectively, connected to a fast photodetector (10 GHz bandwidth). Since the $\nu_p + \nu_s$ component has a frequency of hundreds of THz, only the $\nu_p - \nu_s$ component is detected. By monitoring its frequency, for example through a microwave frequency counter, it is possible to monitor the shift of the two sources and provide a feedback response to the tunable probe source to maintain the pump-probe shift at the desired value. This source limits intensity fluctuations by employing low-noise, high-quality laser sources, provides wide tunability through the use of a tunable laser source and mantains a stable pump-probe frequency shift thanks to the control system.

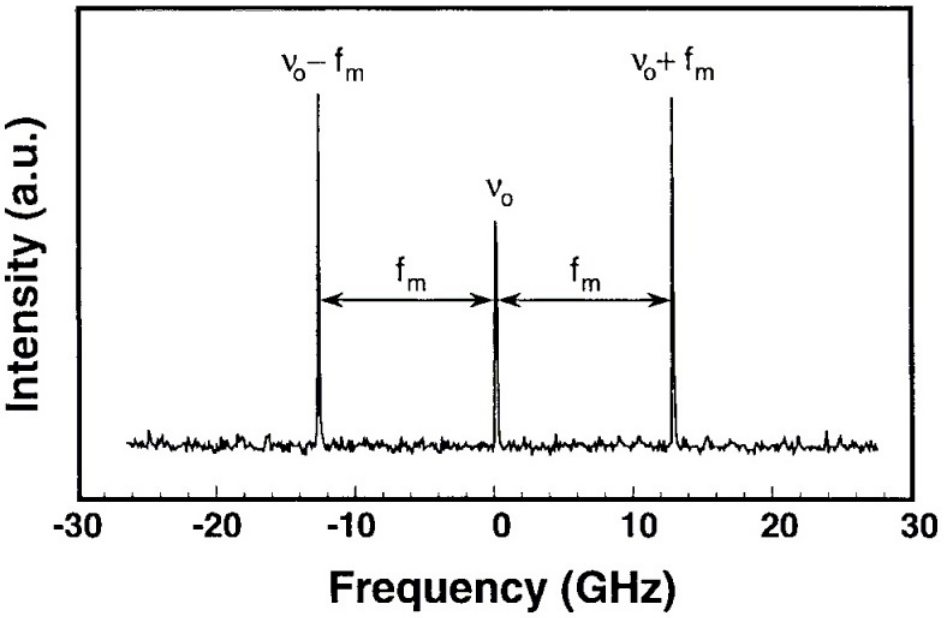

(a) Central carrier frequency ν_0 and modulation sidebands $\nu_0 \pm \nu_m$.

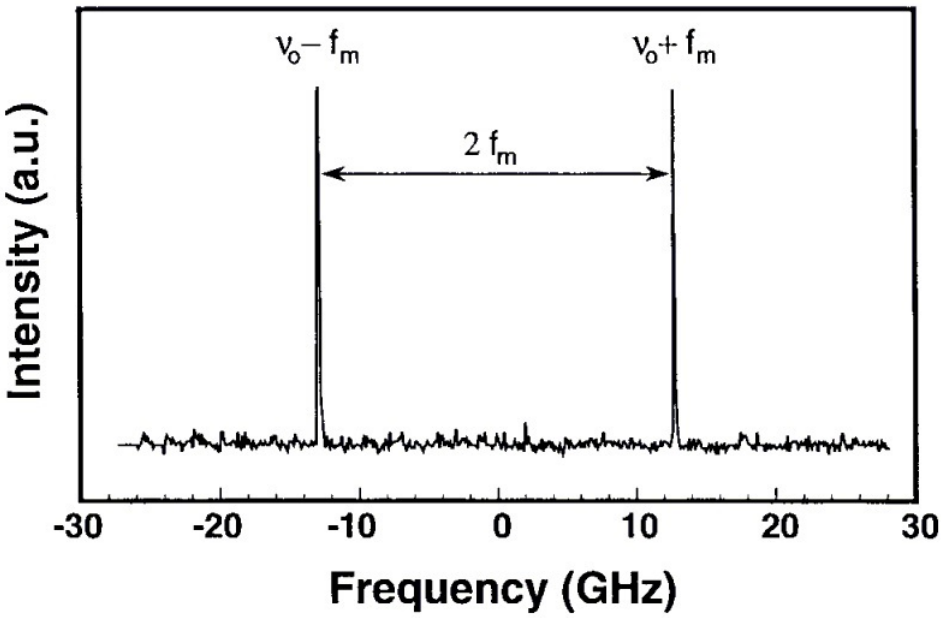

(b) Optimal carrier suppression.

Figure 2.2: Spectrum of the frequency shift from single-frequency laser modulated by a MZM. From [71].

While both techniques mentioned above have proven to result in effective sources for BOTDA techniques, they still have limitations. First of all, both systems require expensive components in order to function correctly. In particular, sources based on the PLL method require two high quality laser sources, one of the two must also have a frequency that is both tunable with a high accuracy and over a wide enough frequency range, while also requiring a frequency measurement system and multiple RF generators for the frequency locking system. In addition, the complexity of the system causes issues for long term stability and accuracy for the frequency shift. Schemes based on the OSB method require a significantly less complex design, and thus are inherently more reliable, but still require an EOM with a bandwidth greater than 10 GHz. The cost of these components adds to the cost of the interrogator equipment and constitutes one of the main obstacle to a large scale employment of BOTDA sensors.

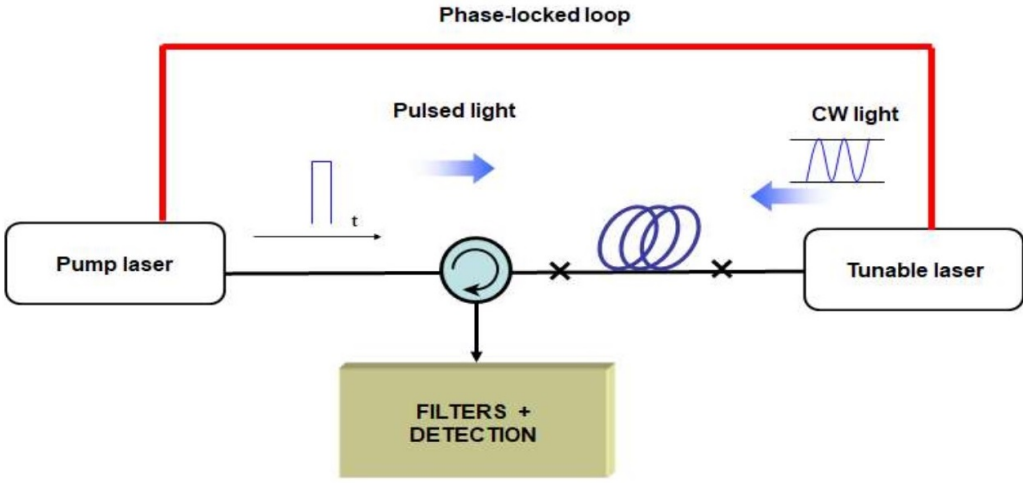

Figure 2.3: PLL stabilization scheme.

2.4 Other sources

To solve the issue shown above, research has focused on finding pump-probe signals sourcing methods that can offer a viable alternative to the OSB and PLL techniques while remaining cost-effective. For instance, several works explored the possibility of using only one modulator to generate both the pump and probe lights, instead of the two required for OSB (one for the probe and one to shape the pump into pulses). To cite an example, [43] showcased a BOTDA sensor which used a pulsed RF signal with a single

externally modulated DFB laser commonly employed in telecommunications, which generates a continuous wave (the probe) and two pulsed sidebands (one of which will be the pump) which, through passive optical methods, are made counterpropagating and used for BOTDA measurements. In [92] Song et al. proposed a design in which both the pump and probe waves were generated by the same laser diode at different times and then made to enter the sensing fiber at the same time through an appropriate choice of delay.

Another approach to reducing costs is to generate a downshifted probe without the use of an electro-optic modulator or an additional laser source. One possible way to achieve this is to take advantage of nonlinear scattering phenomena which can take place in optical fibers. This can be done through the use of fiber lasers, which are tracts of fibers which can produce a light output by scattering an original light signal (called seed pump) provided by a laser source. Among the possible scattering processes which can be used, the most efficient choice is to use SBS to produce light that is already downshifted by a frequency shift that will already be close to the Brillouin Frequency Shift. This type of fiber lasers is knwon as Brillouin Fiber Lasers (BFLs).

2.5 Brillouin Ring Lasers

In their simplest design, Brillouin Ring Lasers, (BRLs) are a variety of BFLs consisting of a length of single mode fiber closed into a ring by a 2-by-2 directional couplers. This type of directional couplers consists of two different fibers fused together to their core, so that when light passes through one fiber, a fixed fraction of it, known as the coupling ratio coefficient κ, is diverted into the other fiber.

When a sufficiently intense light (called seed pump) is injected by an external source into the coupler, part of it is coupled into the loop, where it triggers spontaneos and subsequently stimulated Brillouin scattering, creating a downshifted, counterpropagating light (called Stokes output) which is extracted through the same coupler.

The main advantage of closing the fiber laser into a loop is that the fiber ring acts as a resonant cavity [98]: when the length of the ring and the wavelength of the seed pump are properly tuned, the phase difference between the seed pump entering the ring and the one that remains in the ring after having made a round trip is an integer multiple m of 2π, and thus they interferes constructively.

In particular it can be seen that if κ is the coupling coefficient, $\beta(\omega)$ is the

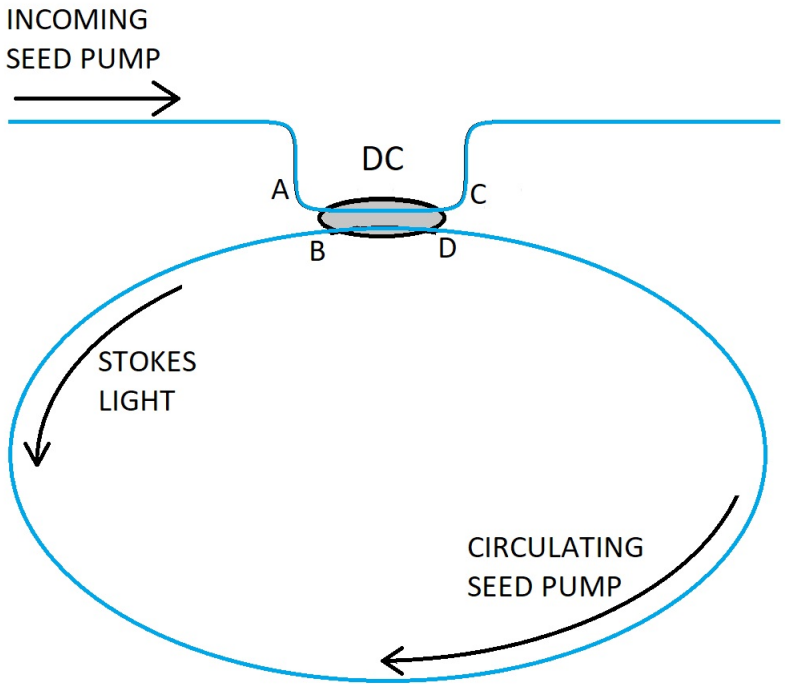

Figure 2.4: Brillouin Ring Laser scheme.

fiber's propagation constant and L is the fiber length, the resonant conditions are the ones that maximize the light intensity at entry D in figure 2.4 while minimizing the one from entry C. These conditions can be expressed as [98]

$$\beta L = 2\pi m - \frac{\pi}{2} \tag{2.1}$$

$$\kappa = (1 - \gamma_0) \exp(-2\alpha L) \tag{2.2}$$

The first formula simply represents the phase requirement to have constructive interference every round trip. The $\pi / 2$ term must be added since the every time light gets coupled out from the coupler it experiences a $\pi / 2$ phase increase.

The second formula represents the optimal coupling coefficient, in which γ_0 is the fraction of power lost due to the coupler (fractional coupler intensity loss) and α is a coefficient that determines the percentage of light intensity lost for every unit of fiber length, known as the fiber's amplitude attenuation coefficient.

It can be also seen that the fiber ring functions exactly like a narrow-band Fabry–Perot resonator, which is a resonant cavity closed by two mirrors with reflectivities $R = \kappa$ and $1 - R = 1 - \kappa$. These resonators are characterized by

a coefficient called finesse F, which determines how effective the resonator is at escluding all non-resonant frequencies and is defined as:

$$F = \pi\sqrt{\frac{R}{1-R}} = \pi\frac{\kappa}{1-\kappa}\dots \tag{2.3}$$

Thanks to the resonant behavior of the ring laser, the seed pump intensity keeps increasing until dispersion losses experienced each round trip (which depend on the power of the incoming light) become equal to the power being injected. As a result, the fiber laser becomes much more efficient, greatly reducing the seed pump threshold power, that is the minimum seed pump power required to trigger stimulated Brillouin scattering and obtain a Stokes output.

In particular, in a BRL the threshold power is the seed pump power necessary to increase the Stokes output's intensity through SBS amplification by an amount equal to the losses it would experience in a round trip loss and is found to be dependant on the cavity length and the fiber through the relation, (where g_B is the fiber Brillouin gain coefficient and A_{eff} is the effective core area of the fibers making the ring) [98]:

$$P_{\text{thresh}} = 2\pi^2\frac{\frac{A_{\text{eff}}}{g_B}}{F\cdot L} \tag{2.4}$$

As can be seen from the equation, the threshold power is greatly reduced by either increasing the finesse or the cavity length, and shows how a BRL can have a significantly lower threshold power compared to open-loop Brillouin fiber lasers. In numerical terms, while open-loop BFLs with lengths above 20 km have threshold powers of tens of mW, properly designed Brillouin Ring Lasers with lengths of a few meters can achieve laser pump thresholds in the order of mW or lower. Using the model mentioned above and developed in [98], the calculated threshold power as a function of length for different coupling coefficients (ranging from 90 to 95 %), which determine the finesse value, is shown in figure 2.5 on the facing page. From the figure it can be easily seen how increasing both length and finesse values positively affect the threshold power. In this model, the values used for the Brillouin gain coefficient and effective area of the fibers were the ones taken from the experimental condition (see below), which were $g = 5.4\cdot 10^{-11}\,\text{m}\,/\,\text{W}$ and $A_{\text{eff}} = 6.0\cdot 10^{-12}\mu\text{m}^2$.

It is to note that when the seed pump exceeds the threshold power most of its intensity is reduced as it fuels the SBS process along the ring to amplify the Stokes output. This factor is neglegible for few-meters length and wasn't

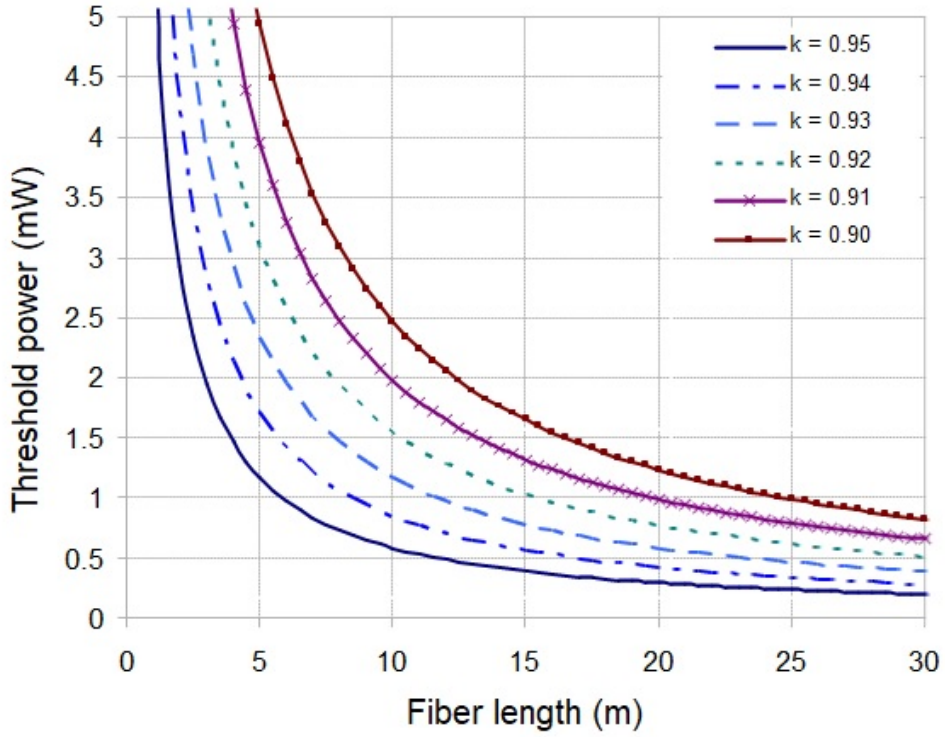

Figure 2.5: BRL threshold power as a function of ring length at different coupling coefficient values κ.

considered in the evaluations above, but puts a limit on the length of the fiber length that can be employed.

Another issue to consider is that while in general the threshold power and the conversion efficiency (that is the Stokes output power as a function of seed pump power) are linked, a high coupling ratio, and thus a high finesse also means that only a small component of the Stokes output is extracted from the ring to be used for any application. Because of this, while in teory a coupling ratio as close as 1 should be desirable, in realistic application it will always be around 90–95 %.

2.6 Hybrid Brillouin ring lasers

As was shown above, Brillouin Fiber Lasers have important properties, such as a low threshold voltage and a narrow linewidth, but have a series of limitations. First of all, they require the ring length and the seed pump wavelength to be resonant, and produce a small output power. Furthermore, the addition

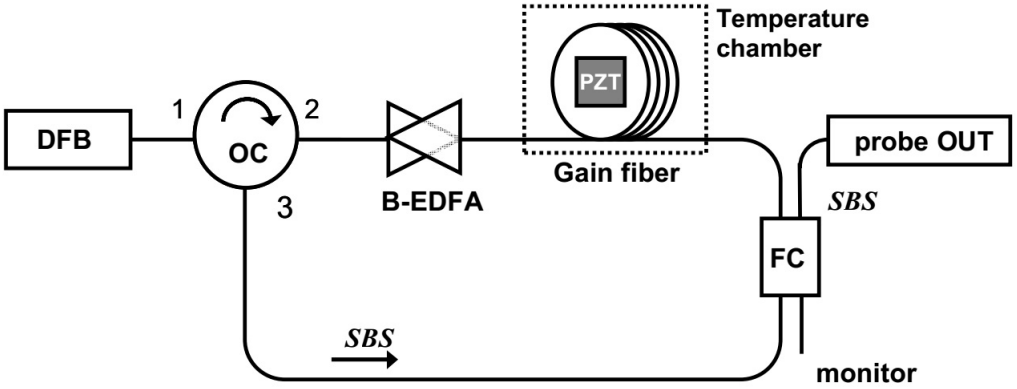

Figure 2.6: Long Cavity hybrid BRL laser scheme (LC-BRL).

of other optical components in the ring resonator is difficult due to the inherent losses associated with adding fiber connections. A way to overcome the need for a resonant, critically coupled Brillouin Ring Laser resonator is to greatly increase the cavity length, to the point where a single round trip produces enough Stokes output power that can be amplified through a different gain method, such as erbium-doped fiber lasers [17]. Erbium-doped fibers are the main component of Erbium Doped Fiber Amplifiers (EDFAs) which when pre-pumped can greatly amplify an incoming wave. With this hybrid approach, large output powers are achievable, while also maintaining the natural frequency shift of the output. It is to note that in this approach the seed pump is no longer necessarily resonant with the ring length. For the Stokes output to be resonant, there must be cavity resonant modes that intersect with the BGS. As will be seen below, at the lengths employed in this type of ring lasers (which ranges from hundreds of meters to kilometers), the spacing of the resonant modes is close enough to always verify this condition.

An example of a hybrid Brillouin ring laser layout, is shown in figure 2.6. The seed pump is provided by a DFB laser with a $\sim 1.25\,\mathrm{MHz}$ linewidth and emitting at $\lambda = 1.551\mu\mathrm{m}$, and is injected into the ring by an optical circulator, which allows passage of light only from port 1 to port 2 and from port 2 to port 3, which allows the Stokes output to recirculate while preventing the seed pump from doing the same. The ring is composed of 2 km of single mode fiber and incorporates a bi-directional Erbium Doped Fiber Amplifier (B-EDFA) [22], whose function is to both boost the seed pump for increased SBS scattering and to amplify the Stokes output itself, improving both threshold power and conversion efficiency. Part of the Stokes output is estracted from the ring through the use of an optical fiber coupler (FC, 95/5

splitting ratio) to be employed in other applications or to be analyzed with an optical spectrum analyzer (OSA), while the rest recircolates into the ring through OC exits 2 and 3.

Another interesting feature of this setup is that, since the seed pump resonance is no longer a requirement, the wavelength of the Stokes output can be tuned by using a piezoactuator (PZT) to apply controlled strain changes to the fiber in order to change its BFS and thus shift the Stokes output frequency. Since in this situation the temperature and strain conditions of the fiber become relevant, the BRL must be placed in a temperature-controlled environment to leave the controlled strain as the only factor determining the BFS.

By the way it's designed, the hybrid BRL, which can also be called Long cavity BRL (LC-BRL), satisfies two of the three requirements mentioned at the beginning of the chapter: it allows from the production of two lightwaves (one being the base seed pump) with a frequency shift which is both stable (since it will always be equal to the BFS of the fiber) and tunable. To evaluate whether the noise is acceptable, specific characterization of the source have to be carried out.

2.7 Implementation of the Long cavity Brillouin Ring Laser

To evaluate the quantitative properties of the LC-BRL shown in the previous section, the Stokes output has been characterized in different ways.

2.7.1 Threshold power and conversion efficiency

Using a power meter, the intensity of the Stokes output was measured at different seed pump powers. From the results, which are shown in figure 2.7 on the following page, the threshold power was found to be $\sim 2\,\mathrm{mW}$, while the Stokes output increased with the pump power up to $\sim 0.5\,mW$ at the maximum available seed pump power of 17 mW, which as probe power is sufficient for a variety of BOTDA applications [25].

2.7.2 Stokes output linewidth

In BOTDA applications, the linewidths of the pump and probe are both important factors for overall performance. First of all, the linewidth of the probe light must be small enough to allow an effective reconstruction of the BGS: if most of the power of the probe or the pump is spread over a few

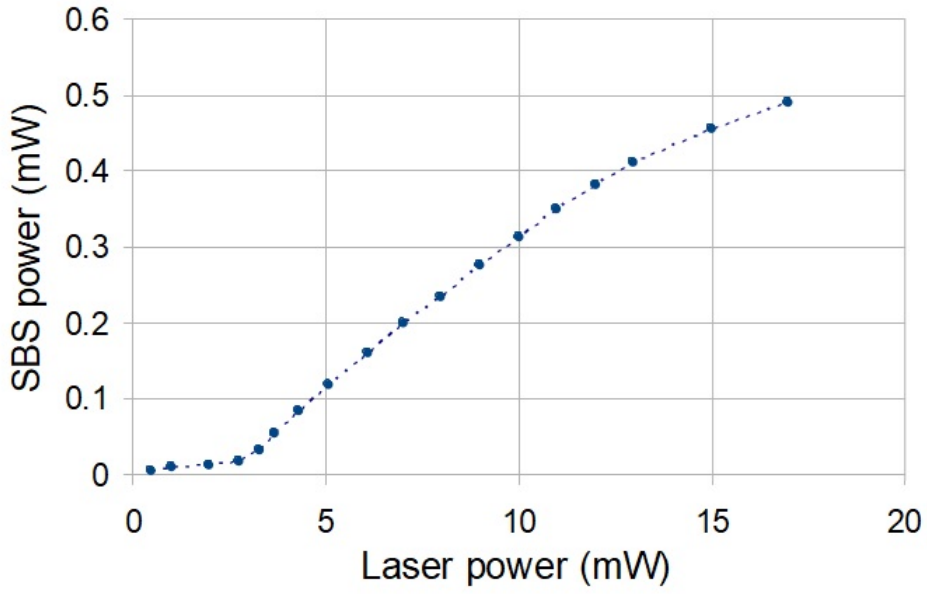

Figure 2.7: LC-BRL output power as a function of seed pump power.

MHz, a change of 1 MHz in pump-probe frequency shift will not change the Brillouin amplification significantly, thus greatly reducing the frequency shift resolution of the measured BGS, which will be consequently "smoothed". As a result, the linewidth of the probe and pump shouldn't be wider than the expected scanning step of the frequency shift which will be used in experiments. In addition, a narrow linewidth provides a reduced noise in the measured Brillouin gain even when it is much lower than the linewidth of the BGS [62].

To determine the validity of the hybrid BRL source it is thus necessary to determine the effect it has on the Stokes output linewidth compared to the seed pump linewidth. To do so, the Stokes output spectrum was obtained through the use of the self-heterodyne technique, which is shown in figure 2.9 on page 36. This technique involves using an optical coupler (OC) to send the Stokes output through different optical paths: one short and one with a greatly increased length to create a delay. The light going through the short path is sent through an acousto-optic modulator (AOM), a device similar to the electro-optic modulator which is driven by a costant frequency of $40\,MHz$, which shifts all the light's spectral components by that amount. At the end of both paths they are united through another optical coupler. If the delay created in the longer path is sufficient, the lights coming from the two paths will be uncorrelated and once coupled together they will beat with each other [34]. If a photodetector is used to detect this beating and the signal is inserted

into an electrical spectrum analyzer (ESA, which in the experiment had a resolution of $< 500\,\text{kHz}$), the final obtained spectrum will be the original light's spectrum convolved with itself and centered at the AOM frequency (in this case 40 MHz), allowing to estimate its linewidth.

The measured full-width half maximum (FWHM) for the linewidth (shown in the inset in figure 2.8, displayed on the ESA at 10 MHz per frequency division) was found to be $\sim 2.5\,\text{MHz}$, or one tenth of the BGS linewidth, which is sufficient for BOTDA measuring with a pump-probe frequency shift step of 1 MHz.

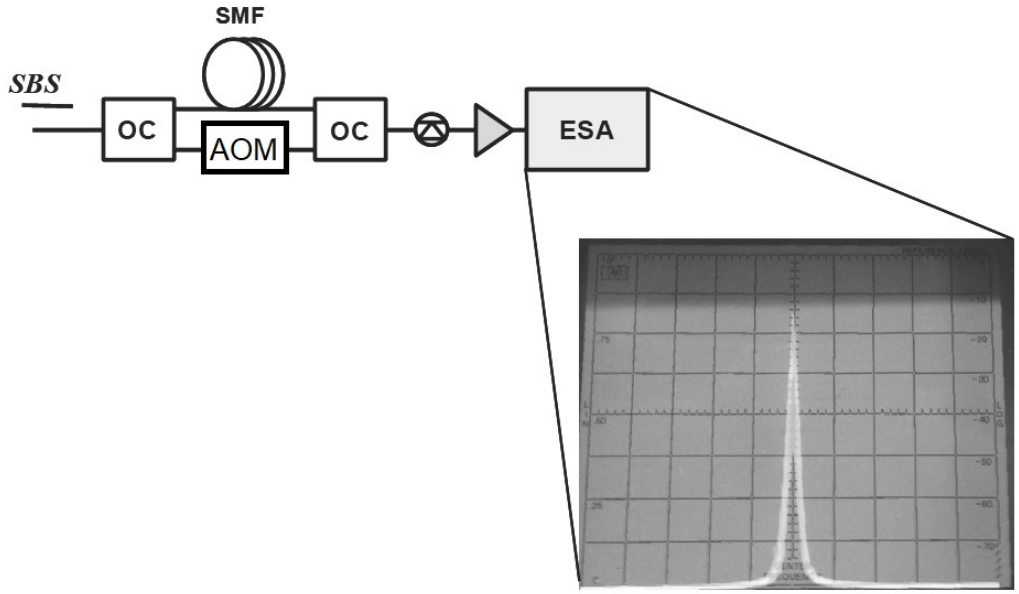

Figure 2.8: Self-heterodyne technique scheme. Inset: extracted probe light spectrum as output from the ESA.

Since the linewidth of the seed pump laser was 1.25 MHz, it can be seen that the stokes output linewidth has doubled the one from the light it originated from. In absence of resonant processes, the linewidth should be equal to the linewidth of the typical BGS (15–20 MHz) [53]. The fact it is one order of magnitude lower and relatively similar to the FWHM of the seed pump can be attributed to the resonating behavior of the long cavity. This is because at each round trip of the long cavity only the frequencies corresponding to the resonant modes experience constructive interference and thus become dominant to the other ones. Because of this, all resonators also act as filters with the ability to reduce the linewidth of the light put through them.

2.7.3 Intensity noise measurement

Finally, an assessment of intensity oscillations in the BRL source has been carried out. Actually, expected fluctuations in fiber lasers are typically higher than in integrated-photonics diode lasers essentially because of long fiber cavity lengths, resulting in oscillations and reduced stability due to onset of cavity mode hopping, pump-signal noise transfer and other effects [29, 36, 56] In order to evaluate the power fluctuations of the BRL source we measured the relative intensity noise (RIN) value, which is measured as dB / Hz and is defined as the power spectral density of the power fluctuations $\delta P(t)$ of the time-varying signal and can be calculated as a function of the angular frequency $\omega = 2\pi\nu$ in the following form [7, 54, 55]:

$$RIN(\omega) = \frac{1}{\bar{P}^2} \int \langle \delta P\,(t)\, \delta P\,(t+\tau) \rangle \exp\left(-i\omega\tau\right) d\tau$$

where $\bar{P}$ is the average optical power and $\langle\rangle$ brackets define the average over a large number of measurements.

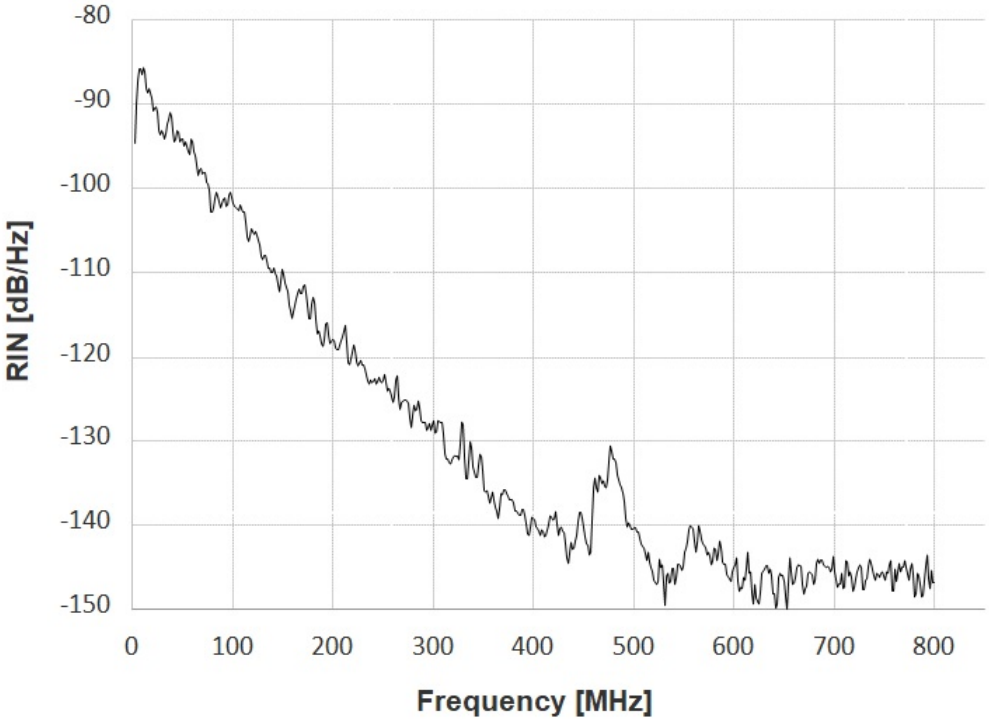

Figure 2.9: RIN spectrum for the BRL output.

In practival terms, RIN measurements were carried out by measuring the BRL Stokes output intensity through a fast PIN InGaAs photodetector

(10 GHz bandwidth). By acquiring the photodetector output through an ESA working up to 15 GHz, the power spectrum $\sigma^2(\omega)$ could be acquired. From this spectrum, the noise profile of the source was obtained by subtracting thermal and shot noise spectrum, which in turn was obtained by acquiring the spectrum of the photodetector output when no light is presence. Finally, the RIN is obtained by normalizing the obtained spectrum to the total output power and the ESA frequency resolution [14, 30, 89].

The measured RIN spectrum is shown in figure 2.9 on the preceding page for frequencies up to 800 MHz. From the graph it can be seen that the intensity noise is higher at lower frequencies, with a maximum of about $-90\,\mathrm{dB}\,/\,\mathrm{Hz}$ in the 10–15 MHz region. Beyond that region, the RIN decreases steadily until the 400–500 MHz region, after which it reaches a minimum of around $-145\,\mathrm{dB}\,/\,\mathrm{Hz}$. This behavior is to be expected from ring lasers, which generally are known have a higher intensity noise values compared to integrated lasers at lower frequencies [36].

2.7.4 Frequency shift tuning system

As said above, a way to achieve frequency tuning needed to reconstruct the BGS in BOTDA measurement in LC-BRL is to impart a varying amount of tensile strain through a piezoactuator (PZT in figure 2.6 on page 32). Since the shift between the seed pump and the Stokes output will be equal to the BFS of the ring fiber and the BFS is linearly correlated to strain changes, it is possible to directly control the frequency shift by controlling the strain generated by the piezoactuator.

The actuators used in the experimental implementation were driven by a DC-voltage generator and can apply a tensile strain in a range from 0 to $\sim 4\,\mathrm{m}\,\epsilon$, which corresponds to a shift tuning range of over ~ 200 MHz, which is required to monitor temperature variations of more than 100 °C and strain variations in the mϵ range. In more detail, the piezoactuator employed was a PZT fiber stretcher consisting of a high-voltage PZT ring around which the ring fiber was wound.

In actual BOTDA experiments, the pump-probe frequency shift was swept by graudally increasing the the PZT voltage by the amount required to obtain 2 MHz step. Sweeping the frequency range in a single direction allowed to avoid any potential hysteresis effect, allowing for a stable and repeatable process. The curve showing the seed pump-Stokes output frequency shift as a function of applied voltage is shown in figure 2.10. It should be noted that

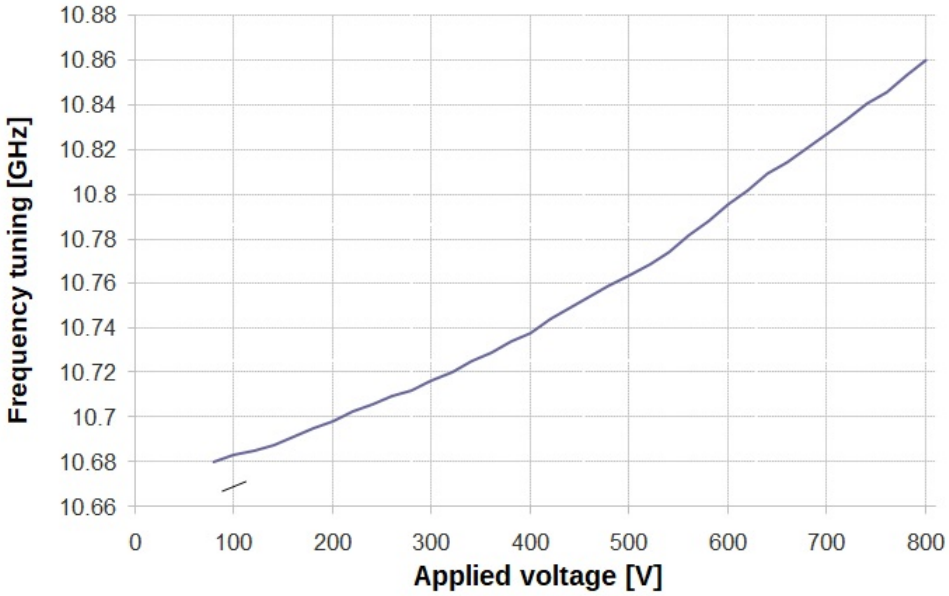

Figure 2.10: PZT tunability system calibration curve for the LC-BRL.

the relation between the applied voltage and the resulting strain (and thus the shift) is not extactly linear, which is to be expected from PZT stretchers. As a result, the curve was used to calibrate the PZT to obtain the voltage needed for the desired frequency shift.

2.8 BOTDA measurement using the LC-BRL source

To evaluate if the performance of the LC-BRL is suitable for distributed Brillouin measurements, a BOTDA implementation employing the LC-BRL source (shown in figure 2.11a) is shown in figure 2.11b on the next page. The light from the DFB laser ($\lambda = 1.55\mu$m, ~ 1.25 MHz linewidth) is split into the pump and probe branch by a 30/70 coupler (in particular, 30 % is sent into the probe branch and 70 % is sent into the pump branch). The light sent to the probe branch is used as a seed pump in the LC-BRL (with a 2.1 km long cavity and an input power of 3 dBm) to create the continuous probe signal, which is then sent into a variable optical attenuator (VOA) so that its power could be set to a value that avoids nonlinear effects and pump depletion [64]. In the experiment, this value was around -2 dBm.

The SBS process is known to be polarization dependant: its efficiency is maximum when the polarization of the pump and probe are aligned and minimum when they are opposite [32]. Since the polarization of both pump

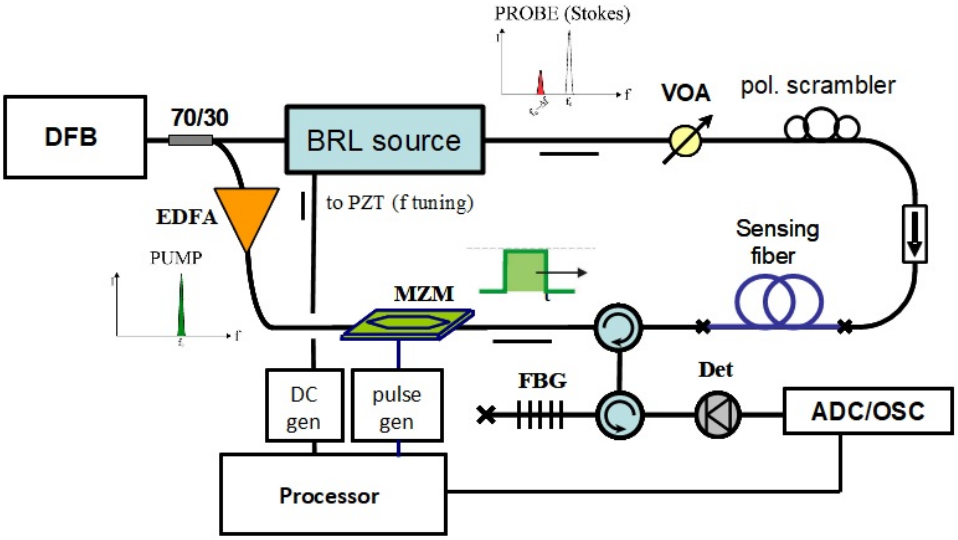

(a) BOTDA scheme.

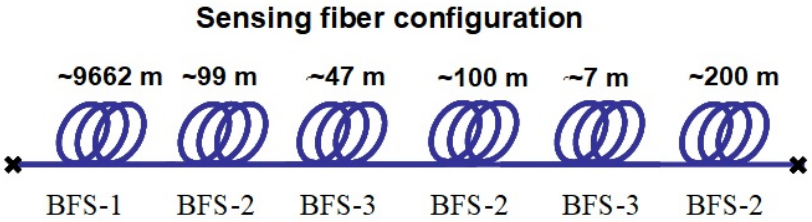

(b) Sensing fiber used for the performance evaluation.

Figure 2.11: LC-BRL implementation in a BOTDA sensing system.

and probe change as they move along the sensing fiber due to effects such as birefringence, the final gain trace obtained in BOTDA measurements is affected by a further degree of noise [16, 33]. To solve this, the probe polarization is randomised through a polarization scrambler. As a result, at every point of the sensing fiber the pump encounters a probe whose polarization is averaged out over all possible positions and the SBS efficiency is similarly averaged at every point of the fiber, resulting in a more stable gain trace.

The light sent in the pump branch was instead amplified by an Erbium doped fiber amplifier (EDFA) and then shaped into a pulsed signal by a MZM (with a bandwidth of 10 GHz), which is driven by an RF pulse with a width of 40 ns and a repetition rate of 7 kHz, generated by a pulse generator whose signal is added to a DC voltage to obtain optimal attenuation in absence of a pulse. Since of the electro-optic effect reaches its peak efficiency when the light is at a specific polarization, the MZM's built-in polarization controller was used to ensure to further optimize the pulse shaping of the pump.

Both the pulse generator and the DC-voltage generator used for the PZT actuators are computer-controlled. The CW probe signal and the pulsed pump signal are coupled with counter-propagating directions into the sensing fiber.

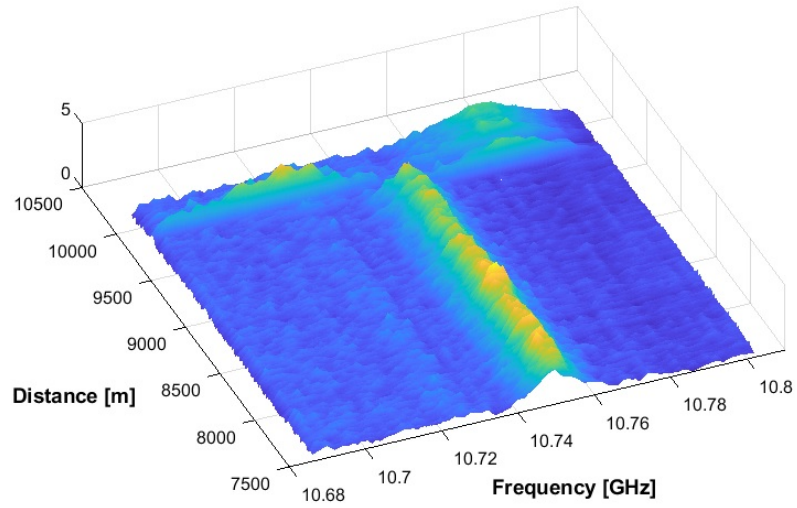

(a) 3D view.

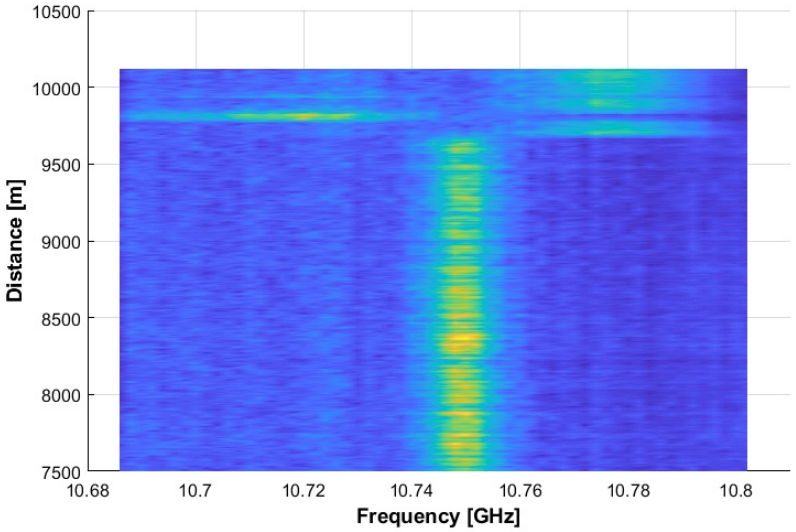

(b) Top view.

Figure 2.12: BGS distribution across the last 2.5 km of sensing fiber.

After the amplification, the probe signal is extracted from the circuit at the end of the sensing fiber through an optical circulator. Here, it was sent through another optical circolator to a fiber Bragg grating (FBG). A fiber Bragg grating is a tract of optical fiber whose core has a refractive index profile which is altered at regular length intervals. This perturbation causes

the grating to reflect incoming light in a narrow range of elements. With an appropriate FBG,only the light at the probe frequency is reflected, while other elements of the incoming light, such as pump light reflected through Rayleigh scattering, is not. The reflected filtered probe light then goes back through the second optical circulator to be detected by a 100 MHz bandwidth photo-detector.

For the experimental demontration, the sensing fiber was composed of several different spools with different BFS values which were spliced together for a total length of $\sim$ 10 km, as shown in figure 2.11b on page 39. This way, it was possible to simulate a situation where the fiber was affected by different temperature/strain conditions across its length. In addition, since the BFS distribution is known in advance, the evaluation of the accuracy of the BOTDA measurement will be facilitated. In particular, the sensing fiber was composed by an initial long segment (9662 m) with a uniform BFS (BFS-1), which was followed by a 99 m long segment with a BFS downshifted from BFS-1 by 30 MHz (BFS-2) and a 47 m long segment with a BFS (BFS-3) upshifted by 20 MHz with respect to the initial fiber. The three remaining segments were a 100 m long one at BFS-2, a 7 m long one at BFS-3 and a 200 m one at BFS-2.

The BOTDA measurement was performed by sweeping the pump-probe frequency shift through the use of the PZT and acquiring a probe trace averaged 1024 times for each frequency. The measured Brillouin gain spectra along the last 2.5 km of the sensing fiber are shown in figure 2.12 on the preceding page. The BGS FWHM linewidths were found to be ranging between 10 and 20 MHz which is comparable to the expected values for a pump pulse of 40 ns. It is to note that the BGS spectrum of different fiber segments, which were possibly manufactured in different ways, can vary significantly.

From these result, the BFS distribution along the fiber was extracted by performing a least-squares Lorentzian curve fit on the BGS at each corresponding fiber position. The BFS distribution for the last 2.5 km of fiber is shown in figure 2.13 on the following page. From the figure it can be seen that the measured distribution correctly displays the one expected from the composition of the different fiber pools: in correspondence of the segments with a BFS equal to BFS-2 (which is 20 MHz higher than BFS-1) a sharp increase of measured BFS can be seen from the initial baseline (corresponding to the initial long segment at BFS-1). Similar result are obtained for BFS-3, with sharp declines of the measured BFS in correspondence of those segments,

including the one with a length of 7 m.

To evaluate the spatial resolution of the BOTDA system, the BFS distribution across the first point of transition between two different fiber segments at BFS-2 and BFS-3, which is the transition between the second and third segment at 9762 m, was taken in consideration (as shown in the inset of figure 2.13). The spatial resolution was defined as the length corresponding to the number of points in the BFS distribution required to go from 10 % to 90 % of the new BFS value. Measured this way, the spatial resolution was found to be around 4 meters, which is the expected value for a pump pulse duration of 40 ns.

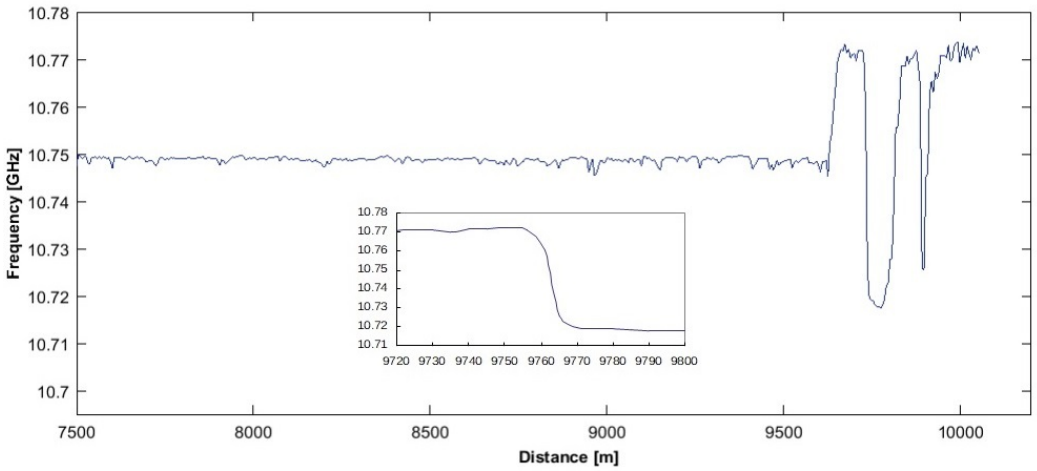

Figure 2.13: Measured BFS distribution along the last $2.5\,km$ of sensing fiber.

The BFS resolution obtained by BOTDA sensing employing the LC-BRL source was calculated as the root mean square error (RMSE) of the measured BFS distribution compared to the expected one. As a result, the BFS resolution was found to be around 0.5 MHz, which corresponds to a temperature and strain resolution of 0.5 °C and 10 $\mu\epsilon$ respectively for most common types of single mode fibers.

From these result, it can be seen that the LC-BRL source can provide a probe signal which is suitable for BOTDA measurements in a range of at least 10 km, while also having the potential of greating reducing the fabrication cost by removing the need of one of the two EOMs: it maintains the pump-probe frequency shift locking due to the inherent nature of BFS while allowing tunability over a 200 MHz range and has an adequate conversion efficiency while having a low threshold power. Finally, the probe signal displays a sufficiently narrow linewidth and allows for acceptable BFS reconstruction

despite an increased intensity noise in the $0 - 500$ MHz frequency range.

The contribution of the author to the work presented in this chapter consists of the theoretical modeling and characterization of the long cavity hybrid BRLs, including the intensity noise, output linewidth, threshold power, conversion efficiency and wavelength tunability. In addition, it includes the experimental BOTDA measurements employing the hybrid BRL source.

3

BOTDA employing a Wavelength-Locked, Short Cavity Brillouin Ring Laser Source

In the previous chapter, a low-cost LC-BRL cavity was showcased and its viability as a probe source for BOTDA measurements up to a 10 km range was demonstrated. Despite this, it was noted that its ultimate BFS, temperature and strain resolutions were limited by three main elements.

- First, the output power of the LC-BRL was overall limited below 1 mW, which reduced the overall range and quality of the BOTDA trace.
- Second, while the linewidth was narrowed compared to the width of the BGS which was expected in absence of resonant filtering, it was still 2 MHz wide, which still has a negative effect on frequency resolution.
- Third, the source had a significant intensity noise increase compared to semiconductor lasers, especially at frequencies below 500 MHz, which is expected to have been the main factor limiting the BFS resolution.

Because of these issues, while offering an attractive alternative in terms of cost reduction, the LC-BRL as a pump source for BOTDA is ultimately limited in terms of performance.

3.1 Noise effects in BRLs

Of the three issues described above, the main limiter to the BFS resolution is ultimately the last one which, as already stated in the previous chapter, is a limit of BRL based sources: due to the nature of fiber ring lasers and SBS,

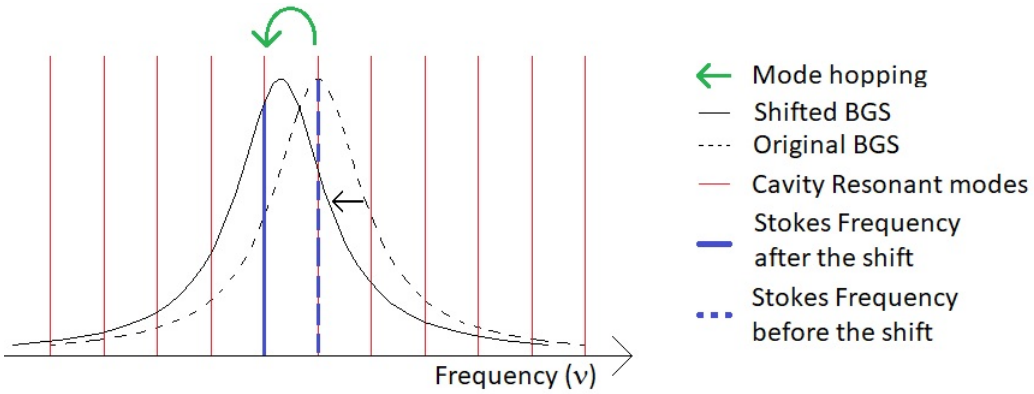

(a) Mode hopping due to shifts in the BGS.

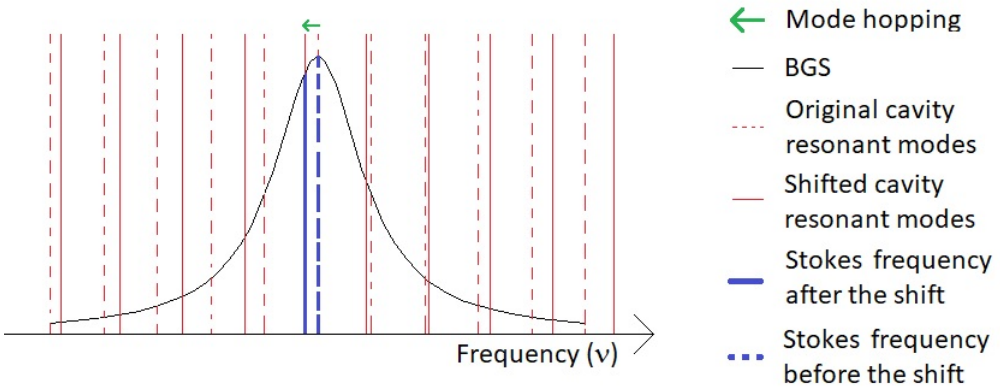

(b) Frequency instability due to shifts in the resonant modes.

Figure 3.1: Mode hopping and frequency instability in BRLs.

the Stokes signal is subject to intensity, frequency and phase noise which tend to degrade its quality [69].

Among the various noise effects (such as Kerr effects and frequency pulling), the most relevant one is the so-called mode hopping effect, which is schematically illustrated in figure 3.1. In a BRL cavity, the frequency of the Stokes output will be the cavity's resonant mode which is closest to the BFS of the fiber, which is known as the dominant mode. In this situation, thermal and acoustic vibrations in the ring continuously cause shifts either in the BFS (figure 3.1a) or in the position of the resonant modes (figure 3.1b) [84]. If the resonant modes of the cavity are too close together, the dominant mode might change, causing a frequency shift and a temporary variation of the Stokes output frequency, causing an increase in both intensity and frequency noise. This effect is the main reason for the increased RIN profiles found in BRL sources compared to semiconductor lasers and also potentially contributed to

increase the output linewidth (which in the previous chapter was found to be twice the linewidth of the seed pump). In addition, if more than one resonant mode is close enough to the BFS, the Stokes output frequency could be a superposition of all those modes, further broadening the frequency linewidth (this effect is known as multi-mode lasing).

To eliminate both of these effects, the cavity resonant modes should be sparse enough that only one of them lies inside the BGS at all times [81, 97]. When this happens, even if the BFS experiences small shifts the dominant mode will always remain the same (as shown schematically in figure 3.2).

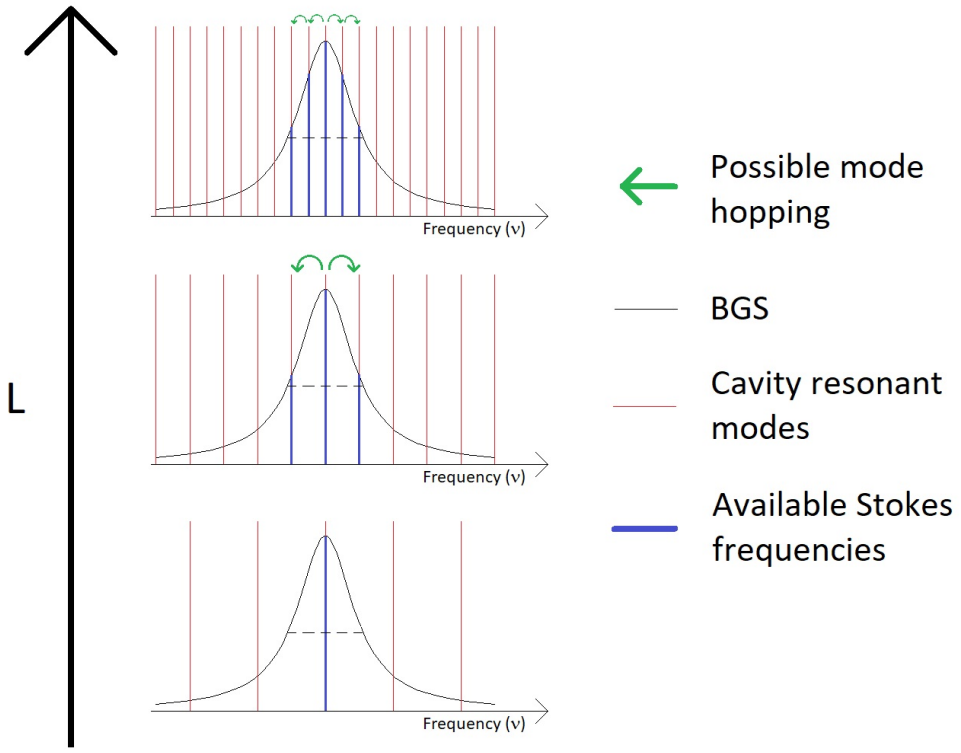

Figure 3.2: Mode hopping with decreasing cavity length.

The spacing between resonant modes, known as the free spectral range (FSR) is given by [61]:

$$FSR = \frac{c}{n \cdot L}$$

where n is the fiber core refractive index (equal to 1.5 for most standard telecom fibers), c is the speed of light and L is the length of the cavity. From this formula, it can be seen that the only way to increase the FSR is to reduce the length of the ring cavity [84]. In particular, using the relation above, to

extend the FSR to be greater than the linewidth of the BGS (20 MHz), the cavity length should be lower than:

$$L < \frac{c}{n \cdot FSR} \approx \frac{3 \cdot 10^8\, ms^{-1}}{1.5 \cdot 40 \cdot 10^6\, s^{-1}} \approx 10\, m\,.$$

In other words, in order to reliably suppress intensity noise associated with BRL sources, the cavity length should be reduced to the order of a few meters.

Taking into consideration the behavior of the BRL threshold power from the previous chapter, (shown again in 3.3), it can be seen that reducing the cavity length increases the seed pump threshold power and as a consequence also reduces the conversion efficiency due, among other factors, to a reduced amount of gain medium where SBS amplification could take place every round trip.

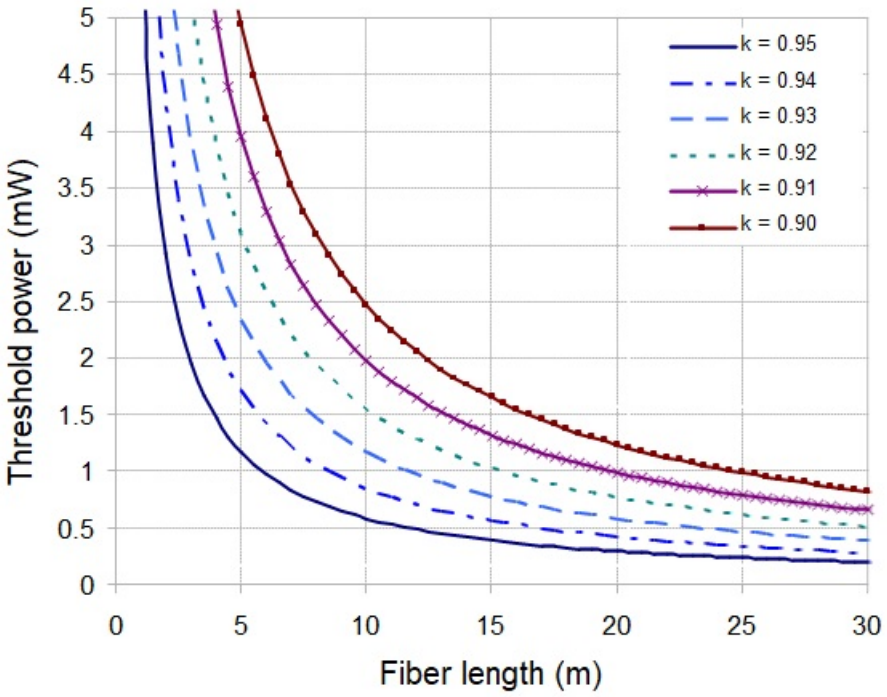

Figure 3.3: BRL threshold power as a function of ring length at different coupling coefficient values κ. From [53].

3.2 Double Resonance

In the treatment of the resonant behavior of the BRL cavity shown in the previous chapter, only the seed pump was taken into account. If the cavity

was to be made resonant for both the seed pump and the Stokes output, it would be said to be in a state of double resonance. When this condition is verified, not only the pump increases in power at every roundtrip until it reaches an equilibrium where the injected pump is equal to the round trip loss, but so does the Stokes output: the light generated by SBS at every round trip interferes constructively with the previously generated light. While in a cavity that is only resonant for the seed pump the Stokes output production is facilitated only because the circulating pump is higher, in a doubly resonant cavity the Stokes output also keeps increasing until it reaches an equilibrium with round trip losses.

3.2.1 Single-cut Technique

To obtain the double resonance condition, the length of the cavity must be finely tuned so that the BFS is equal to m times the FSR, where m is an integer. A possible way to do so for a BRL with a fixed length L, assuming the wavelength of the pump is more or less fixed, is to apply a technique developed in [95] to calculate the amount of length ΔL to be cut from the fiber [85].

To find how to obtain this value, one can proceed as follows: the BFS $\Delta\nu_{\mathrm{SBS}}$ is expressed as:

$$\Delta\nu_{\mathrm{SBS}} = \frac{2nV_a}{\lambda_P}$$

where V_a is the acoustic velocity of the fiber and λ_P is the seed pump wavelength. The condition for double resonance is then written as [59]:

$$\frac{2nV_a}{\lambda_P} = m \cdot FSR = m\frac{c}{n \cdot L}$$

Solved for λ_P the pump wavelength λ_L^k that satisfies the condition for a given L and k is obtained:

$$\lambda_L^m = \frac{1}{m}\frac{2n^2V_a}{c}L \tag{3.1}$$

Relation 3.1 expresses all possible seed pump wavelengths that satisfy the double resonance condition for the cavity, which will be called double resonance peaks. For a given cavity of arbitrary length, these peaks can be found by employing a tunable DFB laser as a seed pump and measuring the Stokes output as a function of the pump wavelength. An example of this

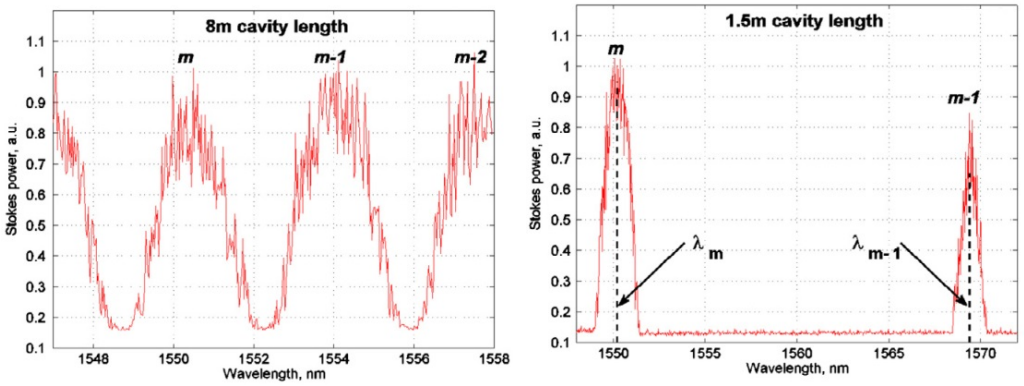

(a) 8 m cavity length. **(b)** 1.5 m cavity length.

Figure 3.4: Measurement of BRL Stokes output as a function of pump wavelength for two different cavity lengths. From [51].

measurement is shown in figure 3.4 on the following page for different cavity lengths [51].

As can be seen from the figures, the relationship between Stokes power and pump wavelength is a function with multiple peaks, which get narrower and more spaced with reduced cavity length, corresponding to wavelengths at which double resonance occurs.

The index m of a given peak is not known a priori, but it can be determined as a function of the location of the chosen peak λ_L^m, the adjacent one to the right (greater wavelength) λ_L^{m-1} and from (3.1):

$$\lambda_L^{m-1} - \lambda_L^m = \frac{1}{m-1}\frac{2n^2V_a}{c}L - \frac{1}{m}\frac{2n^2V_a}{c} = \left(\frac{1}{m\,(m-1)}\right)\frac{2n^2V_a}{c}L \qquad (3.2)$$

Dividing both sides of (3.2) by λ_L^{m-1}, it becomes:

$$\frac{\lambda_L^{m-1} - \lambda_L^m}{\lambda_L^{m-1}} = \frac{\left(\dfrac{1}{m\,(m-1)}\right)\dfrac{2n^2V_a}{c}L}{\dfrac{1}{m-1}\dfrac{2n^2V_a}{c}L} = \frac{1}{m}$$

From which the formula to obtain the index is simply obtained as:

$$m = \frac{\lambda_L^{m-1}}{\lambda_L^{m-1} - \lambda_L^m}$$

Once the index is known, it is possible to calculate the amount ΔL to remove in order to ensure that the frequency peak at an arbitrary index j is at

a desired wavelength λ_L^j' (where $L' = L - \Delta L$ is he final length of the cavity). This can be done by simply solving (3.1) for L and L' and subtracting them.

$$\Delta L = \frac{c}{2n^2 V_a}\left(j\lambda_L^j - m\lambda_L^m\right) = \frac{c\lambda_L^m}{2n^2 V_a}\left(j\frac{\lambda_L^j}{\lambda_L^m} - m\right)$$

It is to note that in order to apply this technique the original length L of the fiber, which may prove difficult to be measured, does not need to be known in advance. All that is required is to locate the double resonance peaks.

A further conclusion that can be obtained by the analysis above is the relationship between the spacing $\Delta\lambda_{\mathrm{DRC}}^m$ between two adjacent resonance peaks and the length of the fiber.

$$\Delta\lambda_{\mathrm{DRC}}^m = \left(\frac{1}{m} - \frac{1}{m+1}\right)\frac{2n^2 V_a}{c}L = \frac{1}{m\,(m-1)}\frac{2n^2 V_a}{c}L$$

From (3.1) it can be seen that m is inversely proportional to L. Because of this, from the formula above it results that $\Delta\lambda_{\mathrm{DRC}}^m$ is inversely proportional to L as well. This can also be visually verified at a glance in the figures 3.4 on the preceding page: in 3.4a on the facing page the spacing is roughly 4 nm for a cavity length of 8 m, while in figure 3.4b on the preceding page the spacing increases to 20 nm (5 times larger) for a cavity length of 1.5 m (roughly 5 times longer).

3.2.2 Self-Injection Locking

The other requirement for double resonance is that the pump lays in one of the resonant frequency modes of the cavity. This requirement can be sastisfied through the use of a stabilization scheme known as self-injection locking [96]. Generally speaking, injection locking consists in sending the light from a low power laser (known as the master laser) into a high power laser (known as the slave laser) [48, 50, 72]. The result of this power injection is that, when the frequencies of the two sources are close enough, the light from the master laser is amplified inside the slave laser, which is thus forced to emit at that frequency. In self-injection locking, in particular, the master laser is replaced by the light of the slave laser after it has experienced some sort of filtering, and is thus less noisy and has a narrower linewidth.

In the case of BRLs, the self-injection is performed by coupling part of the light from the circulating pump inside the ring, which will be at the resonant frequency, right back into the DFB seed pump. This way, the seed pump will always be forced to emit at the frequency of the pump circulating inside the

cavity, which corresponds to a resonant mode. A scheme of how this method can be implemented in a BRL is shown in figure 3.5 on the following page: compared to the basic BRL design, an additional directional coupler (DC2) must be added, with a coupling constant very close to one (99 % / 1 %). A small component of the pump circulating in the ring, which is at one of these resonant frequencies, is coupled out and is fed into the seed pump source through exit 1 and 2 of an optical circulator (OC in the figure) where it locks the seed pump source to emit at the same frequency.

In addition to satisfying one of the requirements for double resonance, the self-injection locking technique is also known to provide other beneficial effects such as a narrowing of the pump linewidth, provided the power of the light used for the self-injection is sufficiently low [10]. An example taken from [96] is shown in figure 3.6 on the next page.

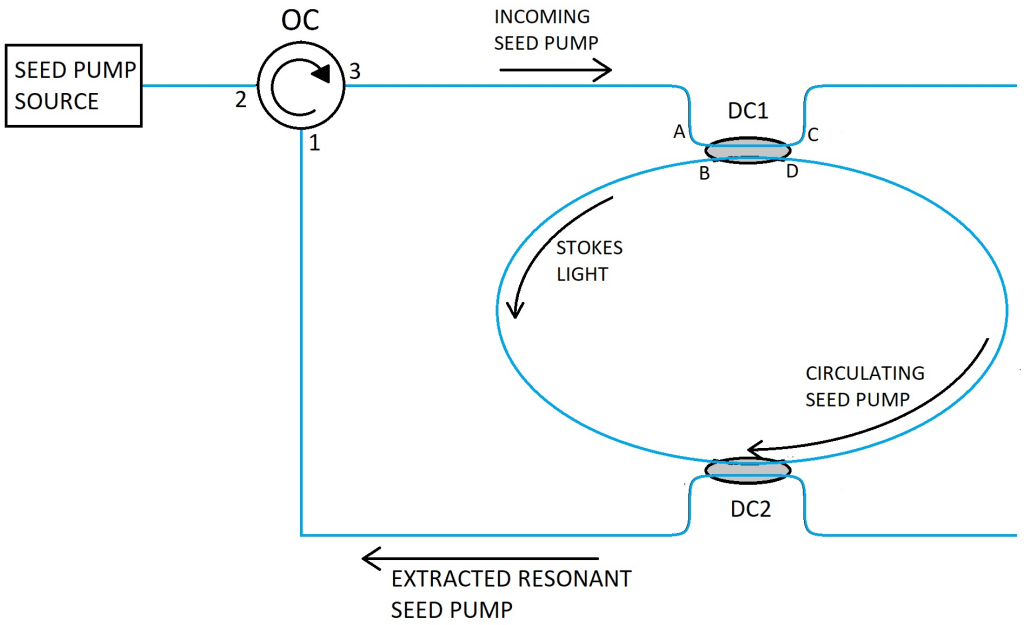

Figure 3.5: Self-injection locking in BRLs.

3.3 Tunability and Stabilization of the frequency shift

As seen in the previous sections, a short cavity and the double resonance effect are expected to lower intensity noise and improve output linewidth while maintaining at least similar threshold power and conversion efficiency. On the other hand, the method used in the previous chapter to tune the Stokes output frequency, that is employing a PZT to change the BFS of the ring

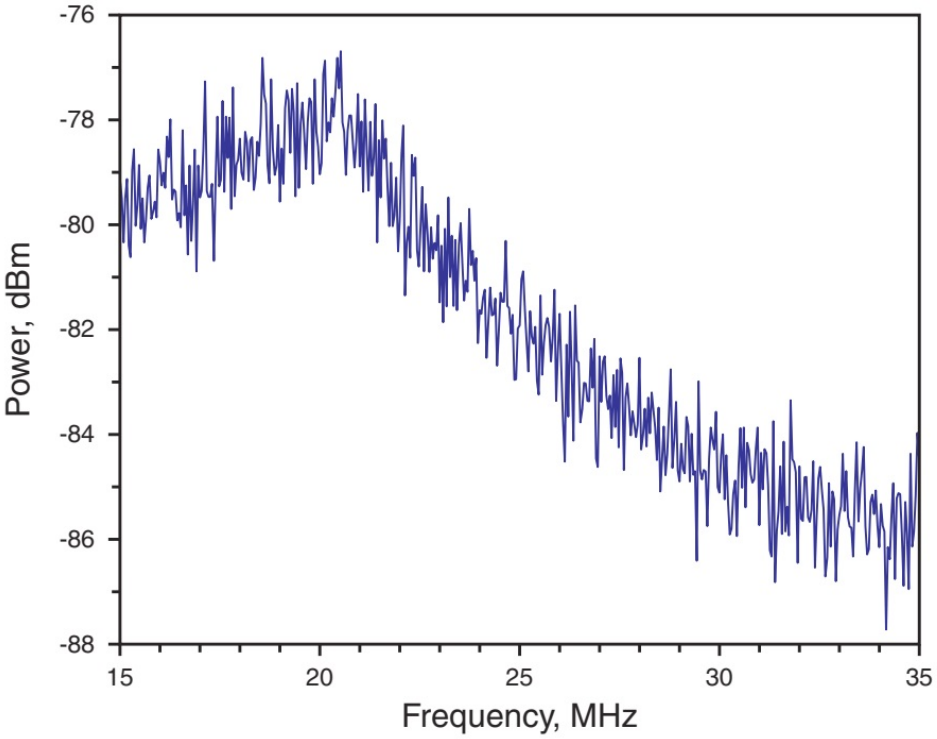

(a) Seed pump spectrum without self-injection locking.

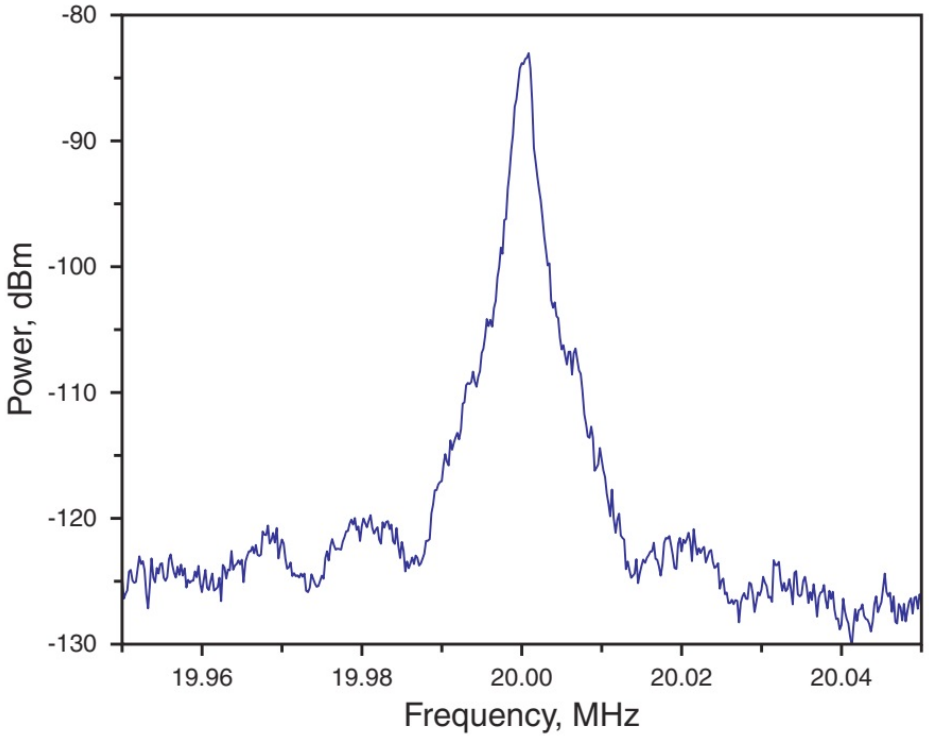

(b) Seed pump spectrum with self-injection locking.

Figure 3.6: Effect of self-injection locking in BRL. From [96].

fiber, can no longer be applied: changing the BFS would mean that it would no longer be necessarily equal to an integer multiple of the cavity FSR, and the double resonance condition would no longer be verified. As a result, for application in BOTDA measurements a different method must be designed to tune the Stokes output frequency, or at least the frequency shift between the Stokes output and the seed pump.

As an additional issue, while thermal instability and vibration no longer cause mode hopping thaks to a reduced cavity length and double resonance, other effects can contribute to change the final pump-probe frequency shift [69]. Such effects include the Kerr effect [42], which is caused by light changing the refractive index of the fiber core inside the ring, and mode pulling [68].

3.3.1 Wavelength locking system

To provide tuning for the pump-probe frequency shift, as well as counteract its detuning, a wavelength locking method such as the one shown in figure 3.7 on the facing page can be implemented. This system uses a EOM to modulate the Stokes output so that the exit light is at a fixed and tunable frequency shift with respect to the pump. To do so, the following steps are followed:

- Using two optical couplers (S1 and S2), a small fraction of the seed pump and the Stokes output from the doubly resonant BRL (DRC-BRL) source are extracted and coupled together into a third coupler (S3) where, similar to the self-heterodyne method described in the section above, their beating signal is fed into a fast photodetector, which outputs a RF signal whose frequency Δf_{BRL} is equal to the frequency difference between the pump and the Stokes output: $\Delta f_{\mathrm{BRL}} = f_{\mathrm{PUMP}} - f_{\mathrm{BRL}}$.

- This signal is sent into a frequency mixer, where it is superimposed with the output of a tunable local microwave signal generator, which emits a signal at a chosen frequency f_{LO}, which must always be greater than Δf_{BRL}. The resulting signal is composed of two sidebands at frequencies $(f_{\mathrm{LO}} \pm \Delta f_{\mathrm{BRL}})$.

- Through the use of a low-pass filter, the band at frequency $f_{\mathrm{LO}} + \Delta f_{\mathrm{BRL}}$ is removed, while the remaining band at frequency $f_{\mathrm{LO}} - \Delta f_{\mathrm{BRL}}$ is amplified and used to drive a EOM that modulates the Stokes output from the DRC-BRL, and is suitably biased to provide carrier suppression ($> 20\,\mathrm{dB}$).

- From the original frequency f_{BRL}, the output of the DRC-BRL is modulated into two sidebands: an upper one at frequency $f_{\mathrm{USB}} = f_{\mathrm{BRL}} + f_{\mathrm{LO}} - \Delta f_{\mathrm{BRL}}$ and a lower one at frequency $f_{\mathrm{LSB}} = f_{\mathrm{BRL}} - f_{\mathrm{LO}} + \Delta f_{\mathrm{BRL}}$, which, remembering the definition of Δf_{BRL}, is equal to $f_{\mathrm{BRL}} - f_{\mathrm{LO}} + f_{\mathrm{PUMP}} - f_{\mathrm{BRL}}$ which is ultimately equal to $f_{\mathrm{PUMP}} - f_{\mathrm{LO}}$. In other words, the lower sideband is downshifted from the pump signal by an amount exactly equal to the frequency set in the microwave generator.

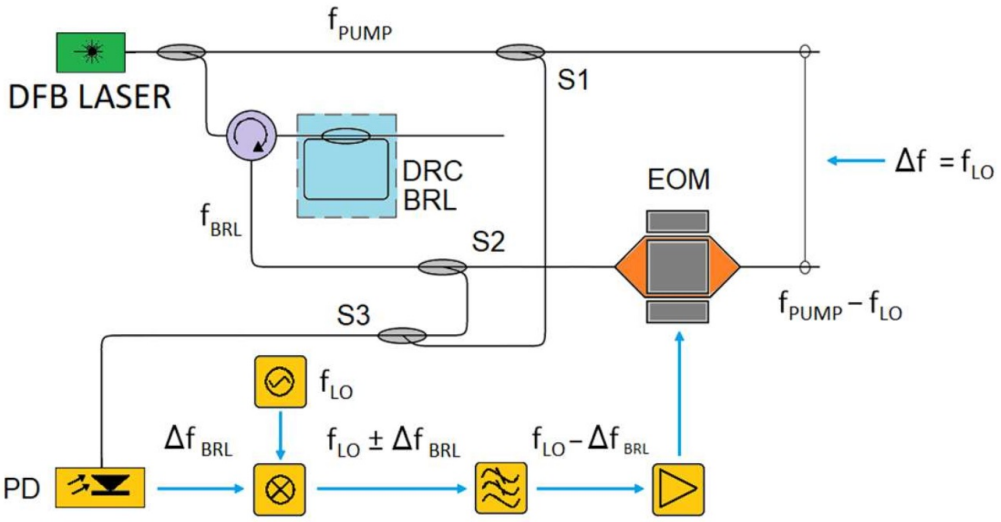

Figure 3.7: Wavelength-locking system scheme. From [82].

If there is any effect that causes the DRC-BRL frequency to shift from f_{BRL} to $f_{\mathrm{BRL}} + \delta f$, the detuning with the pump frequency will change from Δf_{BRL} to $f_{\mathrm{BRL}} - \delta f$. As a result, the frequency modulating the EOM changes from $f_{\mathrm{LO}} - \Delta f_{\mathrm{BRL}}$ to $f_{\mathrm{LO}} - \Delta f_{\mathrm{BRL}} + \delta f$. After the DRC-BRL light is modulated, the frequency of the lower sideband will be

$$f_{\mathrm{LSB}} = f_{\mathrm{BRL}} + \delta f - f_{\mathrm{LO}} + \Delta f_{\mathrm{BRL}} - \delta f\,.$$

It can be immediately seen that the δf components cancel each other out and, as a result, the lower sideband frequency remains equal to $f_{\mathrm{LSB}} = f_{\mathrm{PUMP}} - f_{\mathrm{LO}}$.

In other words, frequency stabilization is maintained because every change in the frequency shift between the DRC-BRL and the pump translates to an opposite change in the final output which cancels the perturbation out.

A few things have to be noted about this setup. First, since the Stokes output must always be lower than the frequency which will be used to locate

the pump-probe frequency shift, it must be made sure that the BFS of the fiber composing the DRC-BRL is lower than the one that the sensing fiber can reach. In addition, in order for the setup to work, it must be ensured that the frequency of the upper sideband $f_{\mathrm{USB}} - f_{\mathrm{BRL}} + f_{\mathrm{LO}} - \Delta f_{\mathrm{BRL}}$ will always be outside of the BGS of the sensing fiber. The frequency difference between the two sidebands can also be written as:

$$f_{\mathrm{USB}} - f_{\mathrm{LSB}} = f_{\mathrm{BRL}} + f_{\mathrm{LO}} - \Delta f_{\mathrm{BRL}} - f_{\mathrm{PUMP}} + f_{\mathrm{LO}} = 2\,(f_{\mathrm{LO}} - \Delta f_{\mathrm{BRL}})$$

From this, it can be seen that a sufficient frequency separation (around 2 GHz) can be obtained if the BFS of the Stokes output (which is equal to Δf_{BRL}) is 1 GHz lower than the minimum value f_{LO} will take. Assuming a standard telecom fiber is employed for sensing, this means that the minumum f_{LO} used will be at the least 10 GHz, thus the fiber used to construct the DRC-BRL should have a BFS equal to around 9 GHz.

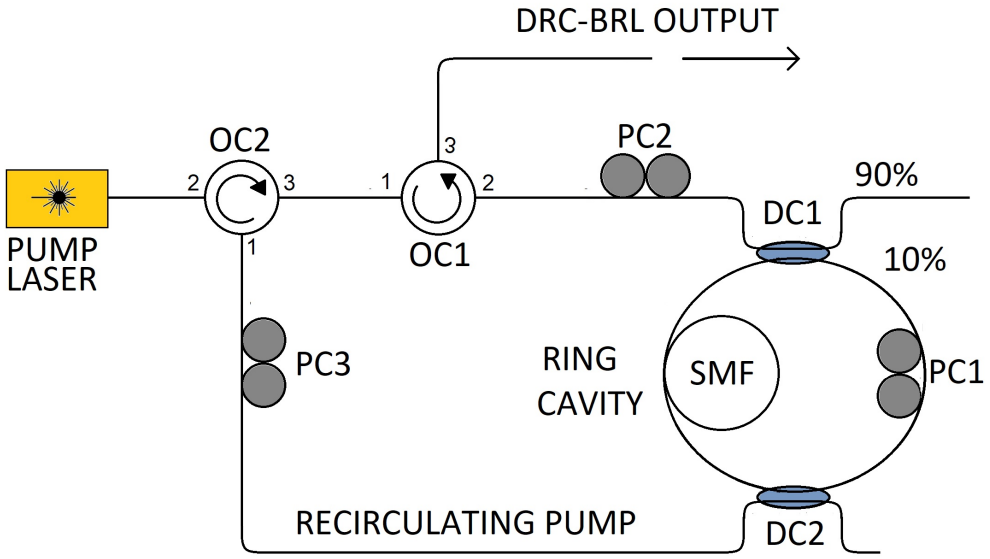

Figure 3.8: Scheme of the DRC-BRL with self-injection locking.

This can be done by employing an optical fiber with a different Germanium (Ge) doping. Standard telecom fibers have a Ge weight percentage of around $3\,\%_{\mathrm{weight}}$, and it is known that an increase of Germanium concentration lowers the acoustic velocity V_a of the core and, recalling (3.1), it can be seen the result of this is a reduction in the BFS [70]. By increasing Ge concentration up to above $20\,\%_{\mathrm{weight}}$ which is done for specialty fibres designed for low bending losses, a BFS of 9 GHz (down from the ~ 10.86 GHz of standard fibers) can be achieved.

Second, while this system requires the use of an EOM (which was removed in the source showcased in the previous chapter), by choosing the right Δf_{BRL} value the signals used to drive it (which have a frequency equal to $f_{\mathrm{LO}} - \Delta f_{\mathrm{BRL}}$) can be kept within a frequency limit of around 1 GHz. As a result, the bandwidth required for the EOM in this system can be made to be around 1 GHz, while traditional systems, such as the optical sideband, require EOMs with bandwidth of more than 10 GHz, and the greatly relaxed hardware requirement results in a cost reduction [61].

3.4 Implementation of the wavelength stabilized DRC-BRL

Using the designs and technique explained above, a DRC-BRL cavity was implemented by the author in [82] and its output performances were evaluated.

3.4.1 Realisation of the short cavity

The layout of the DRC-BRL implementation is shown in figure 3.8 on the preceding page.

The seed pump is provided by a DFB laser with $\lambda = 1553.26\,nm$ and a 350 kHz wide linewidth. The light goes into the fiber ring through exits 2 and 3 of optical coupler OC2 and exits 1 and 2 of optical coupler OC1. The ring cavity consists of a single mode fiber closed by two different couplers: a 90 % / 10 % one (DC1) and a 99 % / 1 % one (DC2). After the circulators, the light enters the ring through DC1. Once the pump circulating inside the cavity exceeds the threshold, SBS is triggered and the counter-propagating downshifted Stokes light is generated. If the ring is doubly resonant, its power increases through multiple loop propagation inside the ring, further increasing intensity and narrowing its linewidth. At every round trip, part of the Stokes output is extracted through coupler C1 and then extracted through exits 2 and 3 of OC1 to be employed in the relevant application.

Coupler DC2 is used to extract a small amount of the pump circulating inside the ring laser, whose frequency will be resonant with the ring, and inject it into the DFB laser for self injection locking through exit 1 and 2 of OC2. Two polarization controllers, PC1 and PC2, are inserted inside and right before the ring respectively. Their purpose is to align the polarizations of the pump and Stokes light inside the cavity, which maximizes the SBS effect [60].

An additional polarization controller, PC3, is instead used in the self-injection

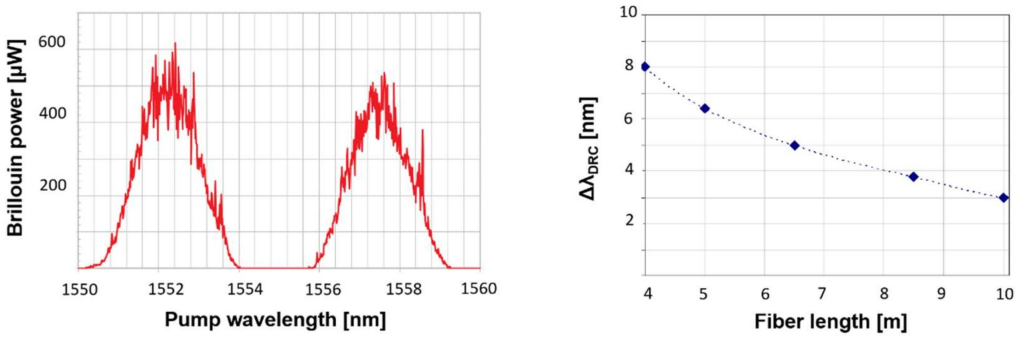

(a) Double resonance peaks in a 5 m long DRC-BRL.

(b) Double resonance peak spacing as a function of cavity length.

Figure 3.9: Double resonance in a BRL cavity. From [82].

locking branch to ensure that the light injected matches the polarization of the DFB output in order to maximize the efficiency of the process.

3.4.2 Achieving double resonance

To ensure that the BRL was doubly resonant with the wavelength of the DFB, the procedure previously described in 3.2 on page 48 was employed, involving the removal of a specific length of fiber. A tunable laser was used to measure the output BRL intensity as a function of seed pump wavelength in the range between 1550 and 1560 nm. Before performing the single cut technique, the length was progressively reduced from 10 m down to 4 m and this measurement was performed for each length in order to evaluate the conclusion that was found regarding the relationship between double resonance peak spacing and cavity length. An example of the measurement of the Stokes output as a function of pump wavlength for a cavity length of approximately 5 m is shown in figure 3.9a. The double resonance peaks spacing at different lengths is shown in figure 3.9b. The relation of inverse proportionality was verified by performing a least squares fit on the data using a power curve model ($y = ax^d$). The resulting best fit exponent was $d = -1.032$, which was close to the expected -1 value for inverse proportionality relation, and the R^2 value was close to 1 (0.9966) indicating that the fit overlapped well with the data and further confirming the expected relation.

After this measurement, the single cut technique was applied, and the final length was about 3.4 m. The DRC-BRL cavity was evaluated similarly to the LC-BRL showcased in the previous chapter in terms of threshold power and maximum output. The results were a threshold pump power of 10 mW

and a maximum output power of 1.5 mW for a pump power of 25 mW. For comparison, the results for the LC-BRL shown in the previous chapter were a threshold power of 2 mW and a maximum output power of 0.5 mW for a pump power of 17 mW.

In terms of threshold power, the LC-BRL shows better results, with a threshold power which is 5 times lower. This is to be expected, since the LC-BRL had a much higher amount of gain medium and a built-in B-EDFA to amplify both the pump and Stokes light, which is not needed in the short cavity.

In terms of conversion efficiency, on the other hand, the DRC-BRL performs significantly better, with a maximum output power that was 3 times higher than the one found for the LC-BRL. The reason for this difference is that the length of the cavity greatly increases the attenuation of the pump and Stokes light, which meant that the Stokes light didn't increase much each roundtrip, and the pump power didn't increase at all. In the short cavity, on the other hand, the low losses, mixed with the resonance for both pump and probe allow both lights to increase progressively inside the cavity, increasing the maximum potential power. In addition, the LC-BRL Stokes output power stopped growing at a lower pump power: since the round trip losses also increase with power, the relation between Stokes output and pump powers suffers from increased diminishing returns, and is mostly dominated by the B-EDFA, which amplified the light by a flat amount.

As a final conclusion, the DRC-BRL compared to the LC-BRL has improved output power and a threshold power which, while lower, is still viable for BOTDA applications.

3.4.3 Wavelength narrowing

The frequency narrowing effect which is expected to be associated with the short cavity DRC-BRL was also evaluated by measuring the linewidth of its output with the self-heterodyne method, using a similar scheme to the one shown in the previous chapter. The long branch was composed of a 12 km long fiber delay line, while the short branch had a 150 MHz acousto-optic modulator. The beating light was measured by a fast photodetector (bandwidth of 12 GHz) and its signal analyzed by an ESA. Referring to [21], it can be seen that the difference in optical path between the two branches allowed measurement of spectral linewidths down to ~ 6 kHz.

The result of one of these measurements is shown in figure 3.10. In this

situation, the Stokes output power was 0.75 mW, the seed pump power was 18 mW and the power of the beating signal was $\sim 200\,\mu$W. For these conditions, the linewidth was found to be ~ 10 kHz, showing a significant narrowing effect compared to the linewidth of the original DFB source, which was 350 kHz. No additional peaks were observed outside of the of the frequency values displayed in figure 3.10, where the signal was below the sensitivity of the measurement, which was limited to about -80 dBm due to SNR limitations, and always at least 20 dB lower than the peak value. In order to evaluate the reliability of this result, similar spectral linewidth measurements were performed with different seed pump power resulting in Stokes output values ranging from 0.5 to 1.2 mW, and similar spectral linewidth values were observed.

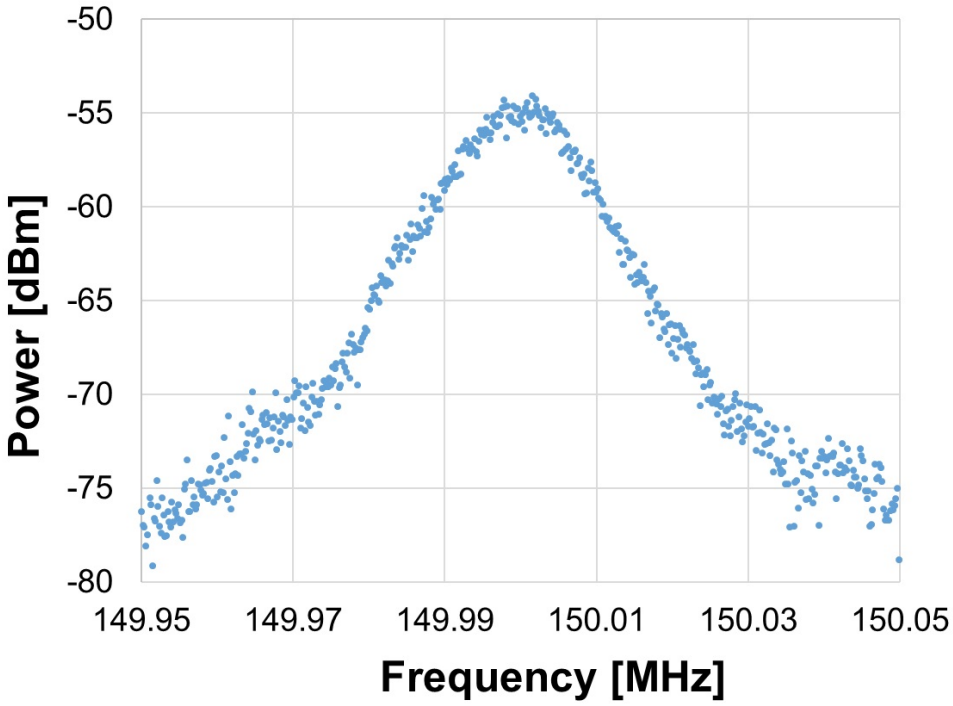

Figure 3.10: DRC-BRL linewidth from self-heterodyne technique. From [82].

Compared to the LC-BRL, where the linewidth was twice the one of the DFB pump, the narrowing effect is greatly increased: the DRC-BRL has an output which is 35 times narrower than the seed pump signal. This difference can be explained by the combined effect of the reduced cavity length, which reduces mode hopping due to acoustic effects, and the resonant behavior of the ring [20]. When the FSR is comparable to the BGS bandwidth, it can be seen that the expected spectral linewidth of the Stokes output can be calculated as

$$\Delta\nu_S = \frac{\Delta\nu_P}{1 + \frac{\pi\Delta\nu_B}{\Gamma}}$$

where $\Delta\nu_P$ is the linewidth of the seed pump, $\Delta\nu_B$ is the BGS linewidth and Γ is a parameter defined by the cavity length L and the coupling ratio R of the cavity (that is, the percentage of power sent into the cavity) and is defined as: $\Gamma = c\,/\,nL \ln R$. Applying the experimental values relevant for the constant of the DRC-BRL cavity, the expected Stokes linewidth was found to be approximately 5 kHz compared to the measured value of 10 kHz. While the calculated result is not equal to the measured one, which can be caused by a variety of issues (including additional losses in the fiber or other minor sources of linewidth broadening), the two results are close enough to show that the measured values are realistic.

3.4.4 Frequency shift stabilization

The stability of the pump probe frequency shift provided by the DRC-BRL linked with the wavelength locking system was evaluated by coupling the output of the DFB pump and the wavelength-locking system (that is, the lower sideband) into the same fiber tract, measuring the beating signal with a fast 12 GHz bandwidth photodetector and analyzing the output with an ESA. The spectrum of the resulting signal is a peak which is centered in the value equal to the frequency shift, which is expected to be equal to the chosen local oscillator frequency f_{LO}, and a linewidth which depends on the frequency drift in a specific averaging time.

An example of the results is shown in figure 3.11 on the following page, for a f_{LO} value of 10.86 GHz and averaging times of 10 ms (figure 3.11a on the next page), which corresponds to the timescale of a single BOTDA measurement, and an extended period of 120 s (figure 3.11b on the following page) [57, 58]. What can be seen from these results is that the peaks are within 1 kHz of f_{LO} (located at the center of the quadrants), showing a tunability with sub-kHz accuracy. For what concerns the stabilization of the frequency shift, the linewidth of the two peaks was 200 Hz for an averaging time of 10 ms and 400 Hz for an averaging time of 120 s.

The measurement was repeated with different f_{LO} values, spanning the entire range of the local oscillators ($10.7 - 11.5$ GHz), showing that the stabilized pump-probe frequency shift is perfectly viable for BOTDA sensing, being accurately tunable and extremely stable both in the single measurement timescale and for even longer timescales.

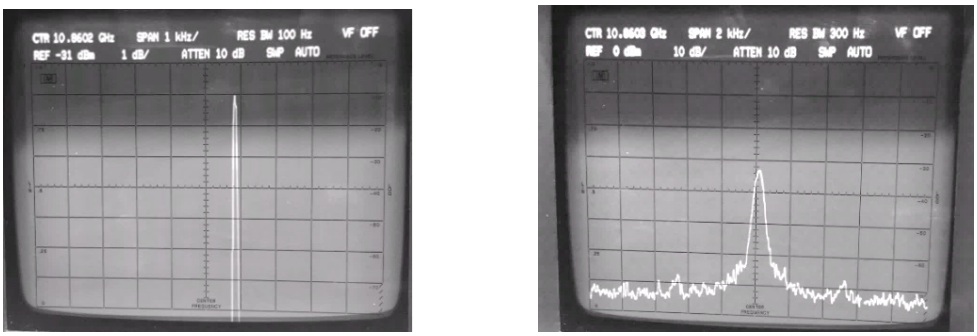

(a) **(b)**

Figure 3.11: Electrical spectrum of the pump-probe beating for wavelength locked DRC-BRL for averaging times of 10 ms (a) and 120 s (b). The frequency range is centered at the local oscillator frequencies f_{LO} 10.8602 GHz and 10.8608 respectively. The y axis scale is 1 dB /division (a) and 10 dB /division (b), while the x axis scale is 1 kHz /division (left) and 2 kHz /division (right). From [83].

3.4.5 Intensity noise measurement

To evaluate the combined effects of employing a short cavity on intensity noise and wavelength locking, the RIN of the Stokes output was measured and compared with the RIN profiles of the DFB source and the LC-BRL one obtained in the previous chapter. The results are shown in figure 3.12 on the next page.

What can be seen from the main figure is that the RIN increase at frequencies below 500 MHz which was seen in the LC-BRL source is greatly suppressed in the DRC-BRL, which shows RIN values only slightly above the original pump DFB levels, between -140 dB / Hz and -150 dB / Hz across the whole $1 - 800$ MHz range, except in the first few MHz frequencies. Since ESA measurements at those small frequency ranges are unreliable, a different approach was used to estimate the RIN spectrum at lower frequencies: the wavelength locked output was fed into an oscilloscope and its spectrum was extracted through a fast Fourier transform (FFT). The RIN profile in this frequency range, which is shown in the inset of figure 3.12 on the facing page indicates that in the range up to 50 kHz (limited by the sampling rate of the oscilloscope) never exceeded -100 dB/Hz, showing limited RIN values even at very low frequencies.

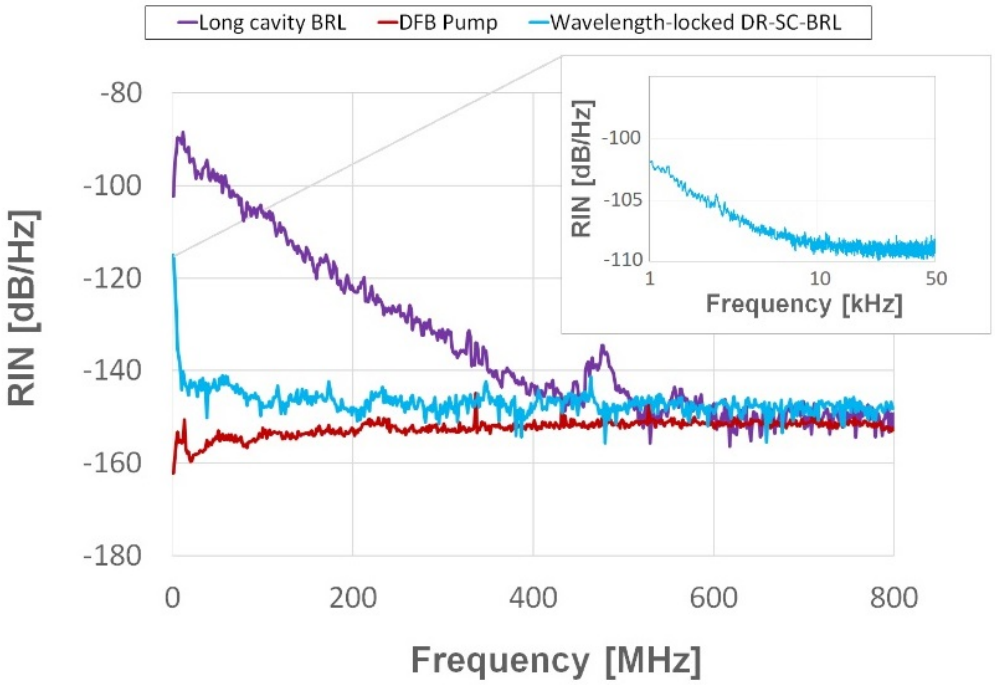

Figure 3.12: Measured spectral RIN the LC-BRL, the λ-locked DRC-BRL and the DFB pump. Inset: RIN measurement for DRC-BRL in the $1 - 50$ kHz frequency range. From [83].

3.4.6 Predicted resolution improvement

While it hasn't yet been possible to employ the cavity in a BOTDA demonstration, by comparing the intensity noise profiles of the Stokes ouptuts for the stabilized DRC-BRL and the LC-BRL it is possible to make a prediction of the effect the lowered noise profile would have on frequency, temperature and strain resolution by calculating the SNR of the probe provided by the two sources.

In BOTDA measurements, the final SNR of the detected probe signal is determined by the combined effect of the current generated by the photodetector I_S and the contribution of different noise variances: the thermal noise δ^2_{th} and shot noise δ^2_{sh} from the photodetector, the spontaneous-spontaeous δ^2_{sp-sp} and signal-spontaneous noise δ^2_{sp-s} from the EDFA, and the intensity noise δ^2_{RIN}. The nature of this relationship is the formula [94]:

$$\mathrm{SNR} = \frac{I_S}{\delta} = \frac{I_S}{\sqrt{\delta^2_{th} + \delta^2_{sh} + \delta^2_{sp-sp} + \delta^2_{sp-s} + \delta^2_{\mathrm{RIN}}}}$$

When the probe is generated by low-RIN sources, the dominant term

in the formula above is the spontaneous signal beat noise δ^2_{sp-s}. When the signal is generated by a fiber ring laser, such as the cases described here, the dominant term is the intensity noise δ^2_{RIN}. In this case, the SNR can be calculated by integrating and then inverting the RIN profile of the source over a frequency range equal to the bandwidth of the photodetectors used to acquire the BOTDA trace (125 MHz), which resulted in SNR values of ~ 38.7 dB for the LC-BRL and ~ 61 dB for the wavelength locked DRC-BRL.

In BOTDA measurement, when the BFS is acquired by Lorentzian curve fitting, the BFS resolution is related with the trace SNR alongside the BGS linewidth $\Delta\nu_B$ of the sensing fiber by the formula [37]:

$$\delta\nu_B = \frac{\Delta\nu_B}{\sqrt{2}\,(\mathrm{SNR})^{1/4}} \tag{3.3}$$

The temperature and strain resolution $\delta\nu$ and δT are linked to the BFS resolution by a relation of direct proportionality:

$$\delta T = \frac{\delta\nu_B}{C_T\nu_B\,(t_r)} \quad \text{and} \quad \delta T = \frac{\delta\nu_B}{C_S\nu_B\,(0)}$$

in which C_T and C_S are the BFS linear coefficients for temperature and strain, while $\nu_B\,(t_r)$ and $\nu_B\,(0)$ are the BFS values when the sensing fiber is respectively at reference temperature and unstrained [40].

The short-cavity double-resonance wavelength-locked BRL allows a $\mathrm{SNR}_{\mathrm{RIN}}$ improvement of ~ 22.3 dB, which, as of (3.3), translates to a FBS resolution which is reduced by a factor of ~ 5.5 dB, which is equivalent to a factor of 3.5. Since the resolution values of the previous chapter were 0.5 MHz for the frequency, 0.5 °C for the temperature and 10 $\mu\epsilon$ for the strain, the values with the new DRC-BRL source would be ~ 0.14 MHz, ~ 0.14 °C and 2.9 $\mu\epsilon$.

It is to note that, as said before, this evaluation assumes that the dominant noise element in the DRC-BRL source is still the intensity noise. While the intensity noise suppression might be so strong to make this no longer the case, it is till useful to show the extent of the improvement in wavelength-locked DRC BRL.

It must also be noted that this evaluation does not take into account the beneficial effect the greatly reduced linewidth of both the BRL output and the seed pump would have on the resolution of BOTDA measurements.

In conclusion, in this chapter the development of a DRC BRL design was evaluated, which made use of both a short cavity to reduce intensity and frequency noise effects and double resonance to maintain good threshold power and conversion efficiency, including a self-injection locking system and

a wavelength stabilization scheme to provide both tunability and control of the frequency shift between the Stokes output and the pump.

The new source showed strong linewidth narrowing behavior and a low intensity noise profile despite being based on a Brillouin ring laser. At the same time, the wavelength locking system provided exceptional accuracy and stabilization for the frequency shift, both in the 10 ms timescale and in the 120 s one, without any potential hysteresis effect or instability due to mechanical elements.

While this system is more complex than the one shown in the previous chapter and employs an EOM like the OSB method, it still reduces costs due to its much lower requirements in terms of EOM bandwidth, while also providing a linewidth narrowing effect thanks to the BRL cavity that none of the other schemes mentioned here can provide.

The contribution of the author to the work presented in this chapter consists of the theoretical modeling and characterization of the short cavity BRLs, including their doubly resonant behavior, intensity noise suppression, and linewidth narrowing. In addition, it includes the characterization of the tuning and stabilizing capabilities of the wavelength-locking system.

4

Dynamic BOTDA measurement: Slope-detection and Closed Circuit BOTDA

As mentioned in previous chapters, while BOTDA systems have seen wide employment for long range distributed sensing, they also have a series of limitations further than complexity and cost. For instance, the pump pulse duration must be 10 ns at minimum, due to the time needed for the acoustic field to be excited by the pump and probe, which puts a limit of ~ 1 m on the minimum spatial resolution obtainable. Another inherent limit for BOTDA sensing is the time required to perform a single measurement. In order to obtain high resolution, high range temperature and strain measurements, the BGS must be characterized over a range of 100–200 MHz of frequency, with a resolution of 1 or even 0.1 MHz. As a result, in order to obtain a single BFS distribution $\nu_B(z)$ across the sensing fiber, thousands of single measurements have to be taken. Considering that every measurement usually requires the probe trace to be averaged tens if not hundreds of times, and that every single trace requires 10 μs per km, it can be seen that a single temperature/strain profile requires several minutes to be extracted, thus relegating BOTDA sensors to the measurement of temperature/strain distributions that are either purely static or change in a larger timescale.

To overcome this limit and allow for dynamic BOTDA measurements, a variety of approaches have been explored in recent years. In [78], for instance, a method defined as Fast-BOTDA (F-BOTDA) was proposed, which involved pre-loading all the possible probe outputs in a single arbitrary waveform. In [102], a correlation technique allowed dynamic strain and temperature sensing with a frequency of 200 Hz (equivalent to a measurement time of 5 ms) with a 10 cm spatial resolution and 20 m measurement range.

Despite the impressive reductions in measurement time, it was argued in [101] that such methods only allowed for a limited range of a few hundred sensing points, one order of magnitude lower than most modern applications.

In [28, 110] other methods were proposed utilizing Optical Frequency Division Multiplexing (OFDM), which allowed ultrafast BOTDA measurement at the cost of a reduced spatial resolution.

4.1 Slope-Assisted BOTDA

Among the fast BOTDA methods, one of the most known and with less drawbacks is the slope-assisted BOTDA (SA-BOTDA). The main idea behing this approach is to keep the pump-probe frequency shift always at a certain setpoint, which resides within the rising or falling slope of the sensing fiber's BGS at a rest state, where the shape of the Lorentzian curve can be equated to a linear slope. At every point of the fiber, the Brillouin amplification will be dependant on the shift of the BGS due to temperature and strain variation, as shown in figure 4.1 on the next page: if the chosen slope is rising, an increase in Brillouin amplification in a point in the fiber will correspond to a decrease in local BGS compared to the base value, denoting a decreased temperature or strain, and viceversa a decrease in amplification will correspond to an increase in the local BGS compared to the base value and an increased temperature or strain. If the chosen slope is descending, these relationships are reversed, as shown in figure 4.2 on the facing page: an increase or decrease in Brillouin amplification corresponds to increased or decreased temperature/strain values, respectively.

In addition, if the change in BFS is less than the width of the linear region of the BGS, the changes in Brillouin gain will be linearly related to the shifts in the BGS.

As a result, once the slope of the BGS is known, it is possible to directly translate the intensity of a single amplified probe trace into a map for the BFS across the fiber.

In principle, the optimal frequency setpoint in terms of BFS uncertainty (and thus temperature/strain sensitivity) should be located at the point where the slope η of the BGS reaches its maximum. The Brillouin Gain Spectrum can be defined in first approximation as a Lorentzian function:

$$g\left(\Delta\nu\right) = \frac{g_B \Delta\nu_B^2}{\Delta\nu_B^2 + 4\Delta\nu^2}$$

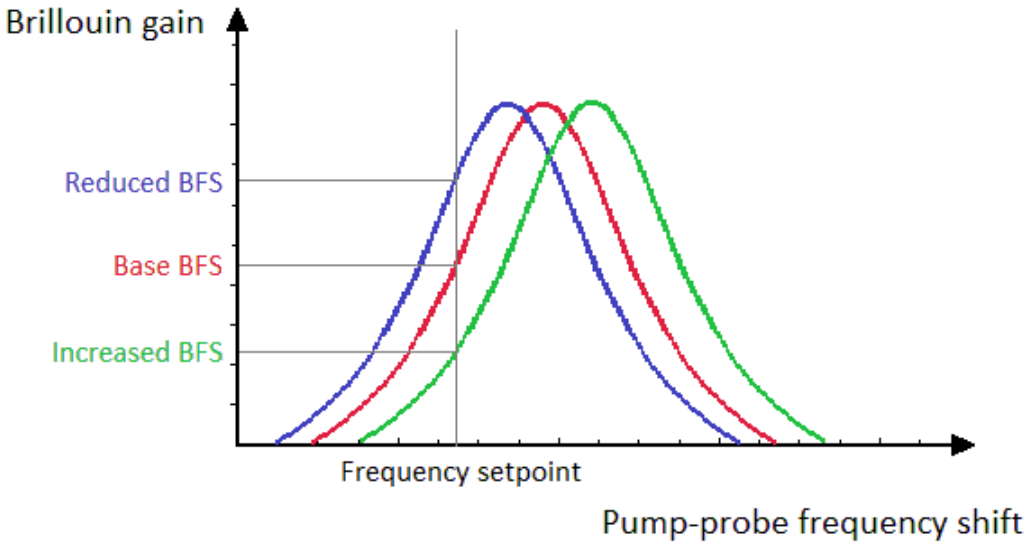

Figure 4.1: Brillouin gain-BFS conversion in Slope-Assisted BOTDA when the frequency setpoint is on the rising edge of the BGS.

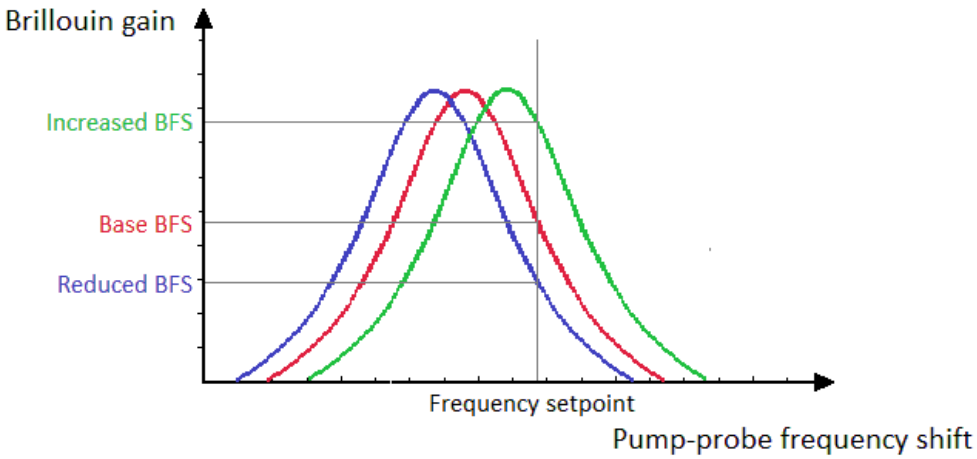

Figure 4.2: Brillouin gain-BFS conversion in Slope-Assisted BOTDA when the frequency setpoint is on the falling edge of the BGS.

where $\Delta\nu = \nu_B - \nu_S$ is the detuning between the BFS ν_B and the pump-probe frequency shift ν_S and $\Delta\nu_B$ is the linewidth of the BGS. The $\Delta\nu$ that maximizes the slope is also the one that nullifies the second order derivative of $g(\Delta\nu)$:

$$\frac{d^2g}{d\Delta\nu^2} = \frac{-8g_B\Delta\nu_B^2\left(\Delta\nu_B^2 - 12\Delta\nu^2\right)}{\Delta\nu_B^2 + 4\Delta\nu^2} = 0$$

which, when solved, gives an optimal frequency detuning equal to:

$$\Delta\nu_{\text{op}} = \pm\frac{\Delta\nu_B}{\sqrt{12}}$$

It is to note that this optimal frequency is very close to the BFS, and to a zone of the BGS where the slope quickly goes to 0, and thus in practical applications small temperature/strain fluctuations could move the Brillouin amplification outside of the linear region. Because of this, the detuning value $\Delta\nu_B\,/\,2$ is chosen instead, since it maximizes the range of the linear region in both directions.

The uncertainty of the BFS measurement as a function of the frequency detuning is the product of the fiber slope and the intensity noise σ_B. For the maximum slope point, this is

$$\sigma_\nu^{\text{maxslope}} = \frac{4\Delta\nu_B}{3\sqrt{3}}\frac{\sigma_g}{g_B}$$

It can be shown that the measurement noise for a BOTDA setup that uses N steps withing the FWHM of the BGS which extracts the BFS through a quadratic curve fit is given by [93]:

$$\sigma_\nu^{\text{standard}} = \frac{\sqrt{3}\Delta\nu_B}{2\sqrt{N}}\frac{\sigma_g}{g_B}$$

where N is the number of frequency steps in the BOTDA measurements. By taking the ratio between these two equations, the BFS uncertainty improvement using a standard BOTDA is obtained as:

$$\frac{\sigma_\nu^{\text{maxslope}}}{\sigma_\nu^{\text{standard}}} = \frac{8}{9}\sqrt{N}$$

If the FWHM of the BGS is 60 MHz (which is correct for a spatial resolution of 2 m) and a scanning step of 1 MHz, $N = 60$ and the ratio above is equal to 6.88, which means that to obtain the same BFS uncertainty using a single frequency probe one would obtain using classical BOTDA would require ~ 47 times more averages, showing a greater degree of efficiency since to obtain

the same results the same measurement is performed 47 times instead of 60. When instead the point at the BGS FWHM is chosen, the noise is $2\sqrt{N}\,/\,\sqrt{3}$ times higher, which for $N = 60$ corresponds to a factor of 8.9 times, meaning that in order to obtain the same BFS noise by gain-frequency convertion using only a single probe frequency at $\Delta\nu = \Delta\nu_B\,/\,2$ would require ~ 81 times more averages. While in theory this would mean that at $\Delta\nu = \Delta\nu_B\,/\,2$ this method is always slower, in practical terms BOTDA frequency sweeps are always larger than the FWHM of the BGS and equal to at least 100 MHz to guarantee that a sufficient portion of the BGS is measured even when the BFS shifts, while the SA-BOTDA doesn't need scanning as long as the BFS change is less than the linear region, where the slope is mostly constant. As a result, the main advantage of this method compared to classical BOTDA is that it is possible to greatly increase the measurement speed, since it eliminates the need for frequency scanning, reducing the measurement time to the time required to acquire a single trace multiplied by the number of traces needed for averaging. In practical terms, this can reduce the measurement speed to the order of tens of milliseconds. The main limitation of this technique is that in order to translate changes in Brillouin gain to changes in the BFS the latter must be within the linear region of the BGS: if it isn't, the relation is no longer linear and the translation becomes too difficult. In additon, other zones of the BGS closer to the peak or the tail have a lower slope, which translates to a lower accuracy in the measurement. Finally, due to the symmetrical nature of the BGS, if the changes in BFS are not limited it is in theory not possible to univocally determine them, as is shown in figure 4.3 on the next page.

4.2 Closed-Circuit BOTDA

In [108], a different way to solve the limited range of SA-BOTDA was proposed, named Closed Circuit Brillouin Optical Time Domain Analysis (CC-BOTDA). The idea behind this approach is to use a variable probe frequency to track the BFS changes along the fiber, using a closed loop (feedback) control system to always maintain the pump probe frequency shift at the same point of the Brillouin gain spectrum. Whenever the gain measured at the original probe frequency ν_S changes due to a shift in BFS, a control system, such as a Proportional-Integral-Derivative (PID) controller, extrapolates the probe frequency change $\Delta\nu_{\text{op}}$ required to revert the measured gain back to its original value, and the current BFS value is obtained by adding $\Delta\nu_{\text{op}}$ to the original ν_S. As a result, when tracking is fast enough compared to the dynamics causing

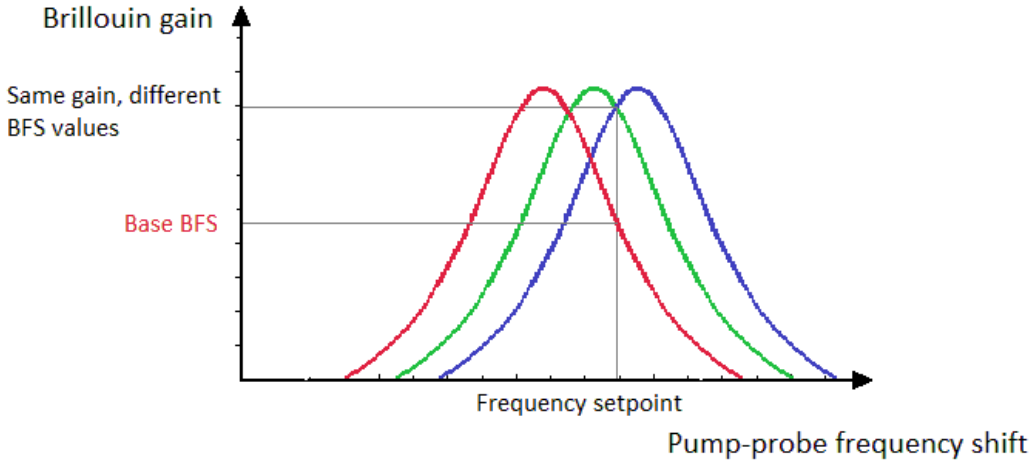

Figure 4.3: Ambiguous SA-BOTDA reading when the BFS is outside of the linear region.

the BFS to change, it is possible to continuously update the pump-probe frequency detuning to follow the shifts in BGS, making it possible to perform Slope-Assisted measurements with a potentially indefinite BFS range, not limited to the linear region of the BGS lateral slope.

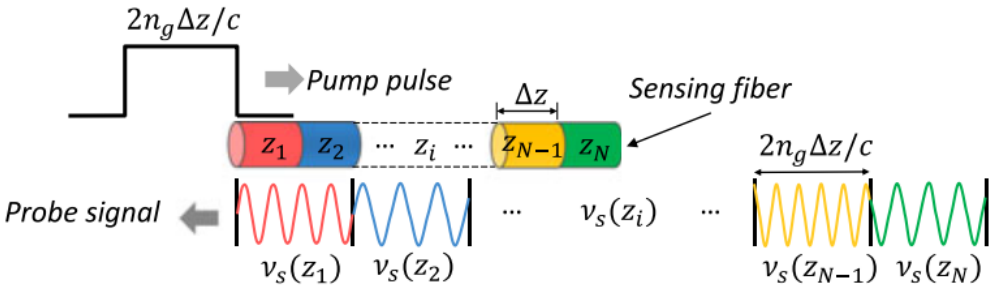

Figure 4.4: Segmentation of the sensing fiber and the probe frequency. From [108].

It is to note that, generally speaking, in real situations every point of the sensing fiber will have a different BFS. Because of this, in order for the CC-BOTDA to work the sensing fiber must be trated as a series of N fiber segments, where $N = L \,/\, \Delta z$, where Δz is the spatial resolution of the sensor and L is the length of the sensing fiber. Through the use of an arbitrary waveform generator (AWG), the probe wave will also be temporally divided in N segments, each with a length equal to the pump pulse (which can

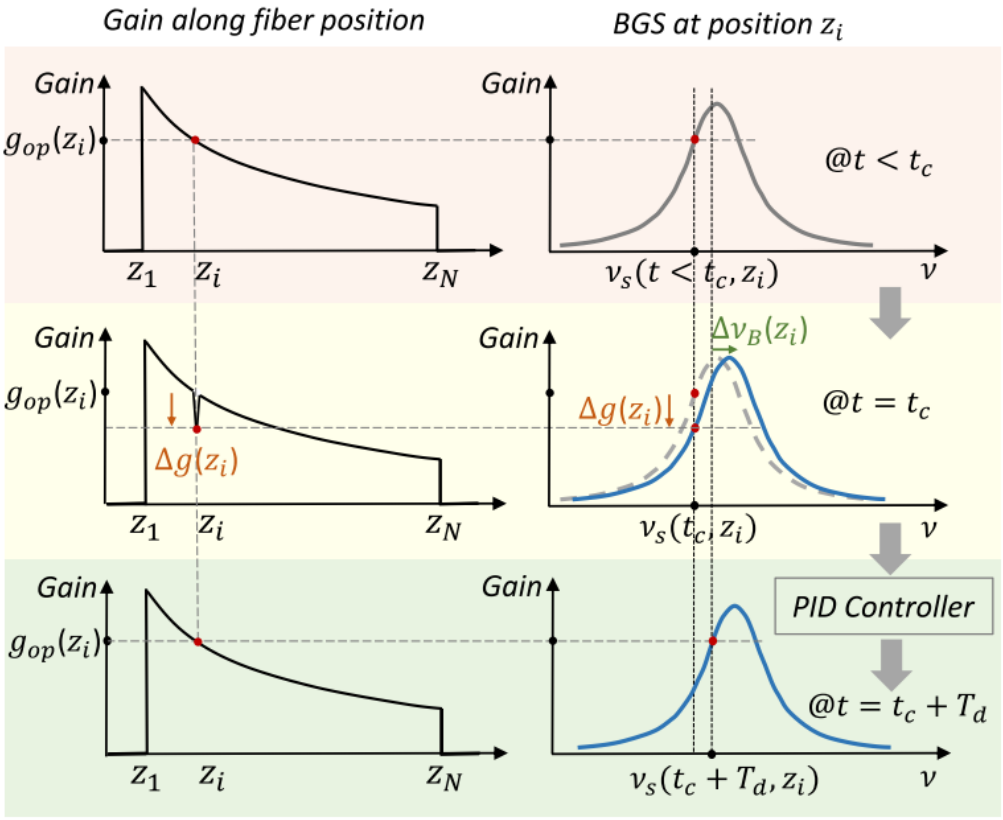

Figure 4.5: CC-BOTDA gain compensation process. From [108].

be expressed as $2n_g\Delta\nu\,/\,c$, where $c\,/\,n_g$ is the group velocity), as shown in figure 4.4 on the facing page. The frequency of each segment is independent from the others.

When the pump pulse reaches a fiber segment at position z_i, it will interact with the corresponding probe segment whose probe frequency will match the expected detuning $\nu_S(z_i)$ thereby giving the measured corresponding gain amplitude $g(z_i)$.

Before the measurement is performed, the initial reference BFS for every segment of the fiber $\nu_S(z)$ is taken using standard BOTDA. Each segment of the probe wave is then set at the chosen detuning $\Delta\nu_{\text{op}}$ from the corresponding measured starting frequency shift. In this situation, the amplified probe trace will take the shape of a uniform exponential decay (as shown in the upper left corner of figure 4.5), corresponding to a uniform Brillouin gain across the fiber. This gain will be chosen as the set gain g_{op}.

During the measurement, whenever an external effect causes the local BGS to shift (as shown in the central frame of figure 4.5), the corresponding local

gain will change from the reference value g_{op} by an amount $\Delta g(z_i)$ which will affect the corresponding point in the measured probe trace.

The closed-loop system of the CC-BOTDA will adjust the local probe frequency $\nu_S(z_i)$ by an amount dependant on $\Delta g(z_i)$. The purpose of the system is to compensate the gain change and bring it back to the original value by continuously adjusting the frequency at each step, until the local pump-probe frequency shift reaches the original detuning from the BGS, as shown in the bottom frame of figure 4.5 on the preceding page.

In this configuration, the information on the evolution of the BFS variation is not obtained by BGS spectral fitting or by direct conversion of the measurement gain, but directly by the control system output.

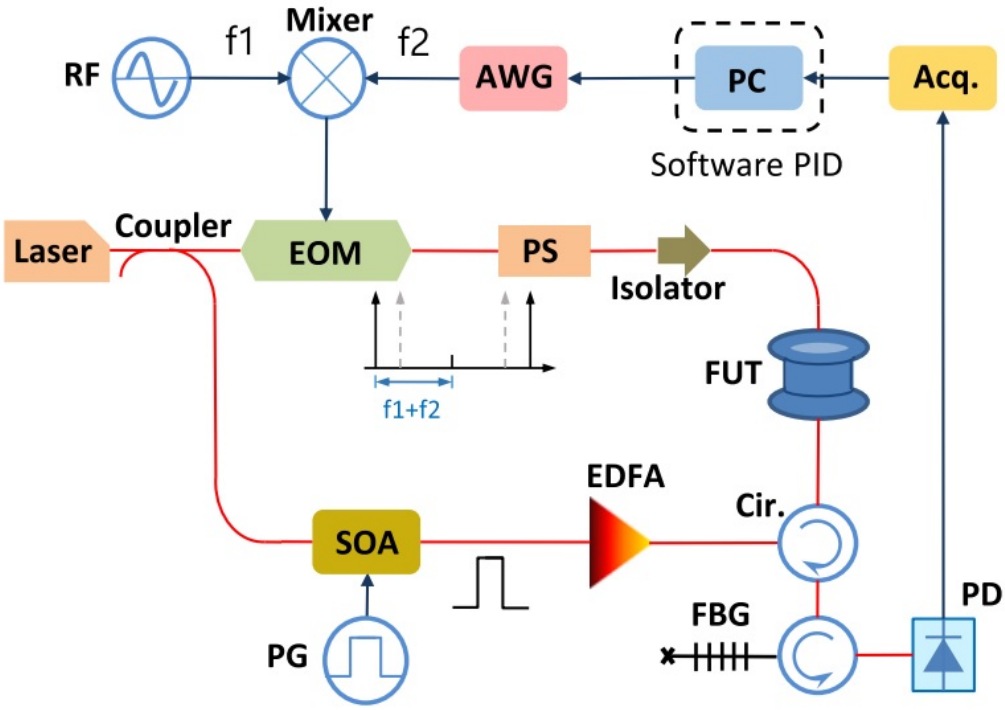

Figure 4.6: Experimental setup. From [108].

In [108], a CC-BOTDA system was implemented using a PID controller as a feedback system. The setup demonstrated to be able to measure temperature variation over a length of 10 km of fiber with a measurement time of 1.7 seconds, which was mainly limited not by the measurements but by the data upload time to the AWG in order to create the segmented waveform.

In addition, among the possible PID configurations, P and PI controllers were found to be the most effective, and it was also shown that, with specific

configurations, they could act as low pass filters as well as feedback loop controllers. Below is a description of some of the results of the work.

4.3 Experimental Implementation

The experimental setup is shown in figure 4.6 on the preceding page. The pump light was shaped into a 20 ns pulse (corresponding to a 2 m spatial resolution) with high (> 50 dB) extinction ratio through a Semiconductor Optical Amplifier (SOA), which will be described in more detail in chapter 6, and shaped into a 20 ns optical pulse with high extinction ratio, and was then amplified with an EDFA. Similarly to a OSB BOTDA scheme, the probe was generated through the use of a EOM, which was driven by a segmented sine wave as described above. As seen previously, a polarization scrambler was used to remove polarization noise. Afterwards, both waves were inserted at both ends of a 9.3 km long sensing fiber, with the amplified probe being detected using a photodetector (PD) and an FBG in a similar way to the one shown in figure 2.11 on page 39.

The segmented probe was generated by driving the EOM with a wave generated by mixing a RF microwave signal at constant frequency $f_1 = 10.2$ GHz with a variable signal at $f_2 = 150$—300 MHz produced by an AWG (whose maximum sampling rate was 2 GHz), so that in all cases the probe component that experienced Brillouin interaction with the pump was at the frequency $f_1 + f_2$. Since the spatial resolution was 2 m and the length of the sensing fiber was 9.3 km, the signal generated by the AWG was composed of 4650 time-domain segments, whose initial frequency was set to match the corresponding initial local BFS (around 10.46 GHz) minus the detuning $\Delta\nu_{\text{op}}$ (which in this case was equal to 17.3 MHz).

At every measurement step, the gain for every segment is acquired and the closed-loop system of the CC-BOTDA calculates the necessary changes to the frequencies, as shown in figure 4.5 on page 73, with the use of a software based PID controller. Although the derivative (D) is known to "predict" system behavior and reduce the overshoots and oscillations imposed by the integral (I) term, it also greatly amplifies the impact of noise. Because of this, only the Proportional (P) and integral component were used.

Due to the time required to upload the updated segmented wave to the AWG, the time between each measurement had a lower limit of 1.7 s.

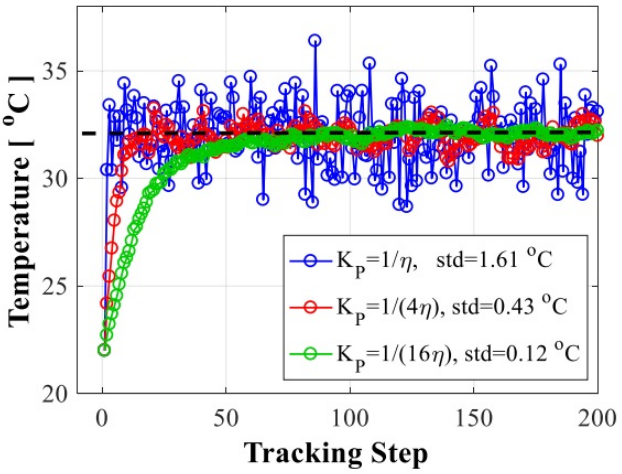

(a) Proportional term only.

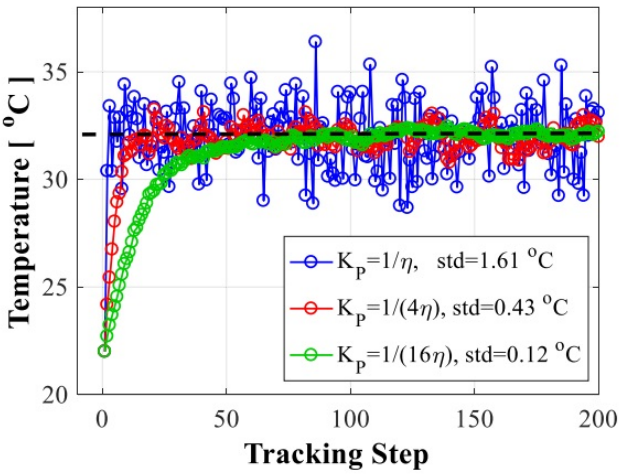

(b) Proportional and integral term.

Figure 4.7: Output of the tracking system for a 10 °C temperature step. From [108].

4.4 Experimental results

The behavior of the PI controller was evaluated by applying a step-like temperature increase on a 6-m long fiber hotspot section at the end of the fiber using different proportional (K_P) and integral (K_I) parameters. Examples of readings from the hotspot are shown in figure 4.7. As can be seen from 4.7a, reducing the K_P coefficient reduced the noisiness of the tracking system output, while also increasing the number of steps required for the system to track the changes: when $K_P = 1/\eta$, the system responded instantly to the changes, but its reading was noisier, while for $K_P = 1/16\eta$ the system required a greater amount of steps to track the temperature change. As was

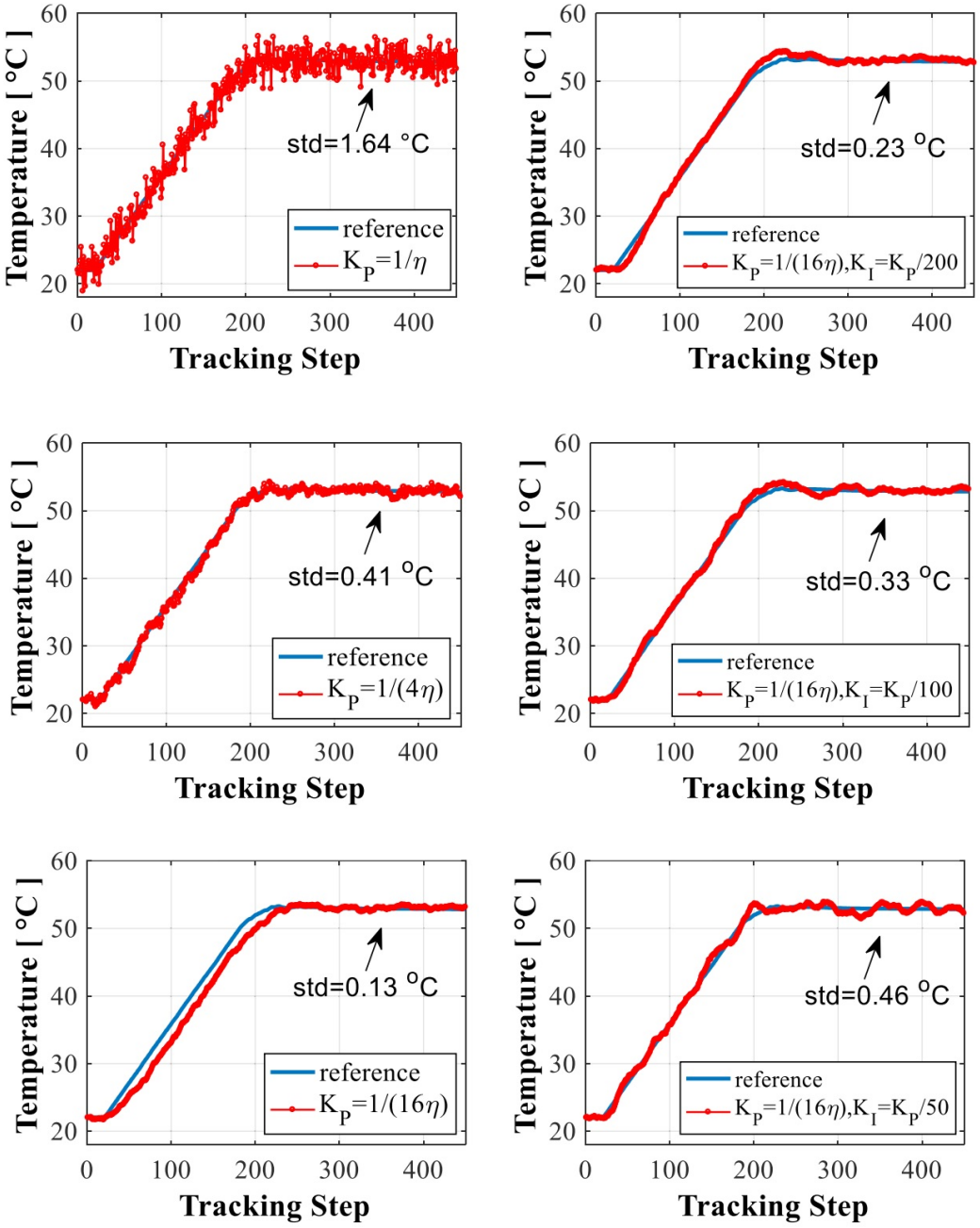

Figure 4.8: Output of the tracking system with different PI parameters for a gradual temperature change of 0.08 °C. From [108].

proven in [108] and will be seen in the next chapter, a tracking system using a P controller with $K_P < 1\eta$ behaves like a low-pass filter. From 4.7b on page 76 it can be seen that by adding a I component to the controller, the system response was faster, but added an overshoot and some noise to the response.

From these result, it was found that the best compromise in terms of noise suppression and response speed was a PI controller with a very small integral component, such as the one with $K_P = 1/16\eta$ and $K_I = K_P/200$.

The tracking behaviour over an extended range was verified by gradually increasing the temperature of the hotspot fiber section from 22 °C to 53 °C with a climbing rate of 0.08 °C/s (or 0.14 °C per step). The results are shown in figure 4.8 on the previous page. As can be seen from the figures, the use of the tracking system allowed the process to be effectively tracked over a range that exceeded SA-BOTDA. In addition, the largest delay found between the actual temperature and the tracking output was equal to 15 steps in the case with $K_P = 1/16\eta$, which with the tracking speed of this device was equal to a time delay between the frequency change and the measurements of only 25 s, while providing similar accuracy. In addition, by adding an integral component, the delay could be removed at the cost of increasing the reading noise.

From these results it can be seen how, despite the limited measurement speed (which could be improved with better hardware), the tracking system shown in this chapter can provide an interesting alternative to both SA-BOTDA and classical BOTDA, thanks to its capability to provide accurate measurements over an extended temperature or strain range, and require only a few seconds to achieve similar results to the ones that would be achieved in minutes with a non dynamic measurement.

5

Controlling and Filtering Methods for Closed Loop BOTDA

5.1 Tracking with P and PI controllers

As has been seen in [108], a simple P controller is capable of keeping the pump-probe frequency shift inside the linear region of the BGS by monitoring and responding to the changes in intensity from the setpoint.

Two things have to be noted about this result. First, while the temperature/strain shift that can be tracked is virtually infinite, depending on the chosen K_P parameter there are some limit situations that can cause the tracking to fail: when K_P=1, any situation where the noise fluctuations are greater than the width of the linear region of the BGS will cause the pump-probe frequency shift to exit it, and the link between the measured intensity and the BFS position estimate will no longer be reliable. For similar reasons, the expected temperature/strain variation for each measurement step cannot exceed the half-width of the linear region.

When a K_P parameter lower than 1 is chosen, the noise suppression noted in [108] and that will be detailed in this chapter will cause the system to be able to tolerate a noise level that is greater than the width of the linear region of the BGS. At the same time, any strain/temperature change with a step-by-step correlation greater than 0 will cause a cumulative delay between the measured intensity and the setpoint which, if large enough, would cause the linear relation between frequency shift and gain to no longer apply, even if every step-by-step change is smaller than the width of the linear region.

As will become evident in chapter 6 on page 105, where tracking was never found to be an issue, and was already seen in [106], these conditions are limit

cases: the SNR is expected to be significantly lower for lengths in the order of kms for noise alone to cause the measurement to exit the BGS linear region, and in order for a single step to do the same the temperature should increase by 30 degrees Celsius in a fraction of a second, which is unlikely in most situations, save for violent thermal phenomena. At the same time, extended temperature variations of tens of degrees Celsius for multiple steps are as unlikely, save for specific application that won't be addressed here.

As a consequence, in this work P and PI controllers are assumed to always be capable of following temperature changes, unless for extremely small K_P and K_I parameters.

As a further note, in most applications that see employment of PID controllers the objective is to maintain the system at a given state (the setpoint) which has an effect on its dynamics [99, 100]. In particular, this means that PID controllers need to be tuned according to the transfer function of the system in order to optimize different aspects of its behavior, such as the speed of the response [66]. For more examples and variations, see [27, 35, 80, 100].

In BOTDA sensing, on the other hand, maintaining the Brillouin gain at every point in the fiber at the specific setpoint has no effect on further evolutions, because these are caused by the system that is being measured, which is unaffected by the state of the sensor. Because of this, the only function of the controller is to keep the pump-probe frequency shift in the linear region of the BGS. In addition, since the sensor can be employed to monitor a wide variety of different situations, no assumption can be made on the extent and nature of temperature/strain fluctuations. Because of these reasons, it is not possible to provide an optimal tracking system, but for what concerns maintaining the pump-probe frequency shift any P or PI controller will provide sufficient tracking in most cases.

5.2 P and PI controllers as filters

Before detailing the filtering effect of the PID controller, an observation has to be made in order to simplify the description of the process, which is summarized in 5.1 on the next page.

At every step n, the pump-probe frequency shift is ν_n and the gain setpoint is g_{op}, while the new measured gain is g_{meas}. After the feedback, the new pump-probe frequency shift will be changed by an amount equal to $\Delta\nu = -K_P \frac{g_{\text{meas}} - g_{\text{op}}}{\eta}$. In other words, the frequency will try to reach the frequency

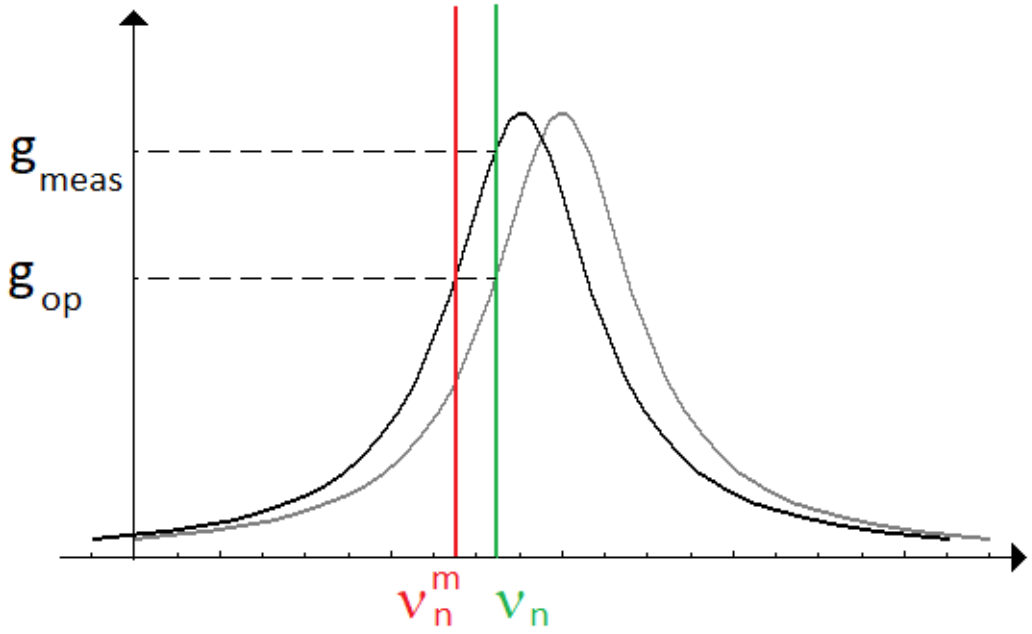

Figure 5.1: Difference between expected gain and measured gain in CC-BOTDA: the curve in grey is the BGS which would return the gain g_{op} with the operating frequency ν_n. In black is the actual BGS that returns the measured gain g_{op} with the operating frequency ν_n, and would return the gain g_{op} if the operating frequency was ν_n^m.

shift value at which the gain would be g_{op} , according to the last measurement. As can be seen from figure 4.5 on page 73, $-\frac{g_{\text{meas}}-g_{\text{op}}}{\eta}$ is equal to the difference between the current pump-probe frequency shift ν_n and ν_n^m, which is the one that should be chosen in order to obtain g_{op} instead of g_{meas}, assuming of course the two frequencies lie in the linear region of the BGS. When a P controller is employed, the new frequency ν_{n+1} will simply be

$$\nu_{n+1} = \nu_n - K_P \frac{g_{\text{meas}} - g_{\text{op}}}{\eta} = \nu_n + K_P \left(\nu_n^m - \nu_n\right)$$

In other words, the contribution of the gain measurement can be ignored and the behavior of the P controller can be described mathematically simply in terms of frequency variation, which in practical measurements will translate to a variation of temperature in this work as it did in [108], but can also translate to strain variations (or other measurands if appropriate sensing fibers are used).

If we define

$$E_n = \left(\nu_n^m - \nu_n\right)$$

as the error of every step, we can say that for a P controller

$$\nu_{n+1} = \nu_n - K_P E_n$$

and, for a PI controller,

$$\nu_{n+1} = \nu_n - K_P E_n + K_I \sum_{i=0}^{n} E_i$$

The meaning of this observation is that the measurement process of the closed loop BOTDA can be treated as reading a signal represented by the fequency ν_n^m corresponding to the measured gain at every step. As shown above the output sequence ν_n is determined by the measured sequence ν_n^m by the formula:

$$\nu_{n+1} = \nu_n + K_P \left(\nu_n^m - \nu_n\right) + K_I \sum_{i=0}^{n} \left(\nu_i^m - \nu_i\right)$$

When $K_P = 1$ and $K_I = 0$, it is immediate to see that the equation above becomes $\nu_{n+1} = \nu_n^m$. In other words, employing a P controller with $K_P = 1$ results in the sensor output being identical to the sequence ν_n^m with only a one step delay. On the other hand, having a P controller with K_P and K_I values lower than 1 and greater than 0 respectively is equivalent to applying a low-pass filter to the measured sequence [106].

Because of this, the tracking and noise suppressing capabilities of P and PI controllers can be decoupled, and the latter evaluated by modeling their performance similarly to what would be done for signal digital filters applied to the ν_n^m sequence. As a further result, their performance can be compared with the one that would be obtained by employing a closed loop BOTDA using a P controller with $K_P = 1$ and applying a different filter to the output.

5.3 Digital filters

Digital filters are mathematical operations that are applied on sampled, discrete-time signals in order to recognize specific patterns, exclude or select signals at specific frequencies or reduce noise [91]. Generally, they are used either for signal selection or signal restoration. Signal selection is used when the desired signal is mixed with interference, noise or other signals, such as distinguishing multiple overlapping voices from a given recording. Signal restoration is required when a signal has been distorted in any way due to hostile measurement conditions or poor equipment.

A very basic example of digital filters is the moving average: every filtered data point is equal to the average of the last N measured data points, where N is a preselected number. As a result, the filtered data sequence becomes a smoothed version of the data sequence, where random fluctuations (like the ones usually generated by noise) are suppressed, but the overall shape of the sequence is also altered.

Compared to analog filters, digital filters cannot be implemented directly on a circuit, but act directly on data converted from analog to digital. Because of this, digital filters can be much more complex and provide levels of performance that are not affected by the hardware limitations of analog filters and thus can be much more complex than analog filters and reach much greater levels of performance [91]. For instance, digital filters are capable of selecting a specific frequency band while excluding all signals outside of it with an almost perfect step-like frequency response, result which is impossible with an analog filter.

Filters can be characterized by three different functions, which are related to each other: the first two are the impulse response and the step response, which are obtained when the filter is applied on an impulse (that is, a measured signal which is 0 at every point except a single one where it is 1) or a step (a measured signal which is 0 before a certain point and 1 afterwards). The third one is the frequency response, which is the function of the attenuation the filter applies to every frequency [91].

Each of these responses alone is enough to define a specific filter in its entirety and its response to every input signal, since any sequence can be defined as either a sum of impulses, step functions or as a spectrum of frequencies. As a consequence, if any of these responses is specified, the other two are univocally determined and can be directly calculated. The difference between the three responses is the information they convey, describing how the filter will react under different circumstances.

Digital filters can be implemented in two different ways. The first and most straightforward is to implement a digital filter by convolving the input signal with a function that is specific for each filter, known as the filter kernel, which corresponds to the signal's impulse response.

The second is to calculate each point of the filtered signal as a sum of the past points from both the input signal and the already filtered data, each point multiplied by a different coefficient. This kind of implementation is known as recursive filter.

Information in signals can be encoded in two possible ways: time domain and frequency domain. In time domain, every point in the sequence describes

when an event occurs and the amplitude of that occurrence, like for example the light output from the sun at every moment.

In frequency domain, relevant information is modulated through frequency and is detected through periodic oscillations in the measured signal.

The different responses of the filter describe how the filter distorts information in the different domains. In particular, filters that have a step response close to the original step will preserve information encoded in time and thus be indicated for time-domain application, while filters that have a step-like frequency response will be able to filter out all the frequencies outside it, and are thus indicated for frequency-domain signals. It is to note that time-domain filter will usually distort information in the frequency domain and viceversa.

In the application of this work, the temperature evolution is a time-domain signal, since it is assumed the temperature is non-oscillating. In addition, since the particular application is a sensor that can be used to measure a wide variety of situations with a wide variety of temperature evolutions, no premade assumptions or models can be made for the measured signal, meaning that particular solutions such as nonlinear filters, which are optimal filters when the evolution of the system producing the signal can be reliably modeled, cannot be employed. Finally, filtering must be performed step-by step, which means other methods for filtering, such as extracting the Fourier transform of a series of data to identify patterns, cannot be employed either, since they require the measurement of a certain event to be completed before it can be identified and filtered. Because of this, P and PI controllers will have to be compared to simple and universal time-domain filters, such as the moving average, which, as will be shown below, is optimal for situations like the ones investigated in this work.

The performance of the filter will be evaluated by two elements: the first will be its step-response, which is extracted by modeling or measuring how the filter responds to a simple step-like input signal. This response will provide information about the speed of the filter, which will be defined as the number of steps required to reach 95 % of the step value. Since the input signal is a step function, the lower the number of steps required, the more the filter will preserve the time domain signal. The second element will be the frequency response: while by frequency-domain standards the response will generally be poor (lacking a flat response at any point in the frequency spectrum), it will provide information regarding the noise suppressing capabilities of the filter. The frequency response can be obtained by calculating the transfer function

of the filter, which is defined as the ratio between the filtered signal point and the measured signal point it originated from. Since the noise is assumed to be purely white gaussian (and thus equal in magnitude at all frequencies), the integral of the transfer function will directly indicate the noise reduction factor.

5.4 Moving average filter

The moving average filter produces each point in the filtered signal by averaging a number of points from the measured signal. In equation form, for a measured signal $x[i]$, the filtered signal $y[i]$ is defined by recursive implementation as:

$$y[i] = \frac{1}{N} \sum_{j=0}^{N} x[i - N + 1 + j]$$

where N is the number of points in the average. Different, equivalent definitions exist, depending on whether $y[i]$ is defined by the average of the last N points before i (like above), the N points after i or around i. The only difference between these definitions is an equal delay in all points. The moving average filter can also be implemented as a kernel filter, where the kernel is 0 except in N points that are equal to $1/N$. In other words, the moving average is the convolution of the signal with a rectangular pulse having a width of N and area of 1.

Using figure 5.2 on the next page as a reference of how the moving average filter works on a noisy step rise and descent, it is evident how the moving average decreases the amplitude of the random noise while also reducing the sharpness of the edges, increasing the number of steps required to reach 100 % of the actual step value. As can be seen from the figures 5.2b on the following page and 5.2c on the next page, increasing the number N of points taken into account for the average increases the noise reduction factor while also increasing the number of steps required to reach the step value, that is the overall "speed" of the filter, and thus further reducing the sharpness of the response. In particular, the noise reduction factor a moving average filter provides is equal to the square-root of the number of points in the average, while the response is equal to that value. For example, a 100 point moving average filter reduces the noise by a factor of 10, and will reach the peak of the step in 100 steps [91].

The moving average filter is optimal for reducing random white noise while keeping the sharpest step response. To understand why this is the case, a

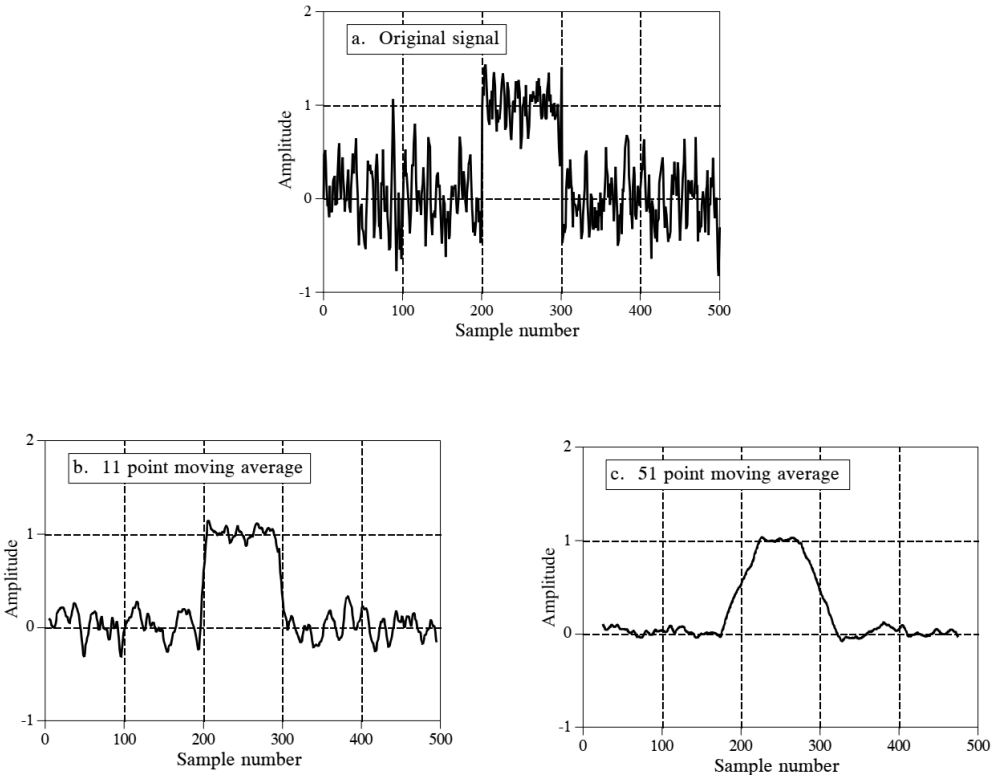

Figure 5.2: Effect of moving average filters on a noisy square pulse. From [91].

sequence of time-domain data which must be passed through a filter with a fixed speed and edge sharpness of N points can be assumed. This would require the filter kernel to have non-zero values in exactly N points. It is assumed that the signal is affected by purely random, uncorrelated noise, and that the goal of the filter is simply to reduce the noise. In this situation, since the noise is random, every point contains the same amounts of noise and information. Because of this, giving a greater weight to a subsection of the N points does not provide any benefit. On the contrary, it makes the final result more dependant on the noise of a single data point. As a result, the highest degree of noise suppression is obtained when the measured data points are all given the same weight, which is achieved when the filter kernel corresponds to the moving average.

By performing the Fourier transform on a rectangular pulse, it can be shown that the transfer function for the moving average filter is

$$H(f) = \frac{\sin(\pi f N)}{N \sin(\pi f)}$$

And the frequency response profile for different numbers of points is shown in figure 5.3:

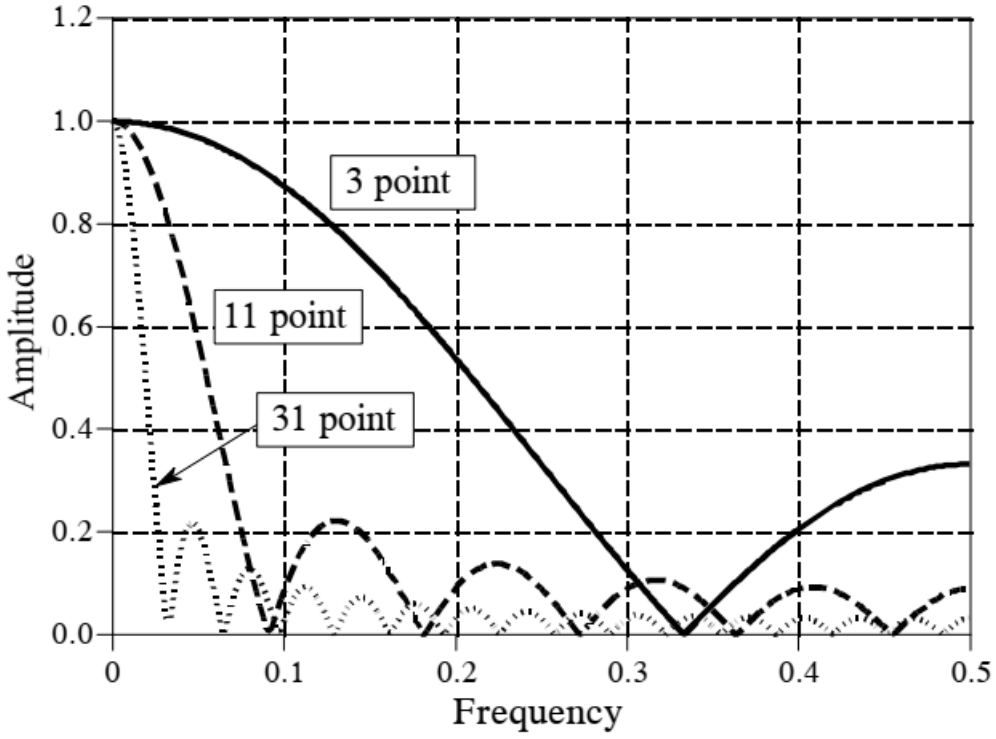

Figure 5.3: Frequency response for different moving averages. From [91].

As stated above, since the moving average filter is optimal for time domain performance, it significantly distorts information in the frequency domain, as can be noted by the fact that there is noin no region of the spectrum where the frequency response is flat, and even in regions where it's lower the suppression is not as strong. Another information that can be extracted from the image is that the greater the amount of points used for the moving average, the greater the suppression is at higher frequencies.

5.5 P controller

5.5.1 Frequency response

As previously said, the P controller can be defined by the following recurrence relation:

$$\nu_n = \nu_{n-1} + K_P \left(\nu_n^m - \nu_{n-1}\right) = \nu_n^m + \left(1 - K_P\right) \nu_{n-1}$$

Applying the z-transform, we obtain [108]:

$$N(z) = K_P N^m(z) + (1 - K_P) z^{-1} N(z)$$

which becomes:

$$N(z)\left[1 - (1 - K_P) z^{-1}\right] = K_P N^m(z)$$

From this relation, the transfer function for P controllers can be extracted [11]:

$$T(z) = \frac{N(z)}{N^m(z)} = \frac{K_P}{1 - (1 - K_P) z^{-1}}$$

The transfer function can be translated from the z-domain to the frequency domain by performing the sostitution $z = e^{i\omega T_S}$, where i is the imaginary unit, ω is the angular frequency and T_S is the sampling period.

5.6 Step response

In order to model the response of the P and PI controllers to a step input signal, it is useful to move the focus from measured and output signals, ν_n^m and ν_n , to the error function sequence that is fed to the controllers, that is defined as $E_n = \nu_n^m - \nu_{n-1}$.

In order to simulate the step function, it can be assumed that E_n is 0 before a certain event at step 0, where $E_0 = 1$ and, from that point forward, the error function will not change again due to causes outside of the controller responding to the new value.

This is equivalent to a situation where $\nu_n^m = 1$ for every $n > 0$.

In this case, for every step the error sequence in a P controller will change as:

$$E_n - E_{n-1} = -K_P E_{n-1}$$

which can be rewritten as

$$E_n = (1 - K_P) E_{n-1}$$

And, knowing that $E_1 = 1$ we have

$$E_n = (1 - K_P)^n$$

which, knowing the definition of the error function, means that the step response of the P controller follows the formula:

$$V_n = 1 - (1 - K_P)^n$$

The number n of steps required to reach a certain percentage d of the step can be extracted by having $\nu_n = d$ and solving for n.

$$d = 1 - (1 - K_P)^n \Longrightarrow (1 - K_P)^n = 1 - d \Longrightarrow n \ln(1 - K_P) = \ln(1 - d)$$

which brings $n = \dfrac{\ln(1-d)}{\ln(1-K_P)}$.

Inverting this relationship, it is also possible to obtain the K_P parameter needed to reach d proportion of the step maximum in n steps:

$$\ln(1 - K_P) = \frac{\ln(1-d)}{n} \Longrightarrow 1 - K_P = \exp\left[\frac{\ln(1-d)}{n}\right] \Longrightarrow$$
$$\Longrightarrow K_P = 1 - \exp\left[\frac{(1-d)}{n}\right]$$

5.7 PI controller

5.7.1 Frequency Response

PI controllers are defined by the following difference relation [12]:

$$\nu_n = \nu_{n-1} + K_P(\nu_n^m - \nu_{n-1}) + K_I \sum_{i=1}^{n} (\nu_i^m - \nu_{i-1}) =$$
$$= K_P \nu_n^m + (1 - K_P)\nu_{n-1} + K_I \sum_{i=1}^{n} (\nu_i^m - \nu_{i-1})$$

To extract the transfer function, the sum $K_I \sum_{i=1}^{n} (\nu_i^m - \nu_{i-1})$ can be decomposed into $K_I(\nu_n^m - \nu_{n-1}) + K_I \sum_{i=1}^{n-1} (\nu_i^m - \nu_{i-1})$. This way, the difference relation becomes

$$\nu_n = K_P \nu_n^m + (1 - K_P)\nu_{n-1} + K_I(\nu_n^m - \nu_{n-1}) + K_I \sum_{i=1}^{n-1} (\nu_i^m - \nu_{i-1})$$

The last sum makes calculating a transfer function impossible, because the number of terms would change with n. To solve this, we can use the same difference relation for $n - 1$:

$$\nu_{n-1} = K_P \nu_{n-1}^m + (1 - K_P)\nu_{n-2} + K_I \sum_{i=1}^{n-1} (\nu_i^m - \nu_{i-1})$$

by rearranging the term we obtain:

$$K_I \sum_{i=1}^{n-1} (\nu_i^m - \nu_{i-1}) = \nu_{n-1} - K_P \nu_{n-1}^m - (1 - K_P)\nu_{n-2}$$

which allows to rewrite the original recurrence relation as

$$\nu_n = K_P\nu_n^m + (1-K_P)\,\nu_{n-1} + K_I\,(\nu_n^m - \nu_{n-1}) + \nu_{n-1} - K_P\nu_{n-1}^m - (1-K_P)\,\nu_{n-2}$$

By separating the PI controller outputs ν_n and the frequencies corresponding to measurements ν_n^m , we have:

$$\nu_n - (2-K_P-K_I)\,\nu_{n-1} + (1-K_P)\,\nu_{n-2} = (K_P-K_I)\,\nu_n^m - K_P\nu_{n-1}^m$$

and performing the z-transform:

$$N(z)\left[1-(2-K_P-K_I)\,z^{-1}+(1-K_P)\,z^{-2}\right] = \\ = N^m(z)\left[(K_P+K_I)-K_Pz^{-1}\right]$$

from which the transfer function can be extracted:

$$T(z) = \frac{N(z)}{N^m(z)} = \frac{(K_P+K_I)-K_Pz^{-1}}{1-(2-K_P-K_I)\,z^{-1}+(1-K_P)\,z^{-2}}$$

5.7.2 Step Response

In appendix A on page 131 it is proven that the error function for a step increase follows two possible progressions:

- An oscillating form with amplitude $(1-K_P)^{\frac{n}{2}}$ when $2-K_P-\sqrt{4-4K_P} < K_I < 2-K_P+\sqrt{4-4K_P}$
- A non-oscillating form expressed as

$$E_n = \frac{1}{2}\left(1+\frac{K_P+K_I}{\sqrt{K_P^2+2K_PK_I+K_I^2-4K_I}}\right)\cdot \\ \cdot\left[\frac{2-K_P-K_I+\sqrt{K_P^2+2K_PK_I+K_I^2-4K_I}}{2}\right]^n + \\ + \frac{1}{2}\left(1-\frac{K_P+K_I}{\sqrt{K_P^2+2K_PK_I+K_I^2-4K_I}}\right)\cdot \\ \cdot\left[\frac{2-K_P-K_I-\sqrt{K_P^2+2K_PK_I+K_I^2-4K_I}}{2}\right]^n$$

When either

$$K_I < 2-K_P-\sqrt{4-4K_P} \qquad \text{or} \quad K_I > 2-K_P+\sqrt{4-4K_P}$$

Through the proof, always shown in appendix A on page 131, it is possible to see that the PI controller will generally reach 95 % of the step response more slowly than a P controller with the same K_P, while also having less noise suppression due to the presence of the integral component in addition with the proportional one.

Visually, the reason for this can be found in the overshoot linked with the step change: right after the sudden increase of the real value, the error of the PI controller will be positive for the first number of steps, increasing the cumulative error that is multiplied by K_I. When the PI controller output reaches the value of the increase, the error sum will still be positive, and will keep on increasing the output, creating the overshoot. It can be said that the integral component in PI and PID controllers adds an inertia in the response of the controller. In [108], the issue of the overshoot was found to be less prominent in situation where the temperature followed a slow ramping process. While this is a very common situation, due to the gradual way heat spreads through objects, it cannot be assumed to always apply. In section 5.9 on page 93 a variant of the PI controller will be proposed that significantly reduces the overshoot.

5.8 Comparison between P controllers and moving average

With the transfer function and the response speed for the P controller, it is possible to compare its performance to the one of the moving average.

To do so, a specific speed value is chosen, which in this case is the number n of steps required to reach 95 % of the maximum step response. Using this value, the corresponding K_P parameter is calculated and the resulting P controller is compared to a moving average with n points in the window.

The four figures 5.4 on the following page show the comparison between the frequency responses of P controllers and moving averages for speeds of 10, 25, 50 and 100 steps respectively (corresponding to K_P values of 0.2589, 0.1129, 0.0582 and 0.0295 respectively).

The x-axis in the graphs are in unit of frequency normalized with respect to the highest sampling frequency which, by the Nyquist theorem, is equal to $1 \,/\, (2T_S)$.

The frequency spectrum for white noise is constant for all frequencies, and every frequency component of the filtered noise will be multiplied by the transfer function at the corresponding frequency. As a result, the total amplitude of the filtered noises going to be determined solely by the integral

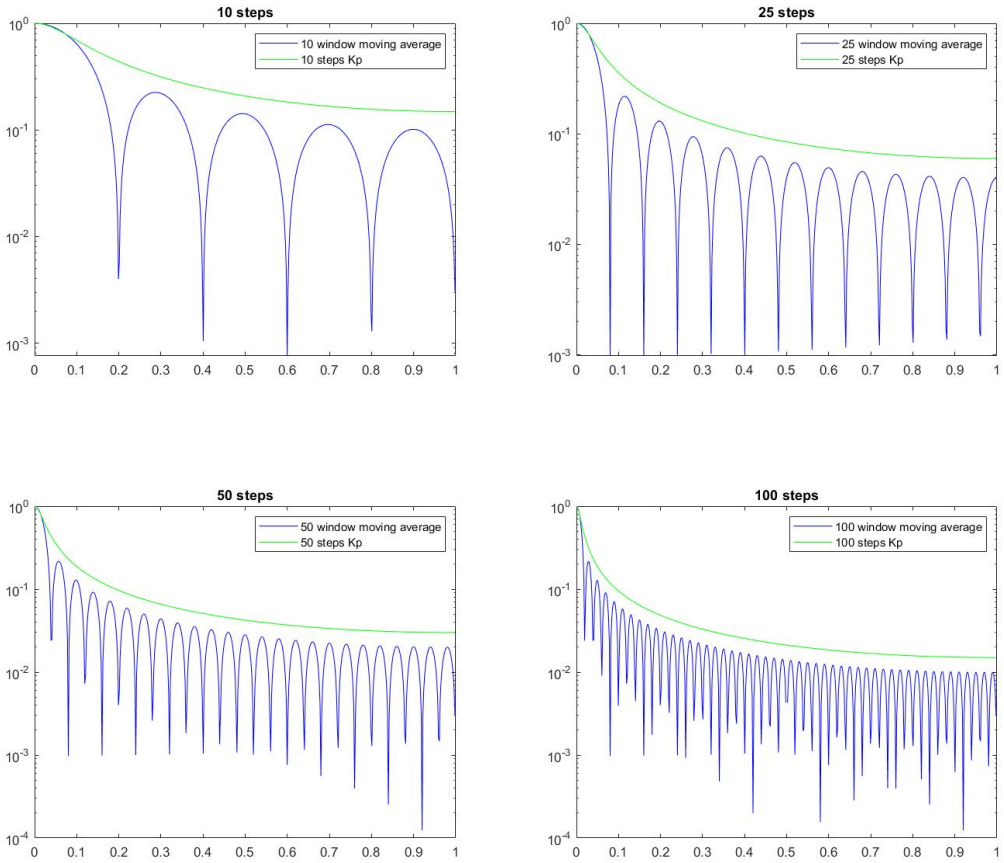

Figure 5.4: Frequency responses of moving average filters and P controllers with an equally fast step response.

of the transfer function, and the noise reduction can be calculated as:

$$NR = \frac{1}{\sqrt{\int_0^1 |H(\nu_{\text{norm}})|^2 \, d\nu_{\text{norm}}}}$$

where ν_{norm} is the normalized frequency. The resulting noise reduction factors for the P controllers and moving averages described in figure 5.5 on the next page as a function of the number of steps required to reach 95 % of the step is shown in figure 5.5 on the facing page.

What can be seen from this result is that both filters follow the same relationship between speed and noise suppression: in order to increase the noise suppression of either filter by a factor of X it is necessary to reduce the speed by a factor of X^2. In addition, at equal speed the moving average has

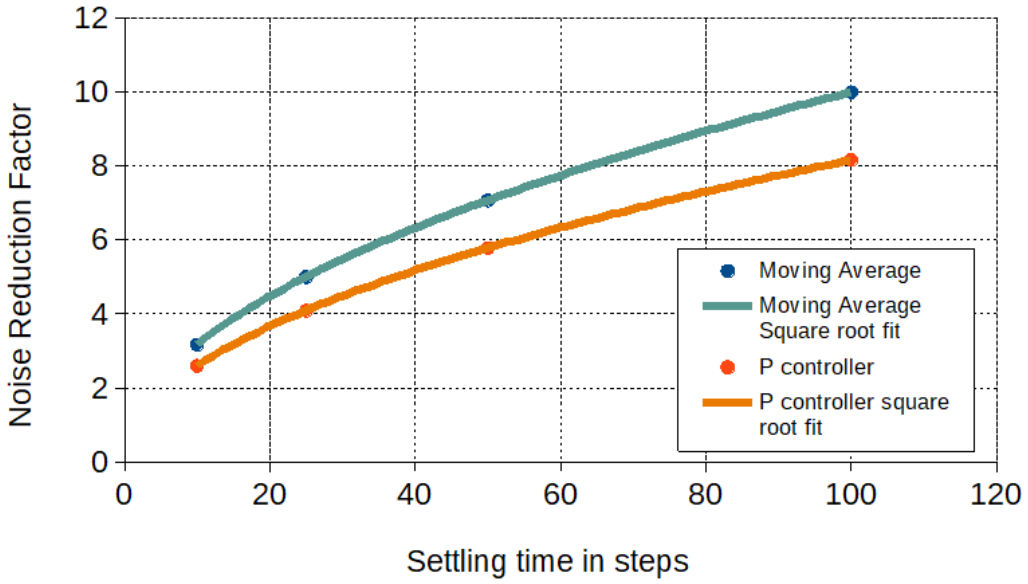

Figure 5.5: Noise reduction factors for the P controllers and moving averages.

a noise reduction factor that is always 22 % higher than the P controller.

Because of this, compared to suppressing noise by employing a P controller with K_P lower than 1, employing a P controller with $K_P = 1$ and then filtering its output with a moving average filter is more efficient in terms of noise suppression. It is to note that this solution will require to keep in memory a number of measured points equal to the size of the moving average window, while the P controller only requires the last output. While this will usually not be an issue in most applications, in situations where only a limited memory storage capacity is available paired with very large averaging windows or very long sensing fibers might require this aspect to be taken in consideration.

5.9 Windowed PI controller

A possible way to reduce the overshoot is to limit the error values that are added in the sum to only the last M, where M is a preselected flat amount. Because only a specific window of errors is considered, this variant of PI controllers will be called windowed PI.

In this situation, the response is

$$\nu_n = \nu_{n-1} + K_P\left(\nu_n^m - \nu_{n-1}\right) + K_I \sum_{i=n-M}^{n} \left(\nu_n^m - \nu_{n-1}\right)$$

Figure 5.6 shows an example of a comparison between the responses of a PI controller with $K_P = 1/128$, $K_I = K_P/1000$ (a) and a windowed PI with $K_P = 1/128, K_I = K_P/100, M = 100$ (b) . As can be seen, the windowed PI better follows the ramp while also having a much smaller overshoot.

To evaluate the noise reduction factor, the transfer function can be extracted from the response as follows:

$$H(z) = \frac{K_P + K_I + \sum_{i=1}^{M} K_I z^{-1}}{1 + (1 - K_P + K_I) z^{-1} + \sum_{i=1}^{M} K_I z^{-1}}$$

Through this transfer function, it is possible to extract the frequency response and compare it to the moving average. As an example, in figure 5.7 on the facing page a comparison between a windowed PI with $K_P = 1/120, K_I = K_P/100$ and $M = 100$ and a moving average of 131 steps is shown. These two parameters combinations were chosen because the windowed PI reaches 95 % of the step response in 131 steps.

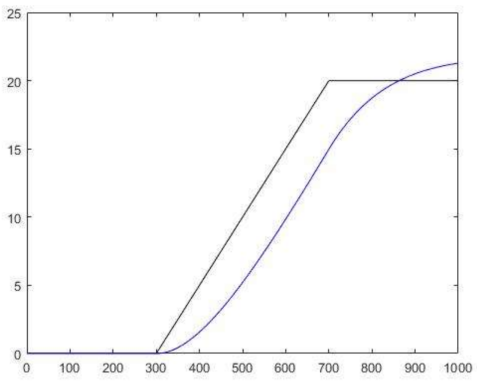

(a) PI controller: $K_P = 1/128$, $K_I = K_P/1000$.

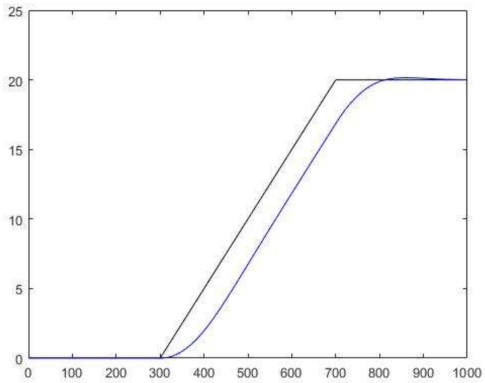

(b) Windowed PI controller: $K_P = 1/128, K_I = K_P/100, M = 100$.

Figure 5.6: Comparison betwen the response of a PI controller and a windowed PI one.

5.10 Result of the comparison

As a conclusion, it can be seen that of all the filters here considered, the most efficient in terms of speed and noise suppression for a signal with time-domain encoded information with no knwon shape and which must be filtered in real time is the moving average.

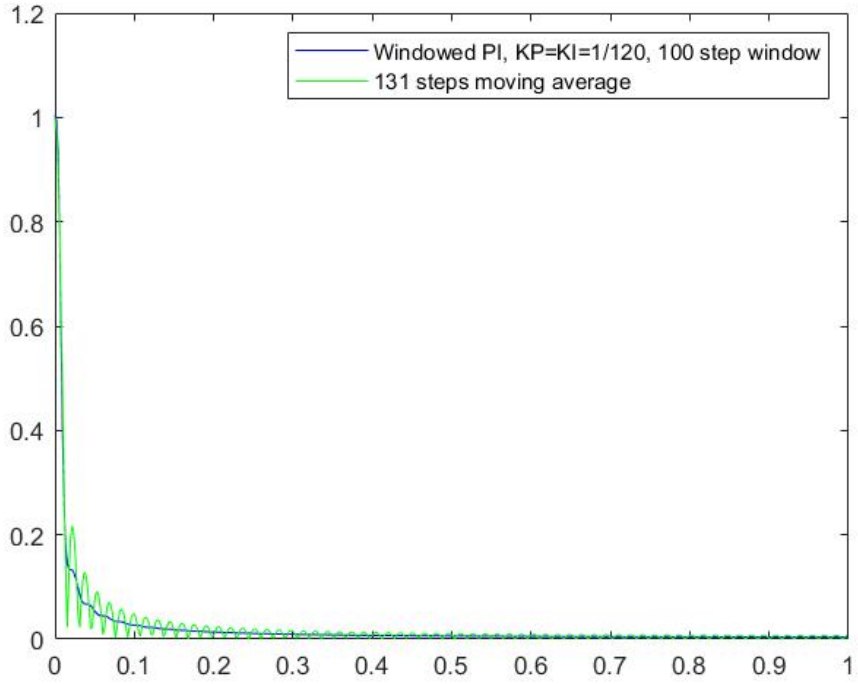

(a) Linear scale.

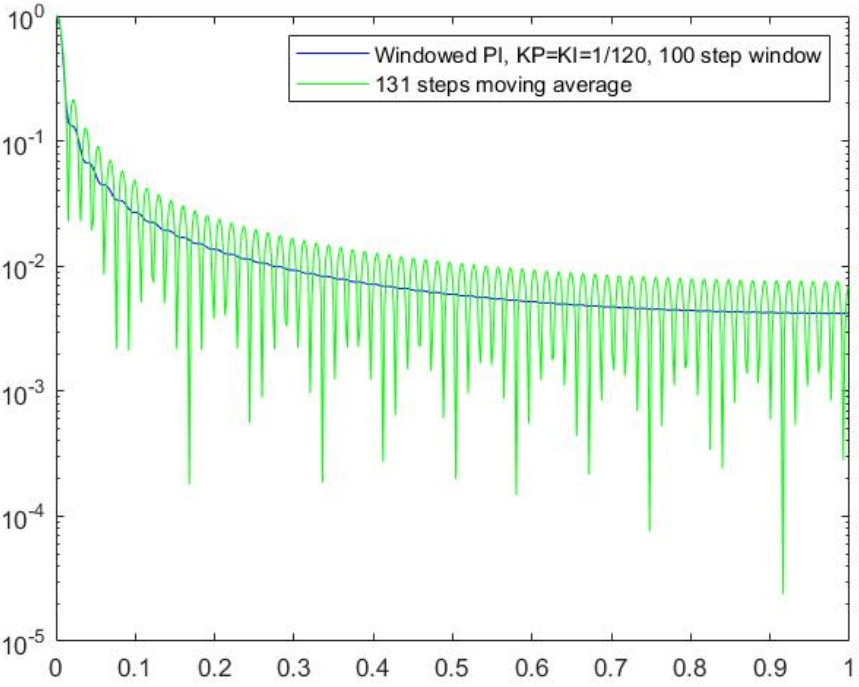

(b) Logarithmic Scale.

Figure 5.7: Frequency response for the windowed PI and moving average.

As was already said, this should not come as a surprise, since when the only source of noise is random (such as white noise) the most efficient way to make a weighted sum of N points to reduce it is to assign the same weight to every point.

In the context of the closed loop BOTDA sensor, this means that, instead of using a P or PI controller with $K_P, K_I < 0$, the best solution is to use a P controller with $K_P = 1$ for the sole purpose of tracking the changes in BFS, and filter its output with a moving average filter to reduce the noise.

The noise reduction factors for the moving average and the windowed PI, which were calculated from the transfer functions shown in figure 5.7 on the previous page are 11.4 and 11.6 respectively, showing that the windowed PI is very close to the moving average in terms of response speed and noise reduction factors (the moving average is still slightly faster, since it reaches 100 % of the response in 131 steps instead of 95 %, but the difference is still small).

5.11 Outperforming the moving average

While the moving average is optimal for linear filters (that is, filters that can be described with a transfer function) and simple recursive filters, it is not necessarily the optimal method in general.

Other more complex filters, known as nonlinear filters, are known to be capable of escluding different forms of noise by employing different methods to predict the state the system they are describing is at each step depending on the present and past measurements [1, 31, 90, 103].

In particular, the Kalman filter is is a nonlinear filter that is used for removing white noise from a measurement of a system in order to estimate a certain related quantity (defined as "state" of the system) [19]. For more examples see [45, 52, 75, 107].

The way this filter operates through a process of prediction of the evolution of the state of the system given the state at the previous measurement step, and confronting it with the actual measurement [105]. The output of the filter is a weighted average between the predicted state and the measured one, where measurements with a smaller uncertainty are weighted more, and the result has a smaller estimation error than either the predicted or the measured state.

It can be shown that, when the model of the system and the measurement errors are known, Kalman filters provide optimal estimation and noise

suppression. See [6, 44, 46, 104] for further examples.

In the situation presented in this work, the application of such a filter is impossible, since the evolution of the relevant quantity (for example, the temperature) depends on the system that is measured, which cannot be determined in advance, and thus there is no way, given the state of the temperature/strain at a given step, to predict the next one.

One thing that is true if not for all, for at least many of the systems that might be measured by BOTDA sensors, on the other hand, is that they can evolve from two stationary states through a dynamic process. In this situation, the monitored value (for example the temperature), starts at a certain level that remains more or less unchanged for a certain period of time until an event causes it to change and reach a new equilibrium at a different level. During the periods where the monitored value is constant, there is no dynamic process to preserve by employing a filter with a limited noise suppression to reduce signal distortion. As a result, a filter with a higher noise suppression level could be used to better characterize the equilibrium, without the risk of distorting the signal.

As a result, one could implement a method that employs a faster filter (as efficient as the moving average) when the signal indicates that there is a dynamic change in process, and a slower filter when the signal indicates a static equilibrium. This method would thus have a speed equal or at least close to the moving average, while providing higher noise reduction in the stationary phases of the measurement, all while relying only on real-time and past data.

In order to do so, the following components are required:

- First, a way to reliably identify the different states of the system through the observed data, while also being able to distinguish between actual changes and variations due to noise.

- Second, two different filters to be employed for the dynamic and static state of the system.

- Third, a way to transition between the two filters which doesn't increase the instability of the measurement and requires a limited number of steps.

5.11.1 Identifying dynamic and stationary states

The only element that can be monitored to detect any changes from dynamic to stationary is the measured data itself. In general, an ideal method of identification should:

- Minimize the delay between the moment the change of state occurs and when the method recognizes it.
- Prevent the risk of falsely recognizing a change of state due to noise.

Of course, due to the presence of noise, simple metrics such as the step-by-step difference of the values or their derivative are not reliable enough to be used, since the step-by-step variation of the signal might be significantly smaller than the noise. This becomes more and more true the fastest the sampling rate for the measurement is. To give an example for why this is the case, a measurement on a system whose temperature climbs by 10 °C at a constant rate over the course of 100 s can be imagined. If the sampling rate is one measurement every 1 s, the step-by-step increase is going to be equal to 0.1 °C. On the other hand, if the sampling rate is one measurement every 10 ms, the step-by-step increase is going to be equal to 0.001 °C. As a result, by a step-by-step point of view the temperature ramp for a measurement that is 100 times faster is also going to be 100 times less steep. At the same time, the noise will remain constant, because it depends on the point-by-point measurement. Because of this, faster measurement times as a general rule will require more steps to distinguish between a changing temperature or strain and noise.

An example of a detection method to move from a stationary to a dynamic state is the following:

1. The signal data is filtered by both a slow and fast filter (which will be discussed below), whose characteristics have to be defined depending on the application and the desired speed or noise suppression.
2. The standard deviation of the last X steps (where X is a parameter that is defined depending on the noise and response speed requirement) of the output for the faster signal, which is going to be named $STD[i]$, is calculated.
3. $STD[i]$ is compared to the mean of the same STD sequence calculated on a previous measurement made when the system was stable (constant temperature/strain), which will be called STD_{flat}.

4. If the system is in a static state, and the absolute value of the difference between $STD[i]$ and the mean of STD_{flat} ($\overline{STD}_{\text{flat}}$) is greater than a certain threshold, is considered as a sign the signal is changing due to a source outside of noise and is considered in a dynamic phase. The threshold can be chosen depending on how sensitive the final filter is required to be. For instance, the threshold could be chosen to be equal to four times the standard deviation of the STD_{flat} sequence ($\sigma\left(STD_{\text{flat}}\right)$) in order to exclude any false positive due to noise.

5. If the system is in a dynamic state, to check if it is transitioning to a static state the following conditions are controlled:

   - The absolute value of the difference between $STD[i]$ and $\overline{STD}_{\text{flat}}$ is lower than a certain threshold, for instance lower than $\sigma(STD_{\text{flat}})$
   - The absolute difference between the output of the fast and slow filter is greater than 4 times $\sigma(STD_{\text{flat}})$. This can be needed to make sure random fluctuations don't cause a shift to static state before the dynamic change of the system has actually finished.

5.11.2 Transition between the two filters of choice

When a change between a steady and dynamic state is detected, a series of decision must be taken in order to translate this change into a change in filter behavior. As has been stated, the basic idea is to employ a faster filter for the dynamic state and a slower one for the steady state, but in order to allow for the smoothest and quickest transition further consideration must be given.

When the transition is from a static to a dynamic state, for instance, a slight difference between the output of the slow-response filter and the fast response one can be expected. In this situation, two options are possible: either have two filters that work in parallel and select the output of either one depending on the state or use a single one whose parameters will change with the state. The first approach will cause the final output to be discontinuous whenever there is a shift from static to dynamic state, but at the same time when this happens the output will be closer to the real signal, while the second approach will yield a smoother but slower response.

When the transition is from a dynamic to a static state, the difference between the slower and faster filter will usually be significant, requiring a transition period between the two. In this situation, the employment of P controllers actually offers an advantage: since the output of a P controller

only depends on its last input, when there is a transition from a dynamic to a stationary state it can be "brought up to speed" by assigning its output value right before the transition to be equal to the one of the faster filter. For the moving average filter, a longer transition period might be needed.

5.11.3 Choice of the filters

As stated above, a faster and slower filter are required to be employed for the dynamic and static states respectively, but can also be useful to determine the state in the first place. The filters used for the latter task can be the same or another set of filters, although the latter case inevitably increases the complexity of the method.

5.12 Practical example

Here is detailed a specific example implementation of the principles described above, for a filter designed to provide a strong ($\sim$ 15) noise reduction factor and variations with an amplitude equal to the standard deviation of the white noise (10 arbitrary units) with ramps with a steepness of 0.1 arbitrary units per step (so a step-by-step increase 100 times smaller than the noise).

The system is composed of three different filters, all filtering the input signal in parallel:

- The first is a P controller with $K_P = 1/128$, which will act as the "slow" filter.
- The second is a window PI controller with a window of 100 steps and $KP = 1/128$ and $K_I = K_P/100$, which will act as the "fast" filter.
- The third is a filter with a variable behavior: when the state is stationary, it behaves like the first filter, while when the sate is dynamic, it behaves like the second one.

The first two filters are used to determine the state of the measurement, while the third one is the output of the method.

The control for the state of the measurement is performed as follows:

- The initial state of the system is considered to be static.
- A sequence of 4000 points where the state is static is pre-computed, the sequence STD_{flat} is extracted as explained below, where the standard

deviation is computed over the last 10 points of the output of the fast filter (windowed PI controller). $\overline{STD}_{\text{flat}}$ and $\sigma(STD_{\text{flat}})$ are extracted from the sequence.

- The sequence $STD[i]$ is computed similarly to STD_{flat}.
- If the state is static, and the average of the last 50 points of the $STD[i]$ sequence is greater than $STD_{\text{flat}} + 4\sigma(STD_{\text{flat}})$, then the state is considered to have shifted from stationary to dynamic.
- If the state is dynamic, the average of the last 50 points of the $STD[i]$ sequence is lower than $\overline{STD}_{\text{flat}} + \sigma(STD_{\text{flat}})$ and the absolute difference between the fast and slow filter output is more than $4\sigma(STD_{\text{flat}})$, the state is considered to have shifted from dynamic to stationary.

As said above, the output comes from the variable filter. When there is a state transition, the following operation are performed on it:

- In the case of a transition from static to dynamic, its parameters change from $K_P = 1/128$ and $K_I = 0$ to $K_P = 1/128$ and $K_I = K_P/100$
- In the case of a transition from dynamic to static, the output of the next step is equal to the average of the last 50 outputs and for the following steps (where it's assumed the system was already static) and the parameters are changed back to $K_P = 1/128$ and $K_I = 0$.

In order to test the performance of this filter, a noisy output was generated from a fixed sequence with a varying signal, corresponding of a step increase, a 800 steps stationary period, a 100 steps long ramp decrease, another 600 steps stationary period and a sinusoidal final section with a period of 100 steps. The fixed sequence and the noisy signal trace are shown in figure 5.8 on the following page.

Its performance is compared to a 132 step moving average filter. The number of steps was chosen to make its response equal to the one of the windowed PI filter when its parameters correspond to the dynamic state.

Since the noise suppression levels are step dependant, in order to calculate them the simulations was repeated 1000 times. Each time a new noisy profile was generated from the same target curve and was filtered by both the moving average and the proposed filter. The outputs of both the moving average

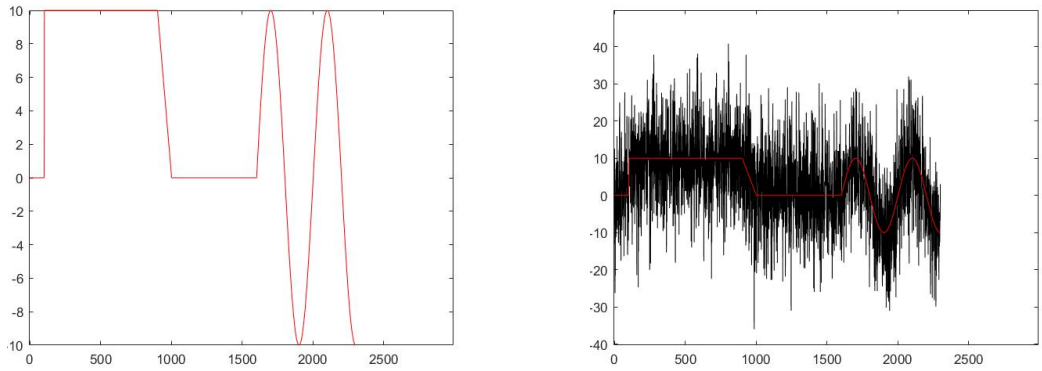

(a) Fixed sequence. **(b)** Noisy signal trace.

Figure 5.8: Fixed sequence and noisy signal trace.

and the implemented method were recorded for each step, and the standard deviation for every step was calculated. In figure 5.9a a comparison between the output of the proposed method (green) and the moving average (black) is shown, while in figure 5.9b a comparison between the standard deviation profiles of the proposed method (green) and the moving average (black) is displayed.

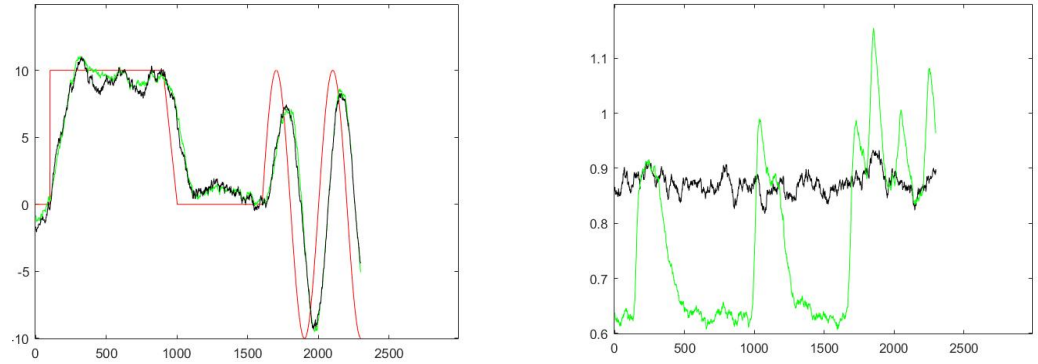

(a) Filtered output. **(b)** Noise levels (original noise level = 10).

Figure 5.9: Comparison between the adaptive filter (green) and the moving average (black) compared to the target.

As can be seen from figure 5.9a, the proposed method is as fast as the moving average, while being closer to the target in the stationary phases. This is more evident looking at figure 5.9b, where the noise standard deviation for the moving average and the filter in the dynamic phase is roughly equal to 0.9 (for a noise suppression factor of 11), while it is equal to roughly 0.62 in the static phase for the proposed method, for a noise suppression of 16. This

increase in noise suppression for the stationary phase is counterbalanced by a brief spike in the noise corresponding to transitions between states, reaching up to 1.1, equivalent to a noise suppression of 9. This is caused by the fact that every time the simulated measurement is repeated the transitions will happen at slightly different steps due to the high noise. This can be seen by the fact the “spikes” are seen corresponding to the ramp or the sine section, but not corresponding to the step, where the step-by-step variation is significant enough to always cause a state transition. Because of this, these spikes might not reflect an increased noisiness of the filter in the actual measurement, but simply the uncertainty linked with the slight variability of the number of steps required for the adaptive method to "detect" the state transition for gradual signals in the presence of heavy noise.

From these results it can be seen how the proposed method has the potential to provide significant performance improvements compared to the moving average whenever is applied to a signal with an alternance between static and dynamic parts, where it’s important to accurately pinpoint the equilibrium values while also being able to describe the dynamic evolution of the system. It is also to note that the one here presented is only one of the possible ways the constituting elements of this method (identification of the states, transition between states and filter set) can be implemented, and other versions might display an even better or more reliable performance.

The contribution of the author to the work presented in this chapter consists of the entirety of the theoretical analysis and simulation that expanded the work done in [108], including the design and development of the adaptive filter method.

6

Experimental implementation of the Closed Loop BOTDA

6.1 Experimental setup

The closed-circuit BOTDA configuration is mostly similar to a standard optical sideband BOTDA in terms of the optical components, and is set to work in a Brillouin loss configuration. The most significant differences are in the electronic components used to generate the probe signals, the data acquisition setup and the timing between the different components. This last element is of particular importance and will require special attention in order for the closed loop control to work.

The setup implemented to evaluate the closed-circuit sensing method is shown in figure 6.1 on the next page.

6.1.1 Light Source

The light for both pump and probe branch is generated by a distributed feedback (DFB), which outputs light in the 1500 nm wavelength range with an intensity of 15.64 dBm. To obtain the pump and probe branches, this light is inserted into a 50/50 optical directional coupler (DC1) to provide both the pump and probe lightwaves.

6.1.2 Pump branch

In the pump branch, an attenuator (ATT) is first used to reduce the intensity of the DFB light below 0 dBm, so that it can be injected into the Semiconductor Optical Amplifier (SOA), an optical amplifier based on carrier recombination

in semiconductors, similar in concept to a laser diode whose end reflectors have been removed. As a result, the incoming light is suppressed unless a current is fed into the SOA, in which case it acts as an amplifier. By feeding it a pulsed electrical signal (produced by an Agilent 33250A 80 MHz arbitrary waveform generator), the pump light is shaped into a 20 ns optical pulse, corresponding to a 2 m spatial resolution.

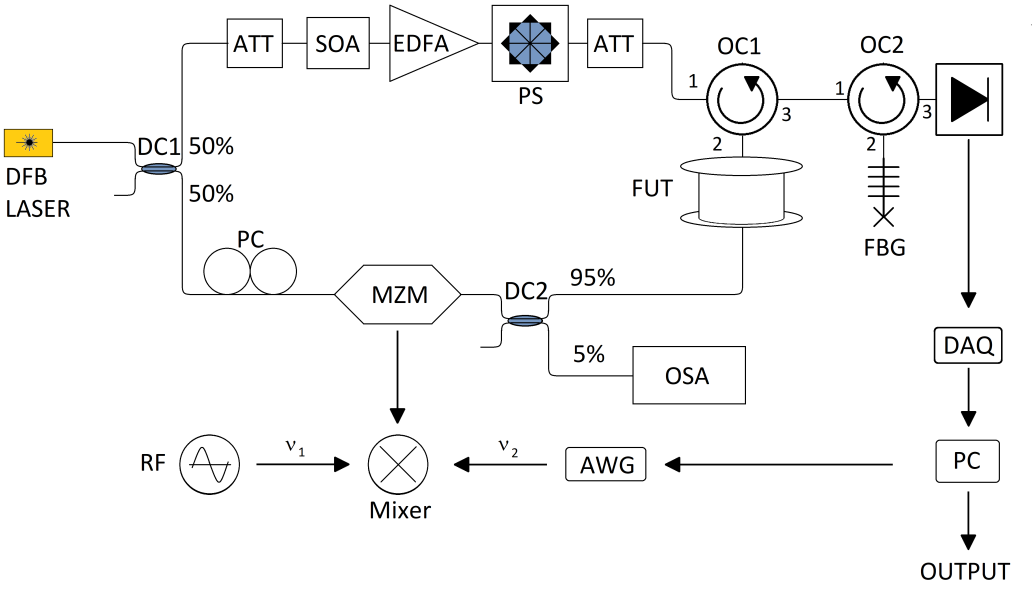

Figure 6.1: Experimental setup.

The pulsed pump is then fed into an Erbium Doped Fiber Amplifier (EDFA), in which the light is amplified through stimulated emission by being injected through an optically pumped rare-earth doped fiber. Out of the amplifier, the intensity of the light pulses is equal to 15 dBm.

The efficiency of the Stimulated Brillouin Scattering depends on the alignment of the polarizations of pump and probe lights, being maximized when they are aligned and minimized when they are opposite. Since the polarizations are subject to random changes as they travel along the fibers due to birefringence, this can cause random fluctuations in the Brillouin amplification. To solve this, a Polarization Scrambler (PS) is used to randomize the polarization of the pump signal, so that along the entire fiber the efficiency of the amplification due to polarization is always constant, because it is averaged over all the possible polarization values.

An optical circulator, which allows passage of light from exit 1 to exit 2

and from exit 2 to exit 3 is used to insert the pulsed pump light into the sensing fiber (exit 1 and 2 of OC1). Before the insertion, a variable attenuator is used to suppress self-phase modulation effects in the sensing fiber.

6.1.3 Probe branch

In the probe branch, as in other OSB layouts, the light is shifted to the probe wavelength with a Mach-Zender Modulator (MZM, model Photline MXER-LN-10), which transfers power from the the laser frequency ν_{DFB} to two sidebands separated from the original one by the modulation frequency. Since the action of the modulator on the light is polarization dependant, a polarization controller (PC) is inserted before it to align the incoming light frequency and maximize the power transfer. Since the frequency will shift overtime, part of the MZM output is coupled out with a 95% / 5% coupler (DC2) and fed into an Optical Spectrum Analyzer, where the power distribution to the sideband can be monitored continuously.

The electrical signal driving the EOM is obtained by mixing the frequency of a microwave generator (RF in figure 6.1 on the facing page) emitting at frequency ν_1 at around 10 GHz and an arbitrary waveform generator (AWG, model Tektronix WX 2181C), which will provide the varying frequencies in a range between 150 and 250 MHz. The spectrum of the wave sent to the MZM is shown in figure 6.2a while the spectrum of the resulting probe light sent into the fiber is shown in figure 6.2b.

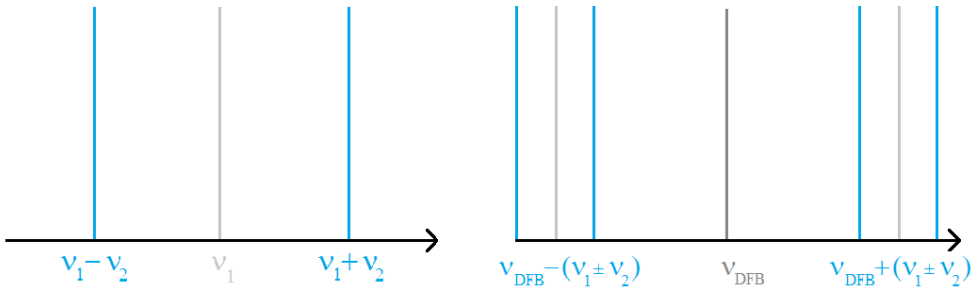

(a) Bands of the signal sent to the MZM (in blue).

(b) Bands of the modulated probe (in blue).

Figure 6.2: Sidebands for the MZM driving signal and the probe.

6.1.4 Filtering and output

The probe light, after entering the FUT and being amplified by the pump, moves through exits 2 and 3 of coupler OC1 and is then reflected by the Fiber Bragg Grating (FBG in figure 6.1 on page 106), which has a bandwidth of 6 GHz and reflects only the frequencies of the upper set of sidebands $\nu_{\mathrm{DFB}}+(\nu_1 \pm \nu_2)$, which are then detected by a 75 MHz bandwidth photodetector (PD). It is to note that due to the necessity of employing a mix of two different frequencies for the modulator, the light reaching the photodetector is composed of two different bands, with only one of those experiencing Brillouin loss, thus reducing the effective signal-to-noise ratio by half. The low bandwidth of the photodetector is also important because the bands will be separated by a frequency difference of around $300 - 400$ MHz (twice the frequency emitted by the AWG), and thus if the photodetector had a higher bandwidth the beating between the two signals would be attenuated by the photodetector and would disturb the measurement.

The voltage signal from the PD is read and digitized by an Agilent Acqiris DAQ card, wich is set with a sampling rate of one measurement every 20 ns, which is equal to the temporal length of every segment. This way, it will be possible to make every point of the trace correspond to a frequency point, which will simplify calculations.

6.1.5 Arbitrary Waveform Generator Output and control

As shown in chapter 4, the AWG signal is temporally segmented into at least N sine wave segments of varying frequencies, corresponding to N segments of equal length Δz, which is the spatial resolution, along the fiber of length L. The duration of each segment is equal to $2n_g\Delta z \,/\, c$, where $c \,/\, n_g$ is the group velocity. Since the spatial resolution is chosen to be 2 m, the length of each impulse is 20 ns. During the measurement process, the n-th frequency segment will start at a frequency $\nu_{\mathrm{op}}(n) = \nu_B(n) - \Delta\nu_B(n)/2 - \nu_1$ where $\nu_B(n)$ and $\Delta\nu_B(n)$ are the Brillouin frequency shift and the Brillouin gain spectrum FWHM at the correspondin n-th fiber segment, which are obtained through conventional BOTDA sensing. With these frequencies, the pump-probe frequency shift will be equal to $\nu_B(n) - \Delta\nu_B(n)/2$ which for every segment n will return half the Brillouin gain $g_B(n) \,/\, 2$.

6.1.6 Data Normalization

It is a known fact that the intensity of the light exiting Mach-Zender modulators also depends on the modulation frequency. As a consequence, while in normal BOTDA every point in the time trace is normalized compared to an area where no amplification is present, in CC-BOTDA this is no longer possible, because every point in the trace will have a dfferent modulation frequency. To solve this, for every measurement the AWG repeats the frequency sequence that defines the segmented probe twice: once with the pump pulse crossing the fiber and once with no other light. This way, a probe trace with amplification and one without are obtained, and the gain is calculated by comparing the corresponding points in the two traces, which were produced by two probe segments which were modulated at the same MZM frequency.

In practical terms, if the frequency sequence has N elements, the trace read from the DAQ will have $2N$ points. If the trace sequence is trace(n), the desired gain sequence gain(n) is calculated as:

$$\text{gain}\,(n) = \frac{\text{trace}\,(n+N) - \text{trace}\,(n)}{\text{trace}\,(n+N)}$$

Where trace(n) is the trace during the first repetition of the frequency sequence, when the pump amplification was present, and trace($n+N$) is the second repetition, with no amplification present.

6.1.7 Timing

In normal BOTDA sensor layouts the probe wave is homogeneous in time, but in this situation this is not the case, and timing becomes essential for the proper fucntioning of the closed-loop measurement. First of all, in order to properly sinchronize the process, the Sync out exit of the AWG (which emits a positive voltage pulse when a new arbitrary sequence begins) is connected to the trigger of the pump pulse generator, which in turns triggers the acquisition card. This way, every measurement starts when a pump pulse is emitted and a probe wave sequence begins. In order for the pump to correctly meet every point in the sequence, it must reach the first segment of the probe when this has reached the end of the fiber, which requires an approriate delay to be added between the time the pulse generator receives the trigger and the moment the trigger is sent.

In addition, once the delay for the optical pump is properly set, the points from the trace must be correctly mapped to the points of the frequency

sequence. If this is not the case, it will result in the closed loop trying to maintain the gain on a fiber segment based on the gain measurement of another segment, causing the closed loop measurement to fail.

An effective way to ensure these last two conditions are obtained is to use a modified frequency sequence for the AWG, which is equal to the starting one except the first and last frequencies are increased by $\Delta\nu_B(n)/2$, so that corresponding to those frequency segments the pump-probe shift will be equal to $\nu_B(n)$ and will cause the maximum Brillouin gain to be measured.

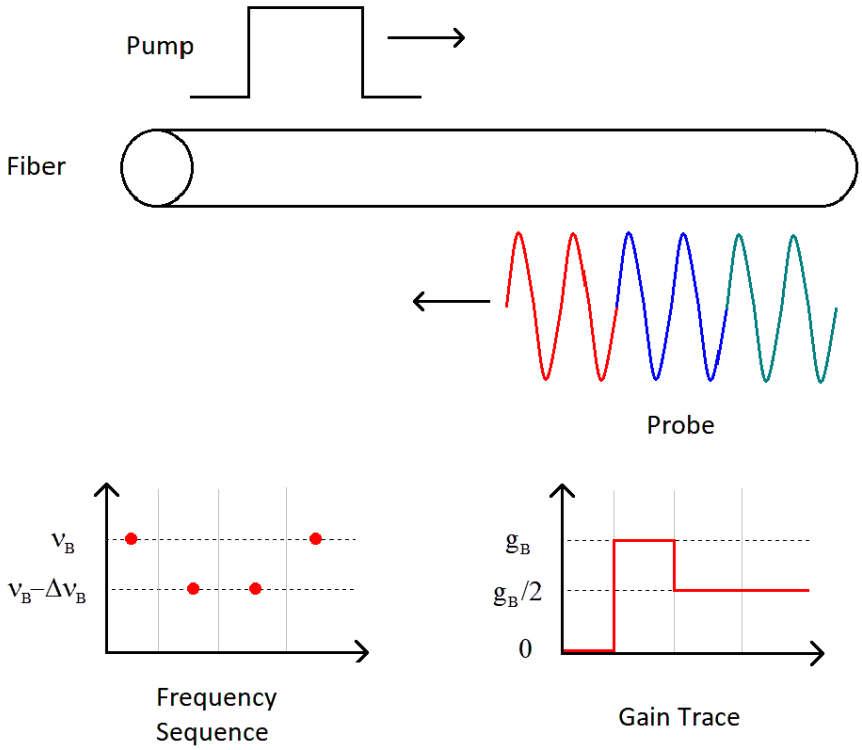

Figure 6.3: Gain measurement when the pump delay is insufficient.

Figures 6.3, 6.4 on the next page, 6.5 on page 112 show how different pump delays affect the measured gain traces from an example 4-point frequency sequence where the first and fourth segments have been increased to ν_B (it is assumed that all points of the fiber have all the same brillouin gain spectrum). When the pump delay is too short (figure 6.3), the pump will meet the first segment of the probe after entering the fiber, and will leave it before the last

segment has entered it. As a result, in the gain trace only the gain increase linked to the first segment will be detected, while the second one will not be visible. On the other hand, when the pump delay is too long (figure 6.4), the first segment of the probe will leave the fiber before the pump pulse enters it and as a result the the gain increase from the first segment will not be detected, while the one from the forth segment will.

When the delay is correct (figure 6.5 on the next page), both gain increases are visible, and by checking in which position in the trace they appear it is possible to detect the points of the trace corresponding to the first and last points of the sequence.

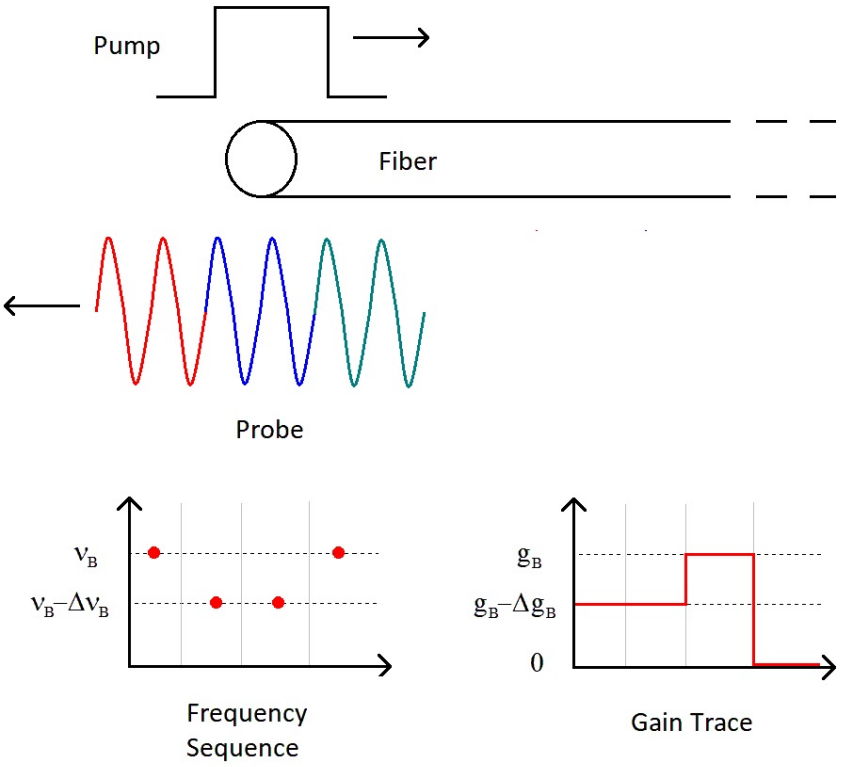

Figure 6.4: Gain measurement when the pump delay is excessive.

6.1.8 Control program

The diagram of every cycle of the control program, which was implemented in LabView 2016, is shown in figure 6.6 on the following page.

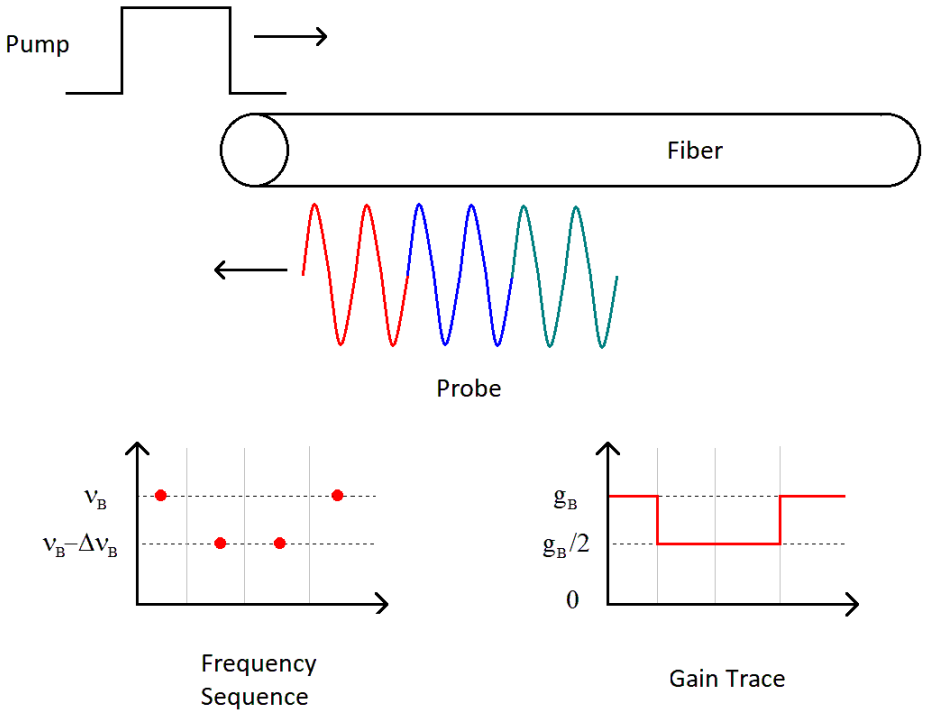

Figure 6.5: Gain measurement with correct pump delay.

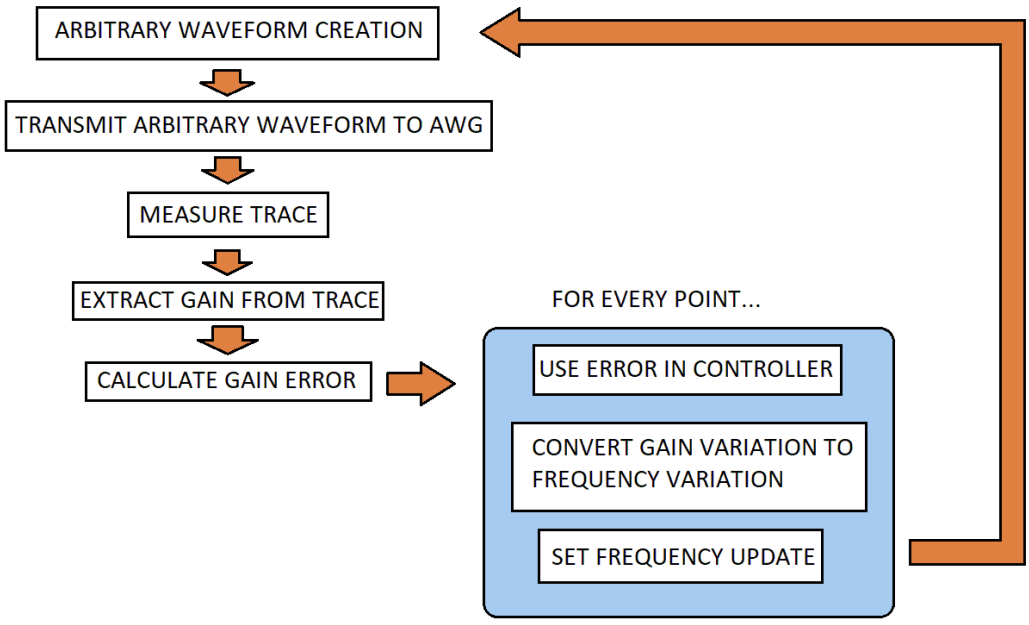

Figure 6.6: Diagram of the control programy.

First, the frequency sequence is used to create the probe wave as a series of sine segments of equal length, which is then uploaded to the AWG as an arbitrary waveform. To provide a smooth transition, the phase of every new sine segment is chosen so that it matches the previous one. The AWG sampling rate is 2 Gsa/s and every segment is 20 ns long, so every segment will be defined by 40 points and the entire sequence will be $40N$ samples long.

After this is done, the DAQ is activated and the intensity trace, which is twice as long as the frequency sequence, is read. Due to the inherent noisiness of BOTDA traces, this trace has to be averaged multiple times in order to be usable. In this work, traces are averaged 512 times.

The gain profile is then obtained by the trace as explained above: the first N points are normalized using the point N positions ahead.

For every point, the gain value is then subtracted to the reference gain to obtain the error, which is then passed to the PI controller. As shown in the previous chapter, this controller can either simply be a non-filtering P controller with $K_P = 1$ whose output will be fed to a digital filter or a PI controller with K_P, $K_I < 1$. As part of the controlling process, the output of the controller for every point is then normalized, compared to the reference gain and converted into the corresponding frequency change, by dividing it by η, which is the slope of the linear region of the BGS. Once this is done, the frequency changes are used to update the frequency sequence for the next cycle.

In addition, since the coefficient η can be excluded from the definition of PID parameters, the K_P values that in chapter 4 were defined as $1/\eta$, $1/4\eta$ and $1/16\eta$, are equivalent to 1, 1/4 and 1/16 and from now on will be defined this way.

6.2 Experimental results

6.2.1 Measurement Time

In [108], the measurement time was 1.7 seconds, because of a series of issues: due to the way the AWG works, the arbitary waveform has to first be determined point-by-point and then uploaded to the generator. As said above, the amount of points that make the arbitrary waveform is equal to $40\,N$ and, when the spatial resolution is 2 meters and the length of the fiber is several kms long, it can amount to hundreds of thousands of points. In addition, the data was transferred through a GPIB, which is significantly slower than

other connection methods such as USB ports. Using the LabView internal measuring method, this process for a 10 km fiber was seen to require around 2 seconds with a GPIB connection and 600 ms with a USB connection. Finally, the DAQ does not have an averaging functionality, which means that in order to perform the 512 averages to reduce noise the DAQ must be activated and read 512 times. Using the LabView internal measuring method, this process was seen to require around 200 ms. From these measurements it can be seen that for long sensing fiber lengths the greatest limit for the measurement time is the upload time required to create the arbitrary waveform.

In the experiment presented in this work, a ~ 950 m-long spool of SMF-28 fiber (corresponding to 475 segments) was employed to showcase faster dynamical measurements. It is to note that, while shorter, this fiber is still one order of magnitude longer than other fibers used for showcasing high-speed measurements.

In these conditions, the time required to extract the measurement from the DAQ becomes the dominant component. In particular, uploading the arbitrary waveform to the AWG required around 60 ms while the time required to measure the averaged trace was around 150 ms, for a final measurement time of roughly 210 ms. This time can further be decreased by reducing the number of averages to 128 and increasing the length of the measurement by 4 times, so that instead of acquiring a single measuring event, 4 are acquired and averaged together. While the time for each single DAQ meauserement is increased, the lower number of averages means that the DAQ must be accessed less times, reducing the total time required for the DAQ measurements to roughly 100 ms, for a total measurement time of 160 ms.

This time could be further reduced with two hardware improvements. One way to do so is to use an AWG which can emit arbitrary waveforms in sequence mode: in this mode, instead of loading the arbitrary waveform point by point into the AWG, the output is assembled by a pre-loaded index of wave segments (which in this case would be a series of sine wave segments at all the possible frequencies in the expected range). This way, at every step the only data to be sent to the AWG would be equal to a single number per fiber segment, representing the position of the index for the corresponding frequency.

Another way to reduce the measurement time would be to employ a DAQ which can autonomosly calculate averages, so that the computer only has to interrogate it once to obtain the averaged trace.

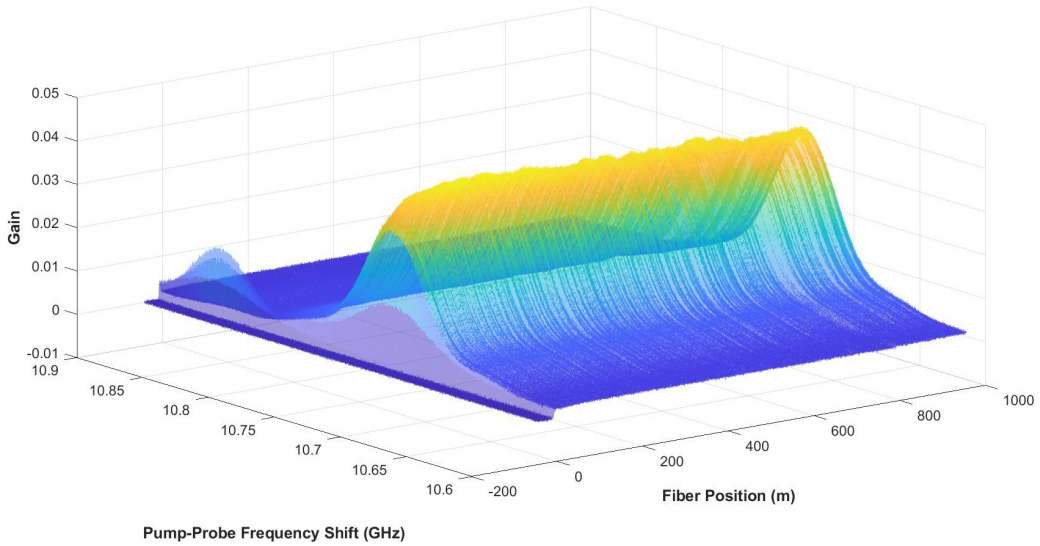

Figure 6.7: BGS distribution along the fiber.

6.2.2 Conventional BOTDA measurement

To determine $\nu_B(n)$ and $\Delta\nu_B(n)$ distribution, alongside the slope η, conventional BOTDA measurements were performed. To maintain the situation as similar as possible to the closed loop, the setup used was the same, but the AWG was set to run a continuous sine wave with a 10 dBm power and 200 MHz frequency. The pump-probe shift was scanned by changing the microwave generator frequency from 10.4 to 10.7 GHz, with a 0.1 MHz step. Every time trace was averaged 2048 times, and was normalized with the last thousand points of the trace, where Brillouin amplification was not present. The results are shown in figure 6.7 and 6.8 on the following page.

The parameters for the Brillouin Frequency Shift are extracted by performing a least-squares Lorentzian curve fitting on the gain data as a function of the frequency shift for every point in the fiber. An example of the spectra and the fitting is shown in figure 6.9 on page 117, while the BFS distribution is shown in figure 6.10 on page 117, alongside the BFS distribution. The full width at half maximum of the BGS was found to be homogenous and equal to 60 MHz for all points of the fiber.

To estimate the ratio η between the normalized gain variation and the frequency shift, a linear fit was performed on the region of every BGS comprising the point closest to the value $\nu_B - \frac{\Delta\nu_B}{2}$ and the 100 points before and after it. To make it compatible with the program, all gain values were normalized by dividing them by the gain value of the central point. An example of the fit is

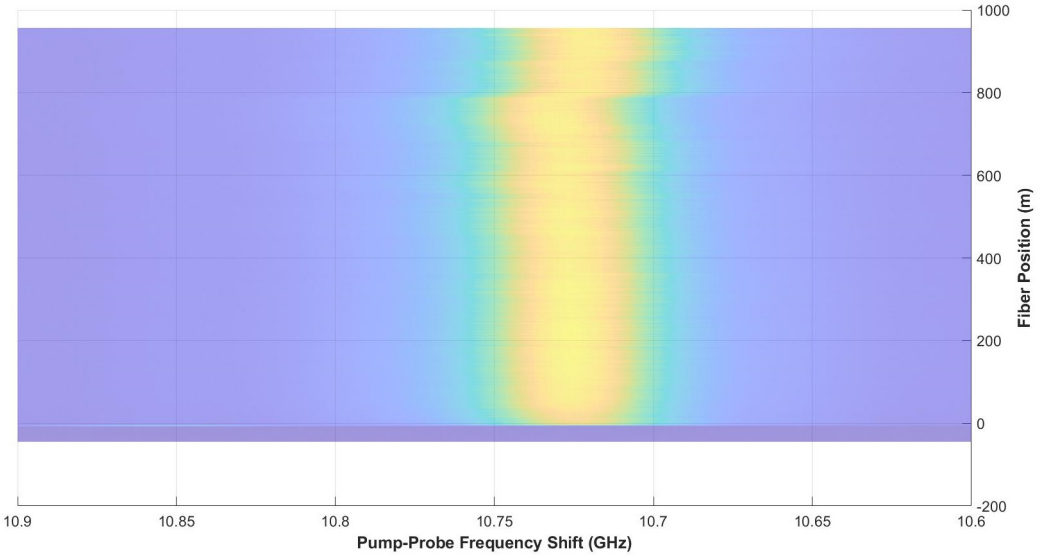

Figure 6.8: BGS distribution along the fiber (view from above).

shown in figure 6.11 on page 118. The coefficient was estimated to be equal to 0.040 ± 0.002.

The reference gain was obtained by measuring the gain of the fiber at the starting frequency values.

6.3 Dynamic Temperature measurements

To test the temperature measurement system, a hotspot at the beginning of the fiber was immerged in a thermic bath, whose temperature was controlled by a LAUDA RM6 thermostat.

First, the sensor was used to track a step-like increase by heating the water up to 35 °C, from a starting room temperature of 22 °C. Once the heating was complete, the measurement process started and during it the hotspot was dropped into the water. Since the hotspot had to be physically moved every time, there was no guarantee the strain conditions were the same for every single experiment, so the conversion between set frequency change and temperature was done by ensuring every tracking measurement included a few points before the hotspot was submerged (when it was stable at 22 °C) and after it was submerged (when it was 35 °C) and using these two sets as references to convert the rest. The results using the K_P and K_I values from [108] are shown in figure 6.12 on page 119.

In terms of the shape of the measurement, the results are similar to the

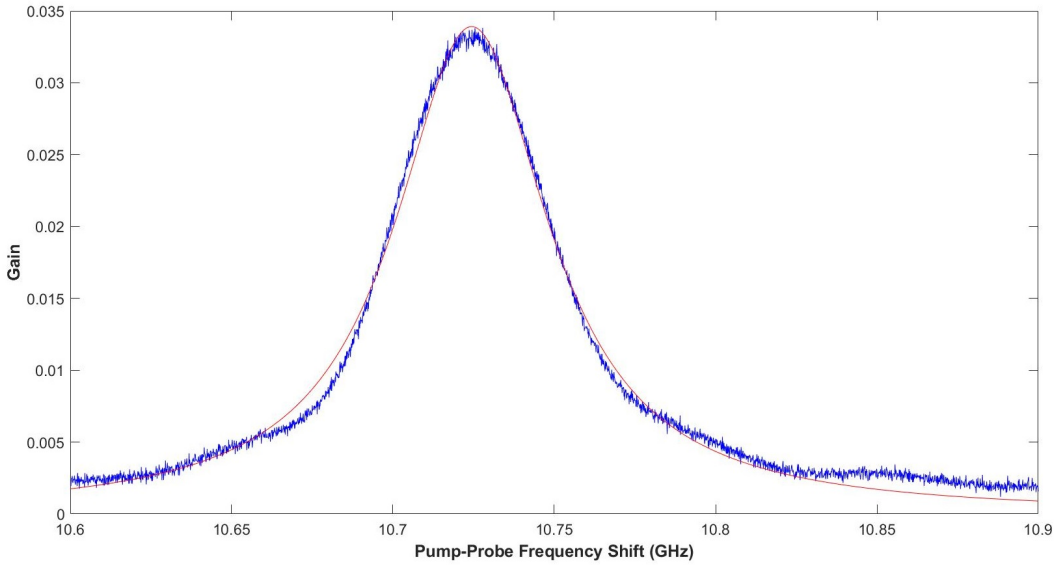

Figure 6.9: Example of a BGS (blue) with a Lorentzian fit (red) at the beginning of the fiber.

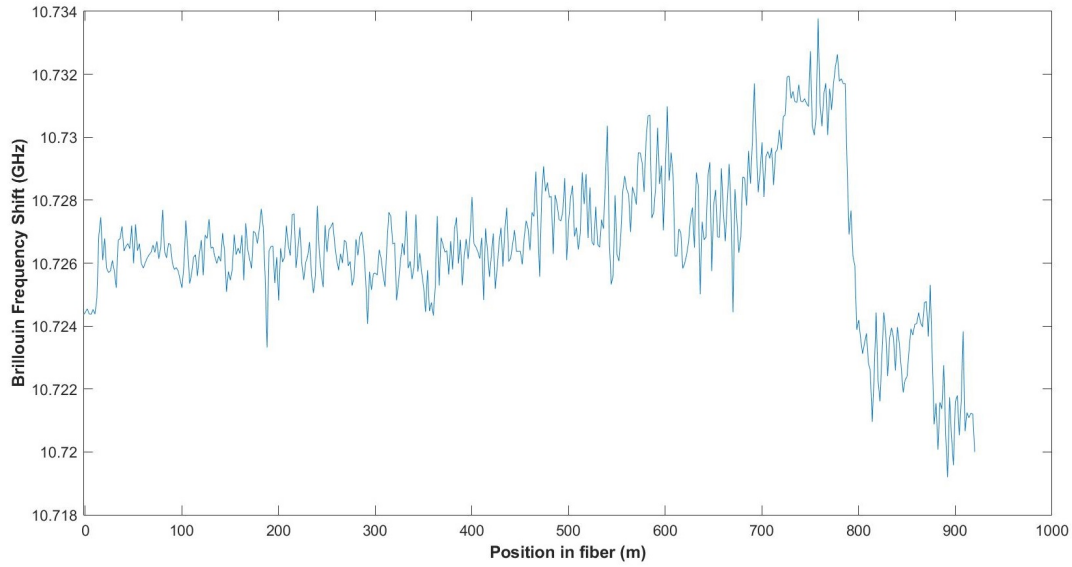

Figure 6.10: BFS distribution along the fiber.

ones in [108]: with lower K_P the system takes more steps to track the real step increase value with the advantage of reduced noise. In addition, the last three cases, where there was a K_I value greater than 0, all show a degree of overshoot positively correlated with K_I.

The frequency noise was estimated by measuring the standard deviation of a sample in a flat zone of the trace. For the step measurement, the zone

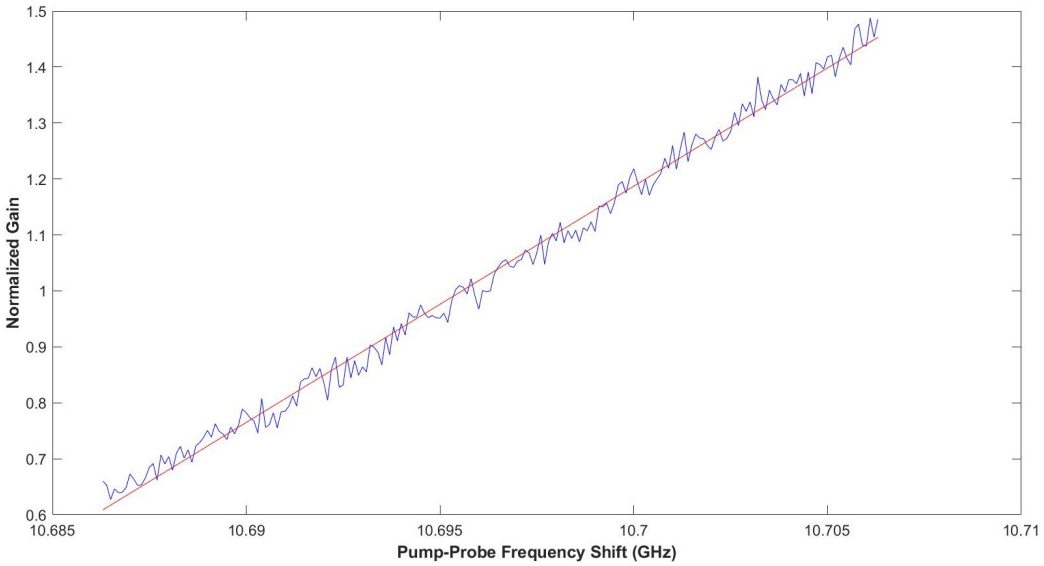

Figure 6.11: Example of the linear fit performed to determine η.

after the step increase was chosen. This was for two reasons: first, the starting frequency set that was obtained from the measurement above is not guaranteed to be the actual stationary state of the fibre hotspot, since moving the hotspot inevitably changes the fiber's BFS distribution due to changes in strain and second, as can be seen for the figures, the measurements required a settling time to reach the frequency shift corresponding to the real temperature. Second, while inside the water the hotspot is less subject to temperature fluctuations and physical vibrations.

The noise measurements show values of 0.77 °C for $K_P = 1$, 0.25 °C for $K_P = 1/4$ and 0.13 °C for $K_P = 1/16$. In the previous chapter, a square root relation was derived between speed and noise suppression, and also the number of steps required to reach 95 % percent of the step value as a function of K_P was:

$$N_{\text{STEPS}} = \frac{\ln 0.05}{\ln (1 - K_P)}$$

which translates to a speed of a single step for $K_P = 1$, 10 steps for $K_P = 1/4$, and 46 steps for $K_P = 1/16$. Looking at the results for P controllers, 95% of the step increase is reached after 18, 30 and 63 respectively. These values are all greater than the expected ones by an amount equal to $18 - 20$ steps. Due to the speed of the measurements, this delay is equal to $\sim$ 3s in terms of time, which is probably the settling time required for the hotspot to be completely submerged and reaching the temperature of the thermal bath. Because of this, the tracking speed is considered to be

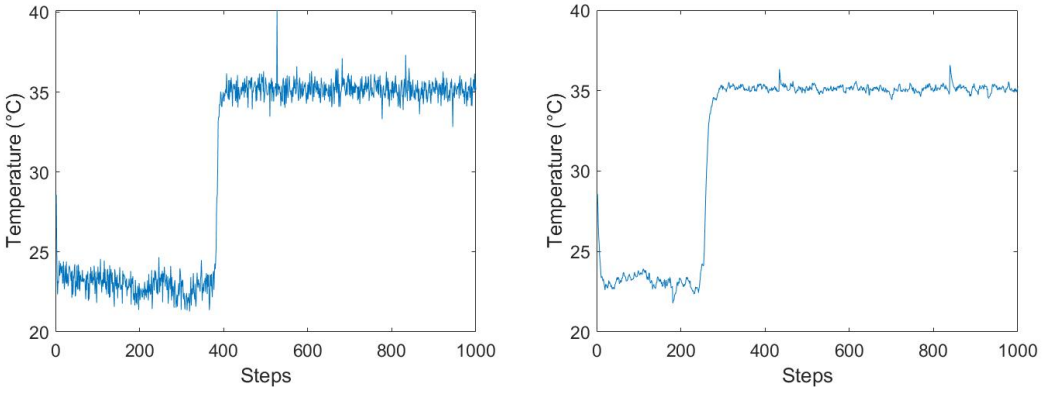

(a) $K_P = 1$.

(b) $K_P = 1/4$.

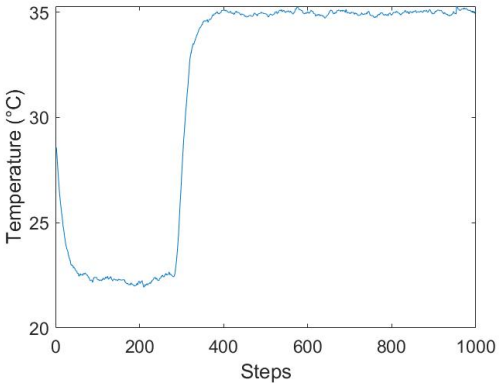

(c) $K_P = 1/16$.

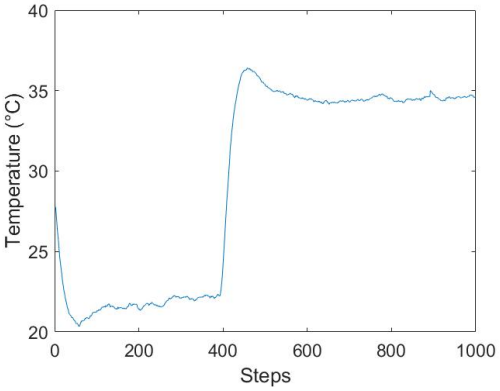

(d) $K_P = 1/16 K_I = K_P/50$.

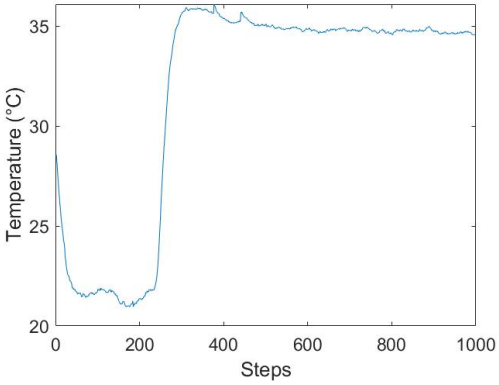

(e) $K_P = 1/16 K_I = K_P/100$.

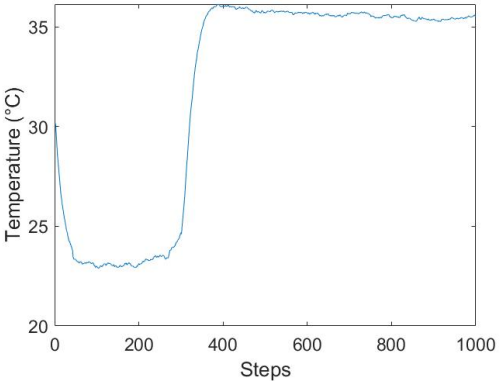

(f) $K_P = 1/16 K_I = K_P/200$.

Figure 6.12: Temperature step increase measurements results.

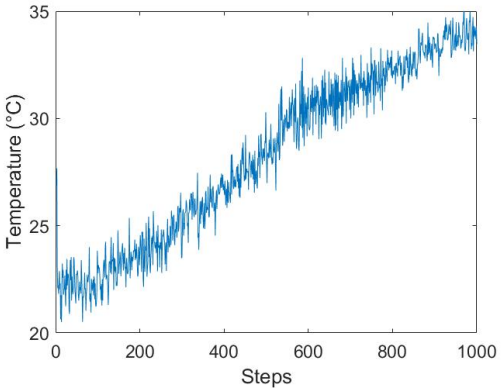

(a) $K_P = 1$.

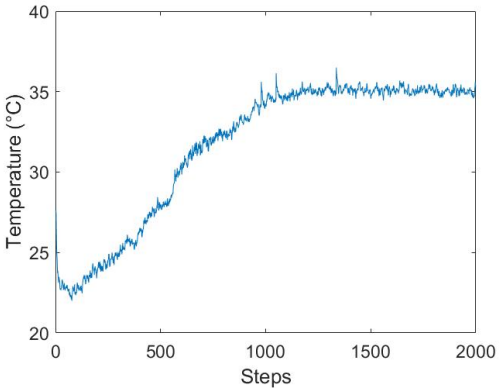

(b) $K_P = 1/4$.

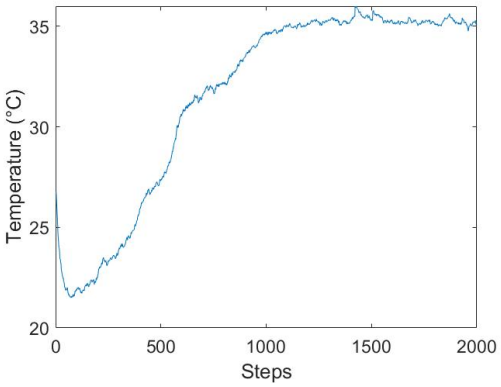

(c) $K_P = 1/16$.

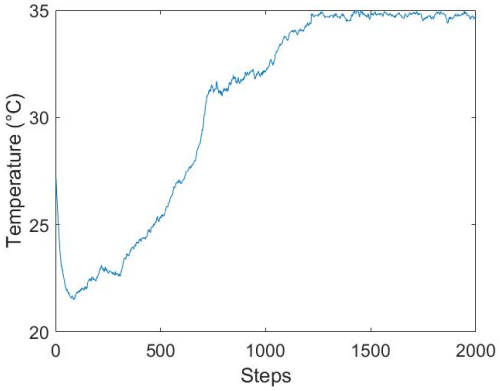

(d) $K_P = 1/16 K_I = K_P/50$.

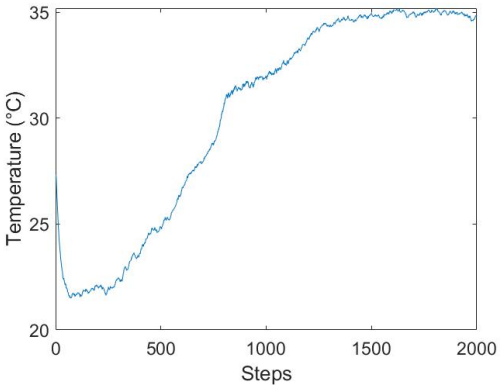

(e) $K_P = 1/16 K_I = K_P/100$.

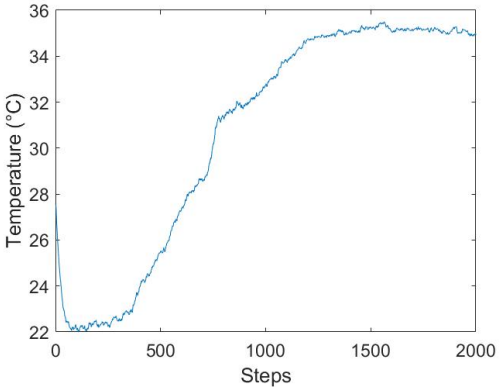

(f) $K_P = 1/16 K_I = K_P/200$.

Figure 6.13: Temperature ramp increase measurements results.

compatible with expected results. The measured noise reduction obtained by reducing the P component from $K_P = 1$ to $K_P = 1/4$, which is 10 times slower, is 3.08, close to the square root of 10 (3.16), and the one obtained by going from $K_P = 1/4$ to $K_P = 1/16$, which is 4.6 times slower, is 2.02, which is also close to the square root of 4.6 (2.14), proving the reliability of the conclusion shown in the previous chapter.

For the PI controller measurements, the measured noise value was 0.18 °C for $K_P = 1/16$ and $K_I = K_P/50$, 0.15 °C for $K_P = 1/16$ and $K_I = K_P/100$ and 0.14 °C for $K_P = 1/16$ and $K_I = K_P/200$, which are compatible with the notion that the noise suppression is increased by an increased K_I parameter. It is to note that the step measurements with PI controllers have the issue of having increased settling times due to the overshoot, which reduce the number of steps that can be used to compute the noise. In addition, small temperature fluctuations can occur during the measurement that can be confused as noise. To correct this, they were manually identified and removed from the sample used to calculate the noise.

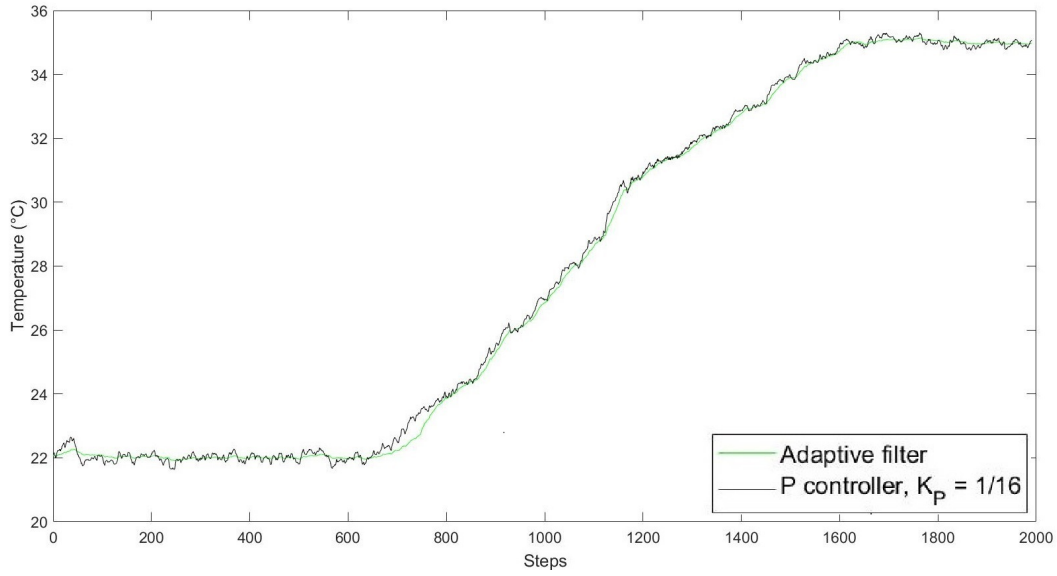

Figure 6.14: Output comparison between the adaptive filter and P controller with $K_P = 1/16$.

Similarly to [108], tracking experiments with a continuously climbing temperature were also performed. In these measurements, the hotspot always remained in the water. At the beginning of the measurement, the thermostat was set to 22 °C, and after $\sim$ 150 steps the thermostat was set to increase the temperature to 35 °C through a mostly linear ramp. The results are shown in

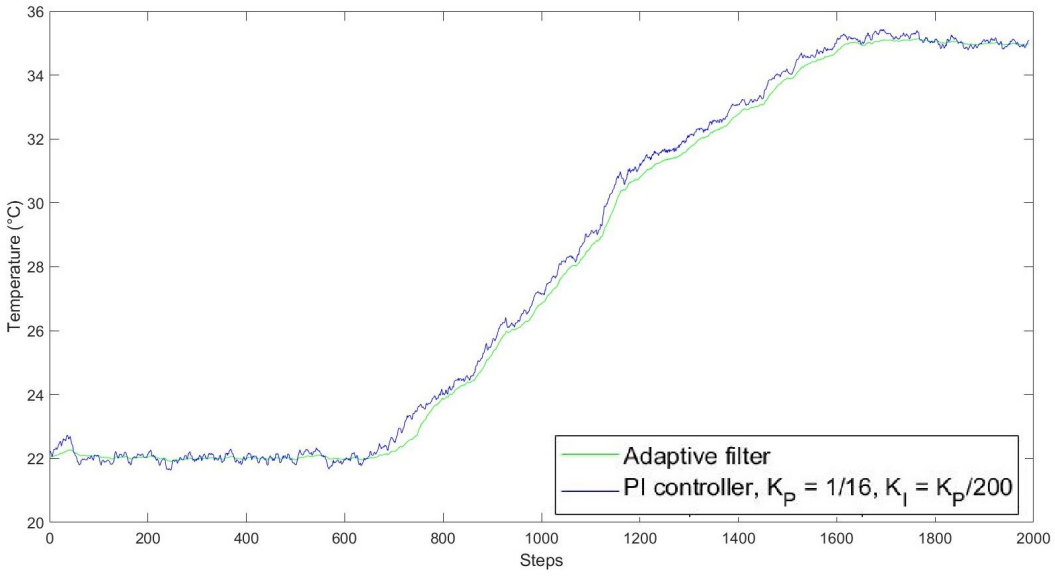

Figure 6.15: Output comparison between the adaptive filter and PI controller with $K_P = 1/16, K_I = K_P/200$.

figure 6.13 on page 120.

The issue of the instability of the temperature can be seen more greatly in these results: since the temperature of the water during the experiment is not static, even when the heating process is stopped the temperature is still changing due to the residual heat in the thermostat's heating coils, which is counteracted by the sensor's cooling mechanism, resulting in an oscillation in the real temperature which is indistinguishable from noise. Because of this, noise measurements are inevitably less reliable than the ones obtained with the previous step increase experiment. Despite this issue, the profiles shown in 6.13 on page 120 have similar elements to the ones seen in [108]: lower K_P parameters correspond to curves that are less sharp and with reduced noise, while adding an integral component K_I increases noise fluctuations while making the starting and end point of the ramp sharper.

6.4 Adaptive filter implementation

To display the potential advantages of the method displayed in the previous chapter to create filters with adaptive behavior, an analogous filtering system was developed to provide a similar response speed to the P and PI controllers with $K_P = 1/16$ and $K_P = 1/16$ and $K_I = K_P/200$ respectively.

These results can also be compared with the output of the new adaptive

filter described in the previous chapter, which was applied in real time to the measurement with $K_P = 1$. The filtering method is defined as follows:

- Three filters are used: a fast control filter, which is a windowed PI filter with $K_P = 1/50$, $K_I = 1/1500$ and a window size of 30 steps, a slow P filter with $K_P = 1/80$ and the output filter, whose parameters will be equal to the slow or fast filter depending on whether the system is in a static or dynamic state.

- A measured sequence of 1000 points where the state was at constant temperature is used to extract the sequence STD_{flat} in a similar way to the one shown in the previous chapter (the standard deviation over the last 15 points of the output of the windowed PI controller applied to the flat sequence). $\overline{STD}_{\text{flat}}$ and $\sigma\left(\overline{STD}_{\text{flat}}\right)$are extracted from the sequence.

- The $STD\,[i]$ sequence is computed as the standard deviation over the previous 15 steps from step i of the output of the fast filter applied to the signal.

- To control whether the system has passed from the stationary to the dynamic state, the average of the last 50 points of the $STD\,[i]$ sequence is checked. If it is greater than $\overline{STD}_{\text{flat}} + 3\sigma\left(\overline{STD}_{\text{flat}}\right)$, then the state is considered to have shifted from static to dynamic. As a result, the output fitler's parameters are changed to the one of the windowed PI controller: $K_P = 1/50$ and $K_I = 1/1500$, with a window of 30 steps.

- If the state is dynamic and the average of the last 60 points of the $STD\,[i]$ sequence is lower than $\overline{STD}_{\text{flat}}$, the system is considered to have shifted from a dynamic to a stationary state.

- When the state transitions from dynamic to static, the output filter's next step value becomes equal to the average of the last 50 outputs and its parameters are changed to $K_P = 1/80$ and $K_I = 0$.

In order to compare its performance to the P and PI controllers mentioned above, the same output measured with $K_P = 1$ was passed through the filtering equivalent of the same controllers, as shown in the previous chapter. As it was stated there, calculating the output of a P or PI controller with a given K_P and K_I from the output of a measurement taken with $K_P = 1$

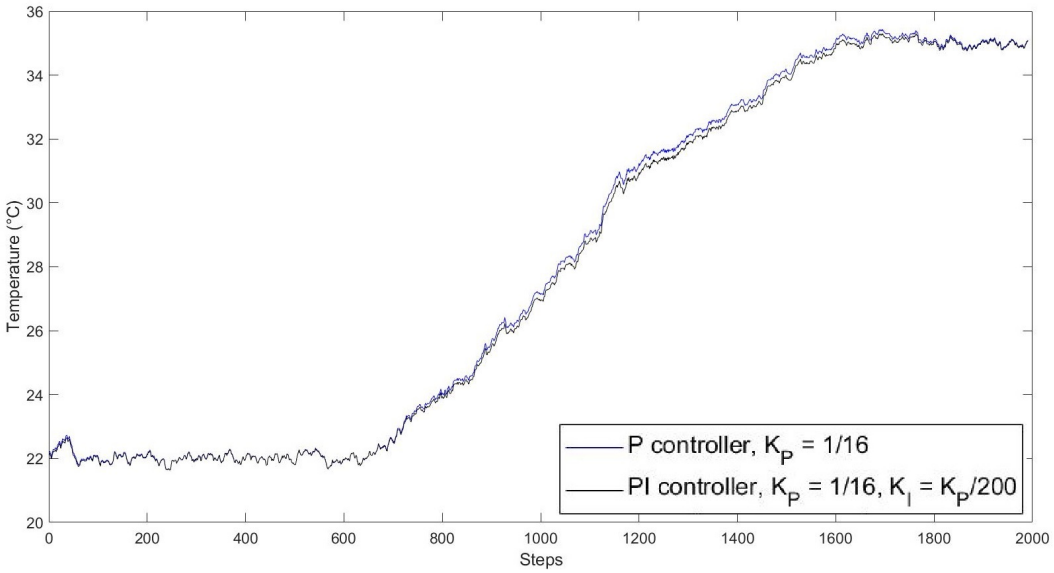

Figure 6.16: Output comparison between the P controller with $K_P = 1/16$ and PI controller with $K_P = 1/16, K_I = K_P/200$.

(which preserves the temperature evolution) is equivalent to making said measurement with the PI controller with K_P and K_I as the parameters.

The comparisons of the results are shown in figures 6.14 on page 121, 6.15 on page 122 and 6.16, first between the adaptive filter and the P controller, then between the filter and the PI controller and finally between the P and PI controller, to verify the validity of this approach.

As can be seen from the figures, the adaptive filter has a speed that is very close to the P controller, and thus it shows a slight delay compared to the PI controller. Despite the similar speeds, noise levels at 35 °C were found to be 0.144, 0.123 and 0.054 °C for the PI, P controller and the adaptive filter respectively. In other words, when the signal is stationary the adaptive filter displays a much higher noise suppression, without significant losses in response speed.

It is to note that the adaptive filter configuration was found through trial-and-error and other configurations could further increase the speed at the cost of a slightly lower noise suppression. What can be seen from this example is that this filtering approach, unlike simple P or PI controllers or moving average approaches, allows to obtain both a quick response and a strong noise suppression in stationary states.

As a further test to compare the noise suppression, a signal similar to the measured one in terms of noise/ramp climb rate ratio and shape (two stable

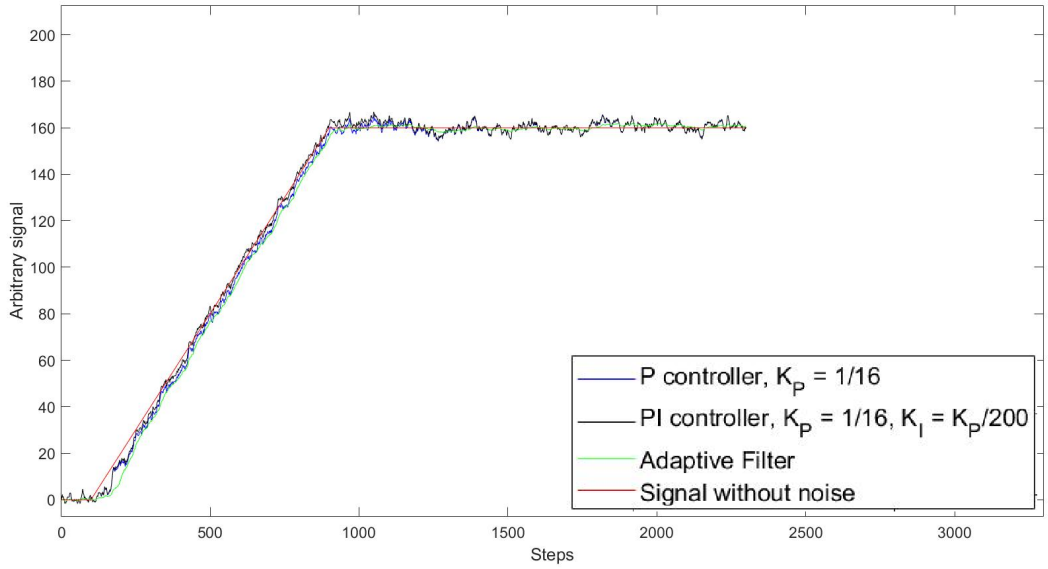

Figure 6.17: Simulated output comparison between the different filters.

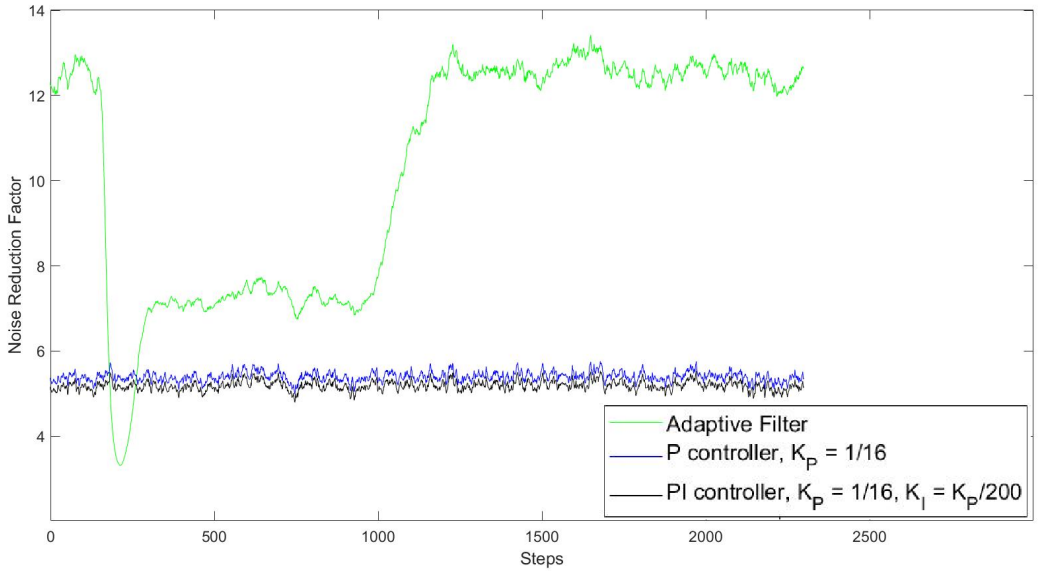

Figure 6.18: Step-by-step noise suppression comparison between the different filters.

states with an 800 steps long ramp between them) was simulated in order to determine the noise suppression at every step of the adaptive filters, the P controller and the PI controller, in a way similar to how it was done in the previous chapter: 1000 signals with new random noise were generated and filtered, and the noise at every step was equal to the standard deviation between all the points at the same step in all the simulations.

The result is shown in figure 6.17 and 6.18. As it can be seen, the adaptive

filter's noise suppression factor is 40 % higher in the points corresponding to the dynamic state, while it is more than double in the points corresponding to the stationary state, which is in agreement to the results obtained from the measurements. The only exception is the first hundred steps at the beginning of the dynamic state where, due to the gradual increase in the signal, the transition from stationary to dynamic states is recognized at different points in every simulation.

The contribution of the author to the work presented in this chapter consists in the recreation of the experimental setup first developed in [108], the study of its limitations and the developments of further improvements. In addition, it includes the implementation of the adaptive filter previously described in chapter 5 and its comparison with previously developed P and PI controllers.

Conclusion

This thesis has focused on devising, studying and experimentally validating methods to overcome two of the main limits for BOTDA applications: the high interrogator complexity/cost and the slow measurement speed.

In the first chapter, the principles of distributed optical fiber sensing, stimulated Brillouin scattering and BOTDA measurements have been overviewed.

In the second chapter, after presenting the two most common methods for providing low-noise and stable pump and probe lightwaves with a tunable frequency shift, alongside their advantages and drawbacks, a first example of an alternative low-cost pump and probe source is presented. It consists of a DFB seed pump feeding a hybrid long cavity ($> 2\,\mathrm{km}$) BRL (LC-BRL) and EDFA layout, where the seed pump is amplified by the erbium doped fiber above the threshold to trigger SBS and generate the recirculating Stokes light. Tunability of the pump-probe frequency shift was obtained by using a piezoactuator to change the BFS of the cavity, which allowed the pump-probe frequency shift to be tuned over a range of 200 MHz. The resulting source provided a probe source with a FWHM linewidth of 2.5 MHz (while the DFB seed pump had a linewidth of 1.5 MHz), a threshold power of 2 mW and a maximum output power of 0.5 mW, which are acceptable values for BOTDA measurements up to at least 10 km. The ring laser was found to add a significant amount of intensity noise in the low frequency range (0–500 MHz), up to $-90\,\mathrm{dB}\,/\,\mathrm{Hz}$, which is a known effect of fiber lasers. Despite this, BOTDA measurements were succesfully performed over a range with 10 km, with a BFS resolution that was found to be around 0.5 MHz, corresponding for most common types of SMF fibers to a temperature and strain resolution of $0.5\,^{\circ}\mathrm{C}$ and $10\,\mu\epsilon$ respectively, which is a serviceable resolution for a wide array of low-end applications where BOTDA with conventional sources sees

little employability due to the interrogator cost.

In the third chapter, a doubly resonant cavity BRL (DRC-BRL) source was presented, which mitigated the issues found with the LC-BRL source shown in the second chapter, namely the high intensity noise and large linewidth of the Stokes output. To reduce the intensity noise, which was found to be mostly caused by mode hopping effects, the length of the cavity was reduced to a few meters. To maintain a high conversion efficiency, the cavity had to be resonant for both the seed pump and the Stokes light, which required careful tuning of the cavity length to the seed pump wavelength, that was achieved through a single cut technique and self injection locking. In order to provide tuning as well as further stabilization, of the pump-probe frequency shift, a wavelength-locking system has been implemented. Compared to the LC-BRL, the resulting source was found to have higher but still acceptable threshold voltage (10 mW) and a higher maximum Stokes output of 2 mW. In addition, the DRC BRL has a greatly reduced intensity noise compared to the LC-BRL, which across almost all the frequency range is below $-140\,\mathrm{dB}\,/\,\mathrm{Hz}$, close to the value of the DFB laser souce ($-150\,\mathrm{dB}\,/\,\mathrm{Hz}$), which rises to $-110\,\mathrm{dB}\,/\,\mathrm{Hz}$ at very low frequencies (0–50 kHz). In addition, the short cavity induces a strong linewidth narrowing effect for both the seed pump and the Stokes output. As a result, the linewidth of the seed output was measured to be 10 kHz, down from an original DFB linewidth of 350 kHz The wavelength-locking system was found to allow for a pump-probe frequency shift tunability over a range of at least 200 MHz with sub-kHz accuracy and fluctuations below 200 Hz in the 10 ms timeframe (typical for a signle BOTDA measurements) and 400 Hz for longer timeframes (120 s), resulting in a highly tunable, accurate and stable shift. Thanks to the reduced intensity noise compared to the LC-BRL, the new source is predicted to reduce the BFS, temperature and strain resolutions by a factor of 3.5. Compared to the results obtained in the previous chapter, this would results in resolutions of $\sim 0.14\,\mathrm{MHz}$, $\sim 0.14\,^{\circ}\mathrm{C}$ and $2.9\,\mu\epsilon$.

It should be noted that the analysis of the behaviour of different BRLs performed in this work also allows to further understand both its amplification mechanics and its resonant behaviour, which can prove to be relevant not only for developing a source for BOTDA but also for all other applications in which BRLs are employed, such as communications and LIDAR detection.

In the fourth chapter, a closed-loop implementation of the slope-assisted BOTDA method was presented as a possible way to perform dynamical BOTDA measurements. The closed-loop method allowed to surpass one of the major limitations of slope-assisted BOTDA, namely the reduced measurement

range. Finally, an example application in measurement sensing is showcased.

In the fifth chapter, the behavior of the PID controller used for the closed-loop measurements was studied, with particular focus on its tracking and noise filtering functions. Afterwards, the PI controller in filtering terms was found to have both lower noise suppression and overall worse step response speed compared to the P controller, due to the overshoot associated with the Integral component. In addition, the P controller was found to have a noise reduction factor which grew at a similar rate to the moving average compared to the step response speed, but the noise reduction for the moving average was found to always be 22 % higher. Finally, an adaptive filter method was presented, which consisted of a way to determine if the signal being filtered (in this case a continuous temperature reading) was, compared to the time required for a single measurement, in a dynamic (rapidly evolving) or stationary (constant or slowly changing) state, and using filters better suited for each: a filter with a faster step response and less noise reduction for the dynamic state and one with a slower step response and high noise reduction to better characterize the equilibrium of the stationary one. In order to showcase the performance of this adaptive filter, its performance was compared with a moving average filter on a batch of simulated noisy signals. The proposed method was found to have equal response speed with the moving average and equal noise suppression in the dynamic state. When the signal was slowly varying (compared to timeframes roughly ~ 100 times the measurement period), on the other hand, the adaptive filter had a noise reduction factor which was 50 % higher. It is to note that, while other filters (such as the Kalman filter) can outperform the moving average filter in similar conditions, they require the model of the measured system evolution to be known in advance, which is not generally known in BOTDA applications. The adaptive filter, on the other hand, only requires a general idea of the minimum changes in relation to the signal noise the filter is required to "recognize" as transitions from the static to dynamic state, which is believed to be a much less stringent requirement.

In the sixth chapter the closed loop measurement system was experimentally implemented. Unlike the experimental demonstration described in the fourth chapter, which was made over a 10 km long sensing fiber, this implementation was made on a 1 km long sensing fiber. This improved the measurement time from 1.7 s to less than 200 ms, showcasing faster dynamic measurements over ranges that are still longer than the ones used for demonstrating other fast measurement methods, which were usually in the order of 100 m. In addition,

the two main hardware issues that limited the meauserement speed were the AWG operation mode (arbitrary waveform) and the DAQ board not being an averager, and solutions were found which are expected to greatly improve the performance, namely use an AWG capable of working in sequence mode with a pre-loaded library of adequately long sine segments and use a DAQ that also works as an averager. Similar experiments to the one in the fourth chapter were performed, with similar P and I coefficients, and the obtained results were similar to the ones expected from the theoretical analysis in the previous chapter for what concerns P controllers, while PI controllers were in line with the results from the work shown in the fourth chapter. Finally, using the conclusion at the beginning of the fifth chapter regarding the possibility of decoupling the tracking and filtering behavior of PID controllers, a measurement with $K_P = 1$ was performed and the resulting trace was used to compare the performance of similar P and PI controllers with parameters equal respectively to $K_P = 1/16$ and to $K_P = 1/16$, $K_I = K_P/200$ controllers with an implementation of the adaptive method shown in the previous chapter. The shape of the resulting filtered traces for the P and PI controller were similar to the ones obtained by setting the parameters at the same values from the beginning, giving further support to the conclusion found at the beginning of the fifth chapter.

In addition, while the implemented adaptive filter had a speed similar to the one of the P controller, it had noise suppression which was found to be 40% higher in the parts of the measurements where the temperature was ramping up. On the other hand, in the parts of the measurement where the temperature was slowly changing for timeframes of at least 15 seconds (roughly a hundred times the single measurement time), noise suppression was even higher, becoming more than double the one provided by the P controller. These results help show how the proposed method is expected to provide improved noise suppression with similar step responses compared to previously showcased signal processings method for CC-BOTDA, especially when the measurand alternates dynamic to slowly changing phases. It should be noted that, also due to the special circumstances that verified during this year, the results shown here are still preliminary: further analysis will help provide more complete results and better understand the practical applications where this technique would be most beneficial. Finally, due to the purely digital nature of this adaptive filtering method, its applicability in other fast BOTDA applications, such as SA-BOTDA, could also be explored.

A

PI Controller: step response modeling

A.1 General form for all PID controllers

In the signal step increase detailed in 5.9 on page 93, a generic PID controller will work so that for every step the error sequence will change by an amount equal to:

$$E_n - E_{n-1} = -K_P E_{n-1} - K_I \sum_{z=0}^{n-1} E_z - K_D \left(E_{n-1} - E_{n-2}\right) \tag{A.1}$$

This relation is a recurrence relation, that can be treated as a discrete version of a differential equation [12]. Let

$$\Delta E_n := E_n - E_{n-1} \qquad \text{and} \qquad \Delta^2 E_n := \Delta E_n - \Delta E_{n-1}$$

Then (A.1) becomes:

$$\Delta E_n = -K_P E_{n-1} - K_I \sum_{z=0}^{n-1} E_k - K_D \Delta E_n \Longrightarrow \tag{A.2}$$

$$\Longrightarrow \left(1 + K_D\right) \Delta E_n = -K_P E_{n-1} - K_I \sum_{z=0}^{n-1} E_z \tag{A.3}$$

By applying Δ to both sides of (A.3) (equivalent of subtracting (A.3) for $n = n - 1$ to (A.3) for n) we have:

$$\left(1 + K_D\right) \Delta^2 E_n = -K_P \Delta E_{n-1} - K_I E_{n-1} \tag{A.4}$$

Which becomes,

$$\left(1 + K_D\right) \left(\Delta E_n - \Delta E_{n-1}\right) = -K_P \Delta E_{n-1} - K_I E_{n-1} \Longrightarrow \tag{A.5}$$

$$\implies (1+K_D)\,\Delta E_n = (1+K_D-K_P)\,\Delta E_{n-1} - K_I E_{n-1} \tag{A.6}$$

And, remembering that $\Delta E_n = E_n - E_{n-1}$ and also $\Delta E_{n-1} = E_{n-1} - E_{n-2}$ we finally obtain:

$$(1+K_D)\,(E_n - E_{n-1}) = (1+K_D-K_P)\,(E_{n-1} - E_{n-2}) - K_I E_{n-1} \implies \tag{A.7}$$

$$\implies (1+K_D)\,E_n = (2+2K_D-K_P-K_I)\,E_{n-1} - (1+K_D-K_P)\,E_{n-2} \tag{A.8}$$

A.2 Solution to the recurrence relation

Equation (A.8) is espressed in the form of a homogeneous linear recurrence relation with constant coefficients (an equation of the form $a_n = c_1 a_{n-1} + c_2 a_{n-2} + \cdots + c_d a_{n-d}$). The solution has d degrees of freedom: the sequence will be determined by the first d elements, which can vary.

The coefficients $C_1, \ldots, C_d$ determine the characteristic polynomial

$$p\,(t) = t^d - c_1 t^{d-1} - c_2 t^{d-2} - \cdots - c_d$$

whose roots $r_1, \ldots, r_d$ if distinct, determine the solution of the relation, which is defined as

$$a_n = k_1 r_1^n + k_2 r_2^n + \cdots + k_d r_d^n$$

Applying this characteristic polynomial for (A.8), its roots can be found through the equation

$$\begin{aligned}(1+K_D)\,r^2 &= (2+2K_d-K_P-K_I)\,r - (1+K_D-K_P) \implies \\ \implies (1+K_D)\,r^2 &- (2+2K_D-K_P-K_I)\,r + (1+K_D-K_P) = 0\end{aligned} \tag{A.9}$$

The roots of (A.9) are:

$$r_{1,2} = \frac{2+2K_D-K_P-K_I}{2+2K_D} \pm \pm \frac{\sqrt{(2+2K_D-K_P-K_I)^2 - 4\,(1+K_D)\,(1+K_D-K_P)}}{2+2K_D}$$

In this situation, d=2, and the solution will be of the form: $E_n = C r_1^n + D r_2^n$

The roots can also be written as:

$$r_{1,2} = \frac{2+2K_D-K_P-K_I \pm \sqrt{K_P^2 + 2K_P K_I - 4K_D K_I + K_I^2 - 4K_I}}{2+2K_D} \tag{A.10}$$

A.3 Case with PI controller

For $K_D = 0$ we have:

$$E_n = Cr_1^n + Dr_2^n = C\left[\frac{2 - K_p - K_I + \sqrt{K_P^2 + 2K_PK_I + K_I^2 - 4K_I}}{2}\right]^n + \\ + D\left[\frac{2 - K_p - K_I - \sqrt{K_P^2 + 2K_PK_I + K_I^2 - 4K_I}}{2}\right]^n \tag{A.11}$$

We also know that $E_1 = 1$, $E_{n<1} = 0$, and $E_2 = 1 - K_P - K_I$.

If $K_P^2 + 2K_PK_I + K_I^2 - 4K_I < 0$, the component under square root in (A.11) will be imaginary. This condition is verified for

$$2 - K_P - \sqrt{4 - 4K_P} < K_I < 2 - K_P + \sqrt{4 - 4K_P}$$

Taking examples from [108], we can see that when $K_P = 1/16$ this condition is verified for values of K_I such as:

$$2 - \frac{1}{16} - \sqrt{4 - \frac{4}{16}} < K_I < 2 - \frac{1}{16} + \sqrt{4 - \frac{4}{16}} \Longrightarrow \\ \Longrightarrow \frac{31}{16} - \sqrt{\frac{15}{4}} < K_I < \frac{31}{16} + \sqrt{\frac{15}{4}} \Longrightarrow \\ \Longrightarrow \sim 0.001008 < K_I < 3.87399$$

Along the example presented in the work, $K_I = K_P/50 = 1/800 = 0.001250$ will fall under this situation, while $K_I = K_P/100$, $K_I = K_P/200$ and below will not.

When r_1 and r_2 are complex, it can be shown that the solution can be expressed as

$$E_n = -B^{\frac{n}{2}}\left(E\cos(\theta n) + F\sin(\theta n)\right),$$

where E, F and θ are defined as

$$E = \frac{-AE_1 + E_2}{B}, \tag{A.12}$$

$$F = -i\frac{A^2E_1 - AE_2 + 2E_1B}{B\sqrt{A^2 + 4B}}, \tag{A.13}$$

$$\theta = \arccos\left(\frac{A}{2\sqrt{-B}}\right) \tag{A.14}$$

while $A = r_1 + r_2$, $B = -r_1r_2$. In other words, the error function will behave like an exponentially dampened sine wave.

The determinant factor for the response speed of the PI controller is going to be the dampening term $-B^{n/2}$ in the controller, equal to

$$\left(\frac{4+K_P^2+K_I^2-4K_P-4K_I+2K_PK_I+4K_I-K_P^2-2K_PK_I-K_I^2}{4}\right)^{\frac{n}{2}} = \\ = \left(\frac{4-4K_P}{4}\right)^{\frac{n}{2}} = (1-K_P)^{\frac{n}{2}}$$

In this situation, it can be easily seen that the error function decays slower than the P controller due to the overshoot that comes with the employment of P controller.

The case in which $K_P^2 + 2K_PK_I + K_I^2 - 4K_I > 0$ corresponds to the conditions when

$$\text{either} \quad K_I < 2 - K_P - \sqrt{4-4K_P} \qquad \text{or} \quad K_I > 2 - K_P + \sqrt{4-4K_P}$$

In this situation, r_1, r_2 are real and the C, D parameters can be obtained directly from the starting conditions.

- $E_0 = 1$ leads to: $\quad C + D = 1$
- $E_1 = 1 - K_P - K_I$ leads to:

$$1 - K_P - K_I = C\left[\frac{2-K_P-K_I+\sqrt{K_P^2+2K_PK_I+K_I^2-4K_I}}{2}\right] + \\ + D\left[\frac{2-K_P-K_I-\sqrt{K_P^2+2K_PK_I+K_I^2-4K_I}}{2}\right] \Longrightarrow$$

$$\Longrightarrow 1 - K_P - K_I = \frac{2}{2}(C+D) - (C+D)\left(\frac{K_p+K_I}{2}\right) + \\ + (C-D)\frac{\sqrt{K_P^2+2K_PK_I+K_I^2-4K_I}}{2} \Longrightarrow$$

$$\Longrightarrow 1 - K_P - K_I = 1 - \left(\frac{K_p+K_I}{2}\right) + \\ + (C-D)\frac{\sqrt{K_P^2+2K_PK_I+K_I^2-4K_I}}{2} \quad \Longrightarrow$$

$$\Longrightarrow -\left(\frac{K_p+K_I}{2}\right) = (C-D)\frac{\sqrt{K_P^2+2K_PK_I+K_I^2-4K_I}}{2} \Longrightarrow$$

$$\Longrightarrow C - D = -\frac{K_p + K_I}{\sqrt{K_P^2 + 2K_PK_I + K_I^2 - 4K_I}}$$

Now, remembering the previous step, we have $C = 1 - D$ which leads to:

$$\begin{aligned}
&\Longrightarrow 1 - D - D = -\frac{K_p + K_I}{\sqrt{K_P^2 + 2K_PK_I + K_I^2 - 4K_I}} \Longrightarrow \\
&\Longrightarrow 1 - 2D = -\frac{K_p + K_I}{\sqrt{K_P^2 + 2K_PK_I + K_I^2 - 4K_I}} \quad \Longrightarrow \\
&\Longrightarrow D = \frac{1}{2}\left(1 + \frac{K_p + K_I}{\sqrt{K_P^2 + 2K_PK_I + K_I^2 - 4K_I}}\right) \quad \text{and} \\
&\qquad\qquad C = \frac{1}{2}\left(1 - \frac{K_p + K_I}{\sqrt{K_P^2 + 2K_PK_I + K_I^2 - 4K_I}}\right)
\end{aligned}$$

As a result, the evolution of the error function is going to be:

$$\begin{aligned}
E_n = &\frac{1}{2}\left(1 + \frac{K_P + K_I}{\sqrt{K_P^2 + 2K_PK_I + K_I^2 - 4K_I}}\right) \cdot \\
&\cdot \left[\frac{2 - K_P - K_I + \sqrt{K_P^2 + 2K_PK_I + K_I^2 - 4K_I}}{2}\right]^n + \\
&+ \frac{1}{2}\left(1 - \frac{K_P + K_I}{\sqrt{K_P^2 + 2K_PK_I + K_I^2 - 4K_I}}\right) \cdot \\
&\cdot \left[\frac{2 - K_P - K_I - \sqrt{K_P^2 + 2K_PK_I + K_I^2 - 4K_I}}{2}\right]^n
\end{aligned}$$

In order for PI to reduce the error faster than P, both elements of the solution must fall faster than $(1 - K_P)$ in absolute value. Since here it is assumed that $\sqrt{K_P^2 + 2K_PK_I + K_I^2 - 4K_I} > 0$, this is equivalent to testing the condition:

$$\frac{2 - K_P - K_I + \sqrt{K_P^2 + 2K_PK_I + K_I^2 - 4K_I}}{2} < 1 - K_P$$

Which is simplified to

$$\begin{aligned} 2 - K_P - K_I + \sqrt{K_P^2 + 2K_PK_I + K_I^2 - 4K_I} < 2 - 2K_P \implies \\ \implies -K_I + \sqrt{K_P^2 + 2K_PK_I + K_I^2 - 4K_I} < -K_P \implies \\ \implies \sqrt{K_P^2 + 2K_PK_I + K_I^2 - 4K_I} < K_I - K_P \end{aligned} \tag{A.15}$$

Since the square root must be positive (because this is the non-oscillating solution), the relation above can only be verified for $K_I > K_P$, and can be compared to the initial conditions

$$K_I < 2 - K_P - \sqrt{4 - 4K_P} \qquad \text{or} \qquad K_I > 2 - K_P + \sqrt{4 - 4K_P}$$

In particular, in the case when $K_I > 2 - K_P + \sqrt{4 - 4K_P}$ it can be seen that, if $K_P < 1$, then $2 - K_P + \sqrt{4 - 4K_P} > 1$. If this is the case, then it must also be $K_I > 1$ but in this condition noise is not suppressed, so it will not be taken in consideration.

In the case when $K_I < 2 - K_P - \sqrt{4 - 4K_P}$, it can be shown that $2 - K_P + \sqrt{4 - 4K_P} < K_P$:

$$\begin{aligned} 2 - K_P - \sqrt{4 - 4K_P} < K_P \implies \\ \implies 1 - K_P < \sqrt{1 - K_P} \implies \\ \implies 1 - 2K_P + K_P^2 < 1 - K_P \implies \\ \implies K_P^2 < K_P \end{aligned}$$

which is verified, since $K_P < 1$. Since we have $K_I < 2 - K_P - \sqrt{4 - 4K_P}$ we also have that $K_I < K_P$, which contradicts the condition at (A.15).

As a conclusion, in every possible situation any PI controller will reach 95% of the step response more slowly than a P controller with the same K_P, while also having less noise suppression due to the presence of the integral component in addition with the proportional one.

Visually, the reason for this can be found in the overshoot linked with the step change: right after the sudden increase of the real value, the error of the PI controller will be positive for the first number of steps, increasing the cumulative error that is multiplied by K_I. When the PI controller output will reach the value of the increase, the error sum will still be positive, and will keep on increasing the output, creating the overshoot. It can be said that the integral component in PI and PID controllers add an inertia in the response of the controller.

Bibliography

[1] Abdurrahman, F. and G. Sugiarta, Implementation of Kalman Filter on Visual Tracking Using PID Controller, *Mechatronics and Applications: An International Journal (MECHATROJ)*, 1.1 (2017). [cit. p. 96]

[2] Agrawal, G. P., *Nonlinear Fiber Optics, 4th ed.* Academic Press, 2007. [cit. p. 9]

[3] Bao, X., J. Dhliwayo, N. Heron, D. J. Webb, and D. A. Jackson, Experimental and theoretical studies on a distributed temperature sensor based on Brillouin scattering, *J. Lit. Technol.* 13.7 (1995), pp. 1340–1348. [cit. p. 19]

[4] Bao, X., D. J. Webb, and D. A. Jackson, 32-km distributed temperature sensor based on Brillouin loss in an optical fiber, *Opt. Lett.* 18.18 (1993), pp. 1561–1563. [cit. p. 18]

[5] Bernini, R., A. Minardo, and L. Zeni, A reconstruction technique for stimulated Brillouin scattering fiber-optic sensors for simultaneous measurement of temperature and strain, *SENSORS, 2002 IEEE*, vol. 2, IEEE, 2002, pp. 1006–1011. [cit. p. 20]

[6] Bertozzi, M., A. Broggi, A. Fascioli, A. Tibaldi, R. Chapuis, and F. Chausse, Pedestrian localization and tracking system with Kalman filtering, *IEEE Intelligent Vehicles Symposium, 2004*, IEEE, 2004, pp. 584–589. [cit. p. 97]

[7] Bolognini, G., S. Faralli, A. Chiuchiarelli, F. Falconi, and F. Di Pasquale, High-power and low-RIN lasers for advanced first-and higher order Raman copumping, *IEEE Photonic Tech. L.* 18.15 (2006), pp. 1591–1593. [cit. p. 36]

[8] Boyd, R. W., *Nonlinear optics, 2nd ed.* Academic Press, 2003. [cit. p. 10, 13]

[9] Brown, A. W., J. P. Smith, X. Bao, M. D. Demerchant, and T. Bremner, Brillouin scattering based distributed sensors for structural applications, *J. Intel.Mat. Syst. Str.* 10.4 (1999), pp. 340–349. [cit. p. 24]

[10] Cardoza-Avendano, L., V. Spirin, R. López-Gutiérrez, C. López-Mercado, and C. Cruz-Hernández, Experimental characterization of DFB and FP chaotic lasers with strong incoherent optical feedback, *Opt. Laser Technol.* 43.5 (2011), pp. 949–955. [cit. p. 52]

[11] Chaudhuri, D., M. Mukherjee, M. H. Khondekar, and K. Ghosh, Simple exponential smoothing and its control parameter: A reassessment, *Recent Trends in Signal and Image Processing*, Springer, 2019, pp. 63–77. [cit. p. 88]

[12] Chiang, A. C., *Fundamental Methods of Mathematical Economics, 3rd edition*, McGraw-Hill, New York, 1984. [cit. pp. 89, 131]

[13] Chiuchiolo, A., L. Palmieri, M. Consales, M. Giordano, A. Borriello, H. Bajas, et al., Cryogenic-temperature profiling of high-power superconducting lines using local and distributed optical-fiber sensors, *Opt. Lett.* 40.19 (2015), pp. 4424–4427. [cit. p. 6]

[14] Clivati, C., G. Bolognini, D. Calonico, S. Faralli, F. Levi, A. Mura, et al., Distributed Raman optical amplification in phase coherent transfer of optical frequencies, *IEEE Photonic Tech. L.* 25.17 (2013), pp. 1711–1714. [cit. p. 37]

[15] Cola, S., L. Schenato, L. Brezzi, F. C. Tchamaleu Pangop, L. Palmieri, and A. Bisson, Composite anchors for slope stabilisation: Monitoring of their in-situ behaviour with optical fibre, *Geosciences*, 9.5 (2019), p. 240. [cit. p. 9]

[16] Costa, L., R. Magalhães, L. Palmieri, H. Martins, S. Martin-Lopez, M. R. Fernández-Ruiz, et al., Fast and direct measurement of the linear birefringence profile in standard single-mode optical fibers, *Opt. Lett.* 45.3 (2020), pp. 623–626. [cit. p. 39]

[17] Cowle, G. J. and D. Y. Stepanov, Hybrid Brillouin/erbium fiber laser, *Opt. Lett.* 21.16 (1996), pp. 1250–1252. [cit. p. 32]

[18] Culshaw, B., Fibre optic sensor technology: An engineering reality or a scientific opportunity?, *Fourth European Workshop on Optical Fibre Sensors*, vol. 7653, International Society for Optics and Photonics, 2010, p. 765304. [cit. p. 5]

[19] Darouach, M., M. Zasadzinski, A. B. Onana, and S. Nowakowski, Kalman filtering with unknown inputs via optimal state estimation of singular systems, *Int. J. Syst. Sci.* 26.10 (1995), pp. 2015–2028. [cit. p. 96]

[20] Debut, A., S. Randoux, and J. Zemmouri, Linewidth narrowing in Brillouin lasers: Theoretical analysis, *Phys. Rev. A*, 62.2 (2000), p. 023803. [cit. p. 60]

[21] Derickson, D., C. Hentschel, and J. Vobis, *Fiber optic test and measurement*, vol. 8, Prentice Hall PTR New Jersey, 1998. [cit. p. 59]

[22] Desurvire, E., *Erbium-Doped Fiber Amplifiers: Principles and Applications*, Wiley, New York, 1994. [cit. p. 32]

[23] Diaz, S., S. F. Mafang, M. Lopez-Amo, and L. Thévenaz, A high-performance optical time-domain Brillouin distributed fiber sensor, *IEEE Sens. J.* 8.7 (2008), pp. 1268–1272. [cit. p. 17]

[24] Dong, Y., L. Chen, and X. Bao, System optimization of a long-range Brillouin-loss-based distributed fiber sensor, *Appl. Optics*, 49.27 (2010), pp. 5020–5025. [cit. pp. 18]

[25] Dong, Y., L. Chen, and X. Bao, Time-division multiplexing-based BOTDA over 100km sensing length, *Opt. Lett.* 36.2 (2011), pp. 277–279. [cit. p. 33]

[26] Fabelinskii, I. L., *Molecular scattering of light*, Springer, 1968. [cit. p. 12]

[27] Fan, C., H. Ju, and B. Wang, A Kalman filter based pid controller for stochastic systems, *2006 International Conference on Communications, Circuits and Systems*, vol. 3, IEEE, 2006, pp. 2055–2057. [cit. p. 80]

[28] Fang, J., P. Xu, Y. Dong, and W. Shieh, Single-shot distributed Brillouin optical time domain analyzer, *Opt. Express*, 25.13 (2017), pp. 15188–15198. [cit. p. 68]

[29] Faralli, S. and F. Di Pasquale, Impact of double Rayleigh scattering noise in distributed higher order Raman pumping schemes, *IEEE Photonic Tech. L.* 15.6 (2003), pp. 804–806. [cit. p. 36]

[30] Faralli, S., G. Bolognini, G. Sacchi, S. Sugliani, and F. Di Pasquale, Bidirectional higher order cascaded Raman amplification benefits for 10-Gb/s WDM unrepeated transmission systems, *J. Lit. Technol.* 23.8 (2005), pp. 2427–2433. [cit. p. 37]

[31] Fayçal, B. H., K. Karim, R. José, G. Moncef, et al., Unbiased Minimum-Variance Filter for State and Fault Estimation of Linear Time-Varying Systems with Unknown Disturbances, *Math. Probl. Eng.* 2010 (). [cit. p. 96]

[32] Galtarossa, A., L. Palmieri, M. Santagiustina, L. Schenato, and L. Ursini, Polarized Brillouin amplification in randomly birefringent and unidirectionally spun fibers, *IEEE Photonic. Tech. L.* 20.16 (2008), pp. 1420–1422. [cit. p. 38]

[33] Galtarossa, A., L. Palmieri, M. Schiano, and T. Tambosso, Statistical characterization of fiber random birefringence, *Opt. Lett.* 25.18 (2000), pp. 1322–1324. [cit. p. 39]

[34] Galtarossa, A., L. Palmieri, M. Schiano, and T. Tambosso, Measurement of birefringence correlation length in long, single-mode fibers, *Opt. Lett.* 26.13 (2001), pp. 962–964. [cit. p. 34]

[35] Gautam, D. and C. Ha, Control of a quadrotor using a smart self-tuning fuzzy PID controller, *Int. J. Adv. Robot Syst.* 10.11 (2013), p. 380. [cit. p. 80]

[36] Geng, J. and S. Jiang, Pump-to-Stokes transfer of relative intensity noise in Brillouin fiber ring lasers, *Opt. Lett.* 32.1 (2007), pp. 11–13. [cit. pp. 36–37]

[37] Geng, J., S. Staines, Z. Wang, J. Zong, M. Blake, and S. Jiang, Actively stabilized Brillouin fiber laser with high output power and low noise, *2006 Optical Fiber Communication Conference and the National Fiber Optic Engineers Conference*, IEEE, 2006, 3–pp. [cit. p. 64]

[38] Grattan, K. and T. Sun, Fiber optic sensor technology: an overview, *Sensor Actuat. A-Phys.* 82.1-3 (2000), pp. 40–61. [cit. pp. 5, 7]

[39] Horiguchi, T., T. Kurashima, and M. Tateda, Tensile strain dependence of Brillouin frequency shift in silica optical fibers, *IEEE Photonic Tech. L.* 1.5 (1989), pp. 107–108. [cit. p. 16]

[40] Horiguchi, T., K. Shimizu, T. Kurashima, M. Tateda, and Y. Koyamada, Development of a distributed sensing technique using Brillouin scattering, *J. Lit. Technol.* 13.7 (1995), pp. 1296–1302. [cit. pp. 16, 64]

[41] Horiguchi, T. and M. Tateda, BOTDA-nondestructive measurement of single-mode optical fiber attenuation characteristics using Brillouin interaction: theory, *J. Lit. Technol.* 7.8 (1989), pp. 1170–1176. [cit. p. 16]

[42] Huang, S., L. Thévenaz, K. Toyama, B. Y. Kim, and H. Shaw, Optical Kerr-effect in fiber-optic Brillouin ring laser gyroscopes, *IEEE Photonic Tech. L.* 5.3 (1993), pp. 365–367. [cit. p. 54]

[43] Iribas Pardo, H., J. Urricelqui Polvorinos, J. Mariñelarena Ollacarizqueta, M. Sagüés García, and A. Loayssa Lara, Cost-effective Brillouin optical time-domain analysis sensor using a single optical source and passive optical filtering, *J. Sens.* (2016). [cit. p. 27]

[44] Julier, S. J. and J. K. Uhlmann, New extension of the Kalman filter to nonlinear systems, *Signal processing, sensor fusion, and target recognition VI*, vol. 3068, International Society for Optics and Photonics, 1997, pp. 182–193. [cit. p. 97]

[45] Kang, S.-W., J.-S. Kim, and G.-W. Kim, Road roughness estimation based on discrete Kalman filter with unknown input, *Vehicle System Dynamics*, 57.10 (2019), pp. 1530–1544. [cit. p. 96]

[46] Keller, J.-Y., M. Darouach, and L. Caramelle, Kalman filter with unknown inputs and robust two-stage filter, *Int. J. Syst. Sci.* 29.1 (1998), pp. 41–47. [cit. p. 97]

[47] Kersey, A. D., A review of recent developments in fiber optic sensor technology, *Opt. Fiber. Techynol.* 2.3 (1996), pp. 291–317. [cit. pp. 5–7]

[48] Kim, Y.-J., B. Chun, Y. Kim, S. Hyun, and S.-W. Kim, Generation of optical frequencies out of the frequency comb of a femtosecond laser for DWDM telecommunication, *Laser Phys. Lett.* 7.7 (2010), pp. 522–527. [cit. p. 51]

[49] Lanticq, V., F. Taillade, R. Gabet, and S. Delepine-Lesoille, *Distributed optical fibre sensors for Structural Health Monitoring: Upcoming challenges, Optical Fibre, New Developments*, INTECH Open Access Publisher, 2009. [cit. p. 7]

[50] Li, X., X. Liu, Y. Gong, H. Sun, L. Wang, and K. Lu, A novel erbium/ytterbium co-doped distributed feedback fiber laser with single-polarization and unidirectional output, *Laser Phys. Lett.* 7.1 (2010), pp. 55–59. [cit. p. 51]

[51] López-Mercado, C. A., V. V. Spirin, S. I. Kablukov, E. A. Zlobina, I. O. Zolotovskiy, P. Mégret, et al., Accuracy of single-cut adjustment technique for double resonant Brillouin fiber lasers, *Opt. Fiber Technol.* 20.3 (2014), pp. 194–198. [cit. p. 49–50]

[52] Ma, X., S. M. Djouadi, T. P. Kuruganti, J. J. Nutaro, and H. Li, Optimal estimation over unreliable communication links with application to cognitive radio, *Proceedings of the 48h IEEE Conference on Decision and Control (CDC) held jointly with 2009 28th Chinese Control Conference*, IEEE, 2009, pp. 4062–4067. [cit. p. 96]

[53] Marini, D., M. Iuliano, F. Bastianini, and G. Bolognini, BOTDA sensing employing a modified Brillouin fiber laser probe source, *J. Lit. Technol.* 36.4 (2018), pp. 1131–1137. [cit. p. 35, 48]

[54] Marini, D., L. Rossi, F. Bastianini, and G. Bolognini, Enhanced-performance fibre Brillouin ring laser for Brillouin sensing applications, *Optical Fiber Sensors*, Optical Society of America, 2018, ThE71. [cit. p. 36]

[55] Marini, D., L. Rossi, F. Bastianini, and G. Bolognini, Study of enhanced performance fiber Brillouin ring laser with wavelength-locking for sensing applications, *20th Italian National Conference on Photonic Technologies (Fotonica 2018)*, IET, 2018, pp. 1–4. [cit. p. 36]

[56] Marini, D., L. Rossi, F. Bastianini, and G. Bolognini, Tunable lower-RIN Brillouin fiber ring laser for BOTDA sensing, *CLEO: QELS _Fundamental Science*, Optical Society of America, 2018, JW2A–166. [cit. p. 36]

[57] Marini, D., L. Rossi, F. Bastianini, and G. Bolognini, Actively stabilized low-noise Brillouin fiber ring laser for Brillouin sensing, *Fiber Lasers*

XVI: Technology and Systems, vol. 10897, International Society for Optics and Photonics, 2019, 108971U. [cit. p. 61]

[58] Marini, D., L. Rossi, F. Bastianini, and G. Bolognini, Enhanced performance low-noise Brillouin ring laser for Brillouin sensing, *Seventh European Workshop on Optical Fibre Sensors*, vol. 11199, International Society for Optics and Photonics, 2019, p. 111993I. [cit. p. 61]

[59] Marini, D., L. Rossi, F. Bastianini, and G. Bolognini, Low-noise wavelength-locked Brillouin ring laser for Brillouin sensing, *Seventh European Workshop on Optical Fibre Sensors*, vol. 11199, International Society for Optics and Photonics, 2019, p. 1119924. [cit. p. 49]

[60] Marini, D., L. Rossi, F. Bastianini, and G. Bolognini, Narrow Linewidth Fiber Brillouin Ring Laser for Sensing Applications, *2019 PhotonIcs & Electromagnetics Research Symposium-Spring (PIERS-Spring)*, IEEE, 2019, pp. 2964–2969. [cit. p. 57]

[61] Marini, D., L. Rossi, F. Bastianini, and G. Bolognini, Wavelength-locked low-noise Brillouin ring laser for Brillouin sensing, *2019 International Workshop on Fiber Optics in Access Networks (FOAN)*, IEEE, 2019, pp. 16–19. [cit. pp. 47, 57]

[62] Minardo, A., R. Bernini, and L. Zeni, Analysis of SNR penalty in Brillouin optical time-domain analysis sensors induced by laser source phase noise, *J. Opt.* 18.2 (2015), p. 025601. [cit. p. 34]

[63] Minardo, A., R. Bernini, and L. Zeni, Accurate distributed temperature measurements by Brillouin Scattering fiber-optic sensor, *SENSORS, 2003 IEEE*, vol. 1, IEEE, 2003, pp. 348–352. [cit. p. 20]

[64] Minardo, A., R. Bernini, and L. Zeni, A simple technique for reducing pump depletion in long-range distributed Brillouin fiber sensors, *IEEE Sens. J.* 9.6 (2009), pp. 633–634. [cit. p. 38]

[65] Minardo, A., R. Bernini, L. Zeni, L. Thevenaz, and F. Briffod, A reconstruction technique for long-range stimulated Brillouin scattering distributed fibre-optic sensors: experimental results, *Meas. Sci. Technol.* 16.4 (2005), pp. 900–908. [cit. pp. 19, 21]

[66] Moradi, H. and G. Vossoughi, Robust control of the variable speed wind turbines in the presence of uncertainties: A comparison between H8 and PID controllers, *Energy*, 90 (2015), pp. 1508–1521. [cit. p. 80]

[67] Mussi, G., N. Gisin, R. Passy, and J. Von der Weid, -152.5 dB sensitivity high dynamic-range optical frequency-domain reflectometry, *Electron. Lett.* 32.10 (1996), pp. 926–927. [cit. p. 9]

[68] Nicati, P.-A., K. Toyama, S. Huang, and H. Shaw, Frequency pulling in a Brillouin fiber ring laser, *IEEE Photonic. Tech. L.* 6.7 (1994), pp. 801–803. [cit. p. 54]

[69] Nicati, P.-A., K. Toyama, and H. J. Shaw, Frequency stability of a Brillouin fiber ring laser, *J. Lit. Technol.* 13.7 (1995), pp. 1445–1451. [cit. pp. 46, 54]

[70] Nikles, M., L. Thevenaz, and P. A. Robert, Brillouin gain spectrum characterization in single-mode optical fibers, *J. Lit. Technol.* 15.10 (1997), pp. 1842–1851. [cit. pp. 16, 56]

[71] Nikles, M., L. Thévenaz, and P. A. Robert, Simple distributed fiber sensor based on Brillouin gain spectrum analysis, *Opt. Lett.* 21.10 (1996), pp. 758–760. [cit. pp. 9, 24, 26]

[72] Ohtsubo, J., *Semiconductor lasers: stability, instability and chaos*, vol. 111, Springer, 2012. [cit. p. 51]

[73] Palmieri, L. and A. Galtarossa, Distributed fiber optic sensor for mapping of intense magnetic fields based on polarization sensitive reflectometry, *Third Asia Pacific Optical Sensors Conference*, vol. 8351, International Society for Optics and Photonics, 2012, p. 835131. [cit. p. 7]

[74] Palmieri, L. and L. Schenato, Distributed optical fiber sensing based on Rayleigh scattering, *Open Optic. J.* 7.1 (2013). [cit. p. 9]

[75] Pan, S., P. Du, Y. Li, Z. Chen, and H. Wang, The study on an general Kalman filter with unknown inputs, *Proceeding of the 11th World Congress on Intelligent Control and Automation*, IEEE, 2014, pp. 3562–3567. [cit. p. 96]

[76] Parker, T., M. Farhadiroushan, R. Feced, V. Handerek, and A. Rogers, Simultaneous distributed measurement of strain and temperature from noise-initiated Brillouin scattering in optical fibers, *IEEE J. Quantum Elect.* 34.4 (1998), pp. 645–659. [cit. p. 16]

[77] Parker, T., M. Farhadiroushan, V. Handerek, and A. Roger, A fully distributed simultaneous strain and temperature sensor using spontaneous Brillouin backscatter, *IEEE Photonic Tech. L.* 9.7 (1997), pp. 979–981. [cit. p. 16]

[78] Peled, Y., A. Motil, and M. Tur, Fast Brillouin optical time domain analysis for dynamic sensing, *Opt. Express*, 20.8 (2012), pp. 8584–8591. [cit. p. 67]

[79] Rogers, A., Distributed optical-fibre sensing, *Meas. Sci. Technol.* 10.8 (1999), R75. [cit. p. 8]

[80] Rohmanuddin, M. and A. Widyotriatmo, A novel method of self-tuning PID control system based on time-averaged Kalman filter gain, *2013 3rd International Conference on Instrumentation Control and Automation (ICA)*, IEEE, 2013, pp. 25–30. [cit. p. 80]

[81] Rossi, L., D. Marini, F. Bastianini, and G. Bolognini, Study of Brillouin optical time domain analysis fiber sensing with stabilized low-RIN pump-probe laser scheme, *20th Italian National Conference on Photonic Technologies (Fotonica 2018)*, IET, 2018, pp. 1–4. [cit. p. 47]

[82] Rossi, L., D. Marini, F. Bastianini, and G. Bolognini, Brillouin Optical Time Domain Analysis with Wavelength-locked Low-noise Pump-probe Laser Scheme, *2019 PhotonIcs & Electromagnetics Research Symposium-Spring (PIERS-Spring)*, IEEE, 2019, pp. 2958–2963. [cit. p. 55, 57–58, 60]

[83] Rossi, L., D. Marini, F. Bastianini, and G. Bolognini, Analysis of enhanced-performance fibre Brillouin ring laser for Brillouin sensing applications, *Opt. Express*, 27.20 (2019), pp. 29448–29459. [cit. p. 62–63]

[84] Rossi, L., D. Marini, F. Bastianini, and G. Bolognini, Wavelength-locked doubly-resonant cavity fibre Brillouin ring laser for BOTDA sensing, *Optical Fiber Communication Conference*, Optical Society of America, 2019, W2A–16. [cit. pp. 46–47]

[85] Rossi, L., D. Marini, F. Bastianini, and G. Bolognini, Tunable and stabilized short cavity Brillouin fiber ring laser for BOTDA sensing, *CLEO: QELS_Fundamental Science*, Optical Society of America, 2020, JTu2G–11. [cit. p. 49]

[86] Schenato, L., L. Palmieri, M. Camporese, S. Bersan, S. Cola, A. Pasuto, et al., Distributed optical fibre sensing for early detection of shallow landslides triggering, *Sci. Rep.* 7.1 (2017), pp. 1–7. [cit. p. 9]

[87] Schenato, L., A. Pasuto, A. Galtarossa, and L. Palmieri, An optical fibre cable for distributed pressure sensing: a proof of concept, *Seventh European Workshop on Optical Fibre Sensors*, vol. 11199, International Society for Optics and Photonics, 2019, 111991Y. [cit. p. 9]

[88] Schenato, L., A. Pasuto, A. Galtarossa, and L. Palmieri, An Optical fiber distributed pressure sensing cable with Pa-sensitivity and enhanced spatial resolution, *IEEE Sens. J.* 20.11 (2020), pp. 5900–5908. [cit. p. 9]

[89] Shin, S., U. Sharma, H. Tu, W. Jung, and S. A. Boppart, Characterization and analysis of relative intensity noise in broadband optical sources for optical coherence tomography, *IEEE Photonic. Tech. L.* 22.14 (2010), pp. 1057–1059. [cit. p. 37]

[90] Simha, A., M. Tallam, H. Shankar, R. Muralishankar, and H. Simha, Adaptive attitude control of the spherical drone on SO (3), *2016 IEEE Distributed Computing, VLSI, Electrical Circuits and Robotics (DISCOVER)*, IEEE, 2016, pp. 90–94. [cit. p. 96]

[91] Smith, S., *The Scientist and Engineer's Guide to Digital Signal Processing*, California Technical Pub., 1997. [cit. pp. 82–83, 85–87]

[92] Song, K. Y. and S. Yang, Simplified Brillouin optical time-domain sensor based on direct modulation of a laser diode, *Opt. Express*, 18.23 (2010), pp. 24012–24018. [cit. p. 28]

[93] Soto, M. A. and L. Thévenaz, Modeling and evaluating the performance of Brillouin distributed optical fiber sensors, *Opt. Express*, 21.25 (2013), pp. 31347–31366. [cit. p. 70]

[94] Soto, M. A. and L. Thévenaz, Towards 1'000'000 resolved points in a distributed optical fibre sensor, *23rd International Conference on Optical Fibre Sensors*, vol. 9157, International Society for Optics and Photonics, 2014, p. 9157C3. [cit. p. 63]

[95] Spirin, V. V., C. A. López-Mercado, S. I. Kablukov, E. A. Zlobina, I. O. Zolotovskiy, P. Mégret, et al., Single cut technique for adjustment

of doubly resonant Brillouin laser cavities, *Opt. Lett.* 38.14 (2013), pp. 2528–2530. [cit. p. 49]

[96] Spirin, V., C. López-Mercado, D. Kinet, P. Mégret, I. Zolotovskiy, and A. Fotiadi, A single-longitudinal-mode Brillouin fiber laser passively stabilized at the pump resonance frequency with a dynamic population inversion grating, *Laser Phys. Lett.* 10.1 (2012), p. 015102. [cit. pp. 51–53]

[97] Spirin, V., C. López-Mercado, P. Mégret, and A. Fotiadi, Single-mode Brillouin fiber laser passively stabilized at resonance frequency with self-injection locked pump laser, *Laser Phys. Lett.* 9.5 (2012), p. 377. [cit. p. 47]

[98] Stokes, L., M. Chodorow, and H. Shaw, All-fiber stimulated Brillouin ring laser with submilliwatt pump threshold, *Opt. Lett.* 7.10 (1982), pp. 509–511. [cit. pp. 28–30]

[99] Sugimoto Dimitrova, R., M. Gehrig, D. Brescianini, and D. Scaramuzza, Towards Low-Latency High-Bandwidth Control of Quadrotors using Event Cameras, *arXiv*, (2019), arXiv–1911. [cit. p. 80]

[100] Tang, K.-S., K. F. Man, G. Chen, and S. Kwong, An optimal fuzzy PID controller, *IEEE T. Ind. Electron.* 48.4 (2001), pp. 757–765. [cit. pp. 80]

[101] Thévenaz, L., *Inelastic scatterings and applications to distributed sensing*, tech. rep., EPFL Press, distributed by CRC Press, 2011. [cit. p. 68]

[102] Voskoboinik, A., O. F. Yilmaz, A. W. Willner, and M. Tur, Sweep-free distributed Brillouin time-domain analyzer (SF-BOTDA), *Opt. Express*, 19.26 (2011), B842–B847. [cit. p. 67]

[103] Wakitani, S., H. Nakanishi, Y. Ashida, and T. Yamamoto, Study on a Kalman Filter based PID Controller, *IFAC-PapersOnLine*, 51.4 (2018), pp. 422–425. [cit. p. 96]

[104] Wan, E. A. and R. Van Der Merwe, The unscented Kalman filter for nonlinear estimation, *Proceedings of the IEEE 2000 Adaptive Systems for Signal Processing, Communications, and Control Symposium (Cat. No. 00EX373)*, IEEE, 2000, pp. 153–158. [cit. p. 97]

[105] Welch, G. and G. Bishop, An introduction to the Kalman filter, *UNC-Chapel Hill*, TR95-041 (2000). [cit. p. 96]

[106] Yang, G., X. Fan, and Z. He, Strain Dynamic Range Enlargement of Slope-Assisted BOTDA by Using Brillouin Phase-Gain Ratio, *J. Lit. Technol.* 35.20 (2017), pp. 4451–4458. [cit. pp. 79, 82]

[107] Yang, J., S. Pan, and H. Huang, An adaptive extended Kalman filter for structural damage identifications II: unknown inputs, *Struct. Control Hlth.* 14.3 (2007), pp. 497–521. [cit. p. 96]

[108] Yang, Z., M. A. Soto, D. M. Chow, P. Ray, and L. Thévenaz, Brillouin distributed optical fiber sensor based on a closed-loop configuration, *J. Lit. Technol.* 36.5 (2018), pp. 1239–1248. [cit. pp. 71–74, 76–79, 81, 88, 91, 103, 113, 116–117, 121–122, 126, 133]

[109] Yu, F. and S. Yin, *Fiber Optic Sensors*, Marcel Dekker Inc., New York, 2002. [cit. pp. 5]

[110] Zhao, C., M. Tang, L. Wang, H. Wu, Z. Zhao, Y. Dang, et al., BOTDA using channel estimation with direct-detection optical OFDM technique, *Opt. Express*, 25.11 (2017), pp. 12698–12709. [cit. p. 68]

Acknowledgements

This work would not have been possible without the guidance and assistance of many people. In particular, I'd like to express my most heartfelt thanks to the following.

Professor Gabriele Bolognini, who offered me extremely precious guidance in the field of distributed optical fiber sensing for the entire PhD period. In particular, I am grateful for the innumerable opportunities he provided me for expanding my knowledge, my skills and my experience in all aspects of research.

Doctor Diego Marini from CNR, that assisted me in these three years with every small problem I could have had with both experiments and bureaucracy.

Doctor Filippo Bastianini from Sestosensor s.r.l, who provided invaluable support in terms of both equipment and advice, and whose inventive solutions to every problem were downright inspiring.

Professor Luc Thévenaz from the Group for Fiber Optics (GFO) at the École polytechnique fédérale de Lausanne (EPFL), who offered me the chance to be a part of the exceptional group he directs for nine months, and allowed me the opportunity of exploring new and exiting avenues for distributed optical fiber sensing. I would also like to thank him dearly for all the support he always shown to everyone during the most difficult and hectic moments of this year. Doctor Zhisheng Yang, also from GFO, who patiently followed me during my work and was always available to discuss all my ideas and doubts, despite his numerous and demanding duties.

All the other researchers and PhD students at GFO, Fan, Li, Malak Simon and Suneetha, that during the months I worked there helped and supported me in innumerable ways, big and small.

I would also like to thank Svetlana Mashkina, the administrative assistant for GFO, that was able to help me with incredible efficiency for all the issue I could have had in Switzerland.

Finally, I want to thank my co-Supervisor, professor Beatrice Fraboni from the University of Bologna, who offered invaluable advice and support for

my entire University experience, acting as a tutor for my career at Collegio Superiore, and guided me through the thesis works for my Bachelor, Master and now PhD.